

CHARLES UNIVERSITY IN PRAGUE
FACULTY OF MATHEMATICS AND PHYSICS
INSTITUTE OF PHYSICS OF CHARLES UNIVERSITY



Doctoral Thesis

**Optical interactions in thin films
of selected magnetic oxides**

Martin Veis

Praha 2009

Supervisor: Prof. Ing. Štefan Višňovský, DrSc.

Advisor: Dr. Jan Mistrík

Study Program: Physics

Study Branch: F6 - Quantum optics and optoelectronics

I declare that my PhD Thesis has been elaborated personally and that I have used only the literature listed. I agree with loaning out my work.

Praha, 13 March 2009

To Eva, Libor and my parents

First of all, I would like to express my gratitude to Prof. Ing. Štefan Višňovský, DrSc., who was leading me during my diploma and doctoral studies, since 2004 (the year of assigning my Master Diploma Thesis) up to now, and whose guidance and great deal of support contributed to my acquired experience in both experimental and theoretical magneto-optics, as well as in various pieces of knowledge in related physical disciplines. I also thank him for introducing me into the international scientific community and for the experience that he shared with me.

I would also like to express my thanks to my advisor Dr. Jan Mistrík who gave me the background of experimental ellipsometry. I am also grateful to him for numerous discussions of special problems of optical and magneto-optical properties of $\text{La}_{2/3}\text{Sr}_{1/3}\text{MnO}_3$ and CuFe_2O_4 thin films.

I am thankful to RNDr. R. Antoš, PhD, my long-time friend since the Master Course studies in Charles University, for numerous discussions about the basic physical topics as well as for his careful reading of the manuscript of this thesis.

I would like to thank to Prof. T. Yamaguchi for the opportunity of ellipsometric measurements in his laboratory in Research Institute of Electronics of Shizuoka University in Japan.

My great thanks belong to Prof. P. Beauvillain, Prof. P. Lecoeur and Prof. B. Mercey for collaboration in research of the $\text{La}_{2/3}\text{Sr}_{1/3}\text{MnO}_3$ thin films. I am also grateful to Prof. P. Lecoeur for a very friendly atmosphere of scientific cooperation during my short stay in Orsay.

Similarly, I am very thankful to Prof. S. Prasad and Prof. R. Krishnan for grateful cooperation on the research of CuFe_2O_4 and Bi:YIG thin films which resulted in papers at international journals and at the conferences oriented to magnetism. I also thank to Prof. S. Prasad for preparation of the samples which were the subjects of this thesis.

I am also thankful to Prof. A. Ishida for the opportunity to stay in his laboratory during my study stay at Shizuoka University in Japan as well as for his huge support and discussions about the basic physical phenomena in the field of solid state physics .

Next, my special thanks belong to my other colleagues and good friends, namely Eva Lišková, Vratislav Kolinský, Jiří Franta, Miroslav Nývlt, Kamil Postava and Radek Lopušník.

I would also like to thank to my parents and my brother for a huge support during my whole life.

Finally, I am thankful to my girlfriend Eva, who was always with me.

Contents

1	Introduction	1
1.1	General introduction	1
1.2	Aim of this thesis	3
1.3	Collaborations	3
1.4	Thesis outline	4
2	Polarization states of light	6
2.1	Polarization ellipse	6
2.2	Jones formalism	8
2.3	Complex plane representation	11
2.4	Propagation of polarized light through polarizing optical elements	12
2.5	Ellipsometric and magneto-optical angles	14
3	Material properties described by permittivity tensor	18
3.1	Macroscopical description	18
3.1.1	Symmetry arguments	19
3.2	Microscopic theory of material tensors	21
3.2.1	Lorentz model	22
3.2.2	Semiclassical theory of material tensors	23
3.2.3	Diamagnetic and paramagnetic transitions	25
4	Optics of magnetic materials	28
4.1	Wave equation in anisotropic medium	28
4.2	Propagation parallel to the magnetization vector	30
4.3	Polar Kerr effect at normal light incidence	31
4.4	Anisotropic multilayers	33
4.4.1	Matrix representation of multilayered structure	35
4.4.2	Eigenmodes in isotropic regions	38

4.4.3	Reflection and transmission coefficients	40
5	Experimental techniques	43
5.1	Spectroscopic ellipsometry	43
5.1.1	Basic experimental setup	44
5.1.2	Experimental data processing	46
5.2	Magneto-optical spectroscopy	47
5.2.1	DC measurement techniques	47
5.2.2	Modulation techniques	49
5.2.3	Magneto-optical spectrometer based on the azimuth modulation technique	50
5.2.4	Calibration procedure and experimental data processing	55
6	Experimental results on $\text{La}_{2/3}\text{Sr}_{1/3}\text{MnO}_3$ thin films	57
6.1	Material Introduction	57
6.2	Sample deposition	59
6.3	Spectroscopic Ellipsometry	65
6.4	Magneto-optical spectroscopy	67
6.5	Conclusions	82
7	Experimental results on CuFe_2O_4 thin films	84
7.1	Material introduction	84
7.2	Sample deposition	86
7.3	Spectroscopic ellipsometry	87
7.4	Magneto-optical spectroscopy	90
7.4.1	Polar geometry	90
7.4.2	Longitudinal geometry	98
7.5	Conclusion	100
8	Experimental results on Bi:YIG thin films	102
8.1	Material introduction	102
8.2	Sample deposition	103
8.3	Magneto-optical spectroscopy	104
8.3.1	Polar geometry	104
8.3.2	Longitudinal geometry	109
8.4	Conclusion	112
9	Summary	114

1 Introduction

1.1 General introduction

Magneto-optical (MO) effects play an important role in various experimental techniques. Historically, the first manifestation of magneto-optical effect was demonstrated by Michael Faraday in 1846. He found an interesting azimuth rotation of linearly polarized light after its passage through a glass rod inserted into magnetic field. The azimuth of the rotation was proportional to the applied magnetic field and to the length of the glass rod. This phenomenon got the name after its discoverer and is called Faraday rotation. Several years later in 1876, Reverend John Kerr announced azimuth rotations, however much weaker, after the reflection of polarized light on a magnetized metallic iron mirror. He found that this magneto-optical effect in reflection was proportional to the sample magnetization. The effect was later labeled the magneto-optical Kerr effect.

In the case of the magneto-optical Kerr effect, we can distinguish between three special configurations of magnetization vector with respect to the sample surface and the plane of incident light. In polar geometry (the first demonstration done by J. Kerr), the magnetization vector is perpendicular to the sample surface. In longitudinal geometry (discovered in 1878), the magnetization vector is parallel to both, the sample surface and the plane of incident light. Finally the transverse effect, predicted by C. H. Wind in 1897 and demonstrated for the first time by P. Zeeman in 1898, occurs when the magnetization lies in the plane of the sample and simultaneously is perpendicular to the plane of incident light. Schematically are these geometries shown in Fig. 1.1.

Owing to the nature of the magneto-optical Kerr effect, the experimental techniques based on it are widely used as a tool to investigate magnetism inside thin films. They combine several advantages with respect to other techniques, which is high sensitivity (comparable with superconducting quantum interference device (SQUID) magnetometry), possibility of time resolved measurements [1], in a special setup also rather good lateral resolution down to $0.2 \mu\text{m}$ [2], and depth sensitive measurements. In this thesis magneto-optical spectroscopy is combined with spectroscopic ellipsometry to provide the full information about the permittivity tensor of investigated material.

1.1. GENERAL INTRODUCTION

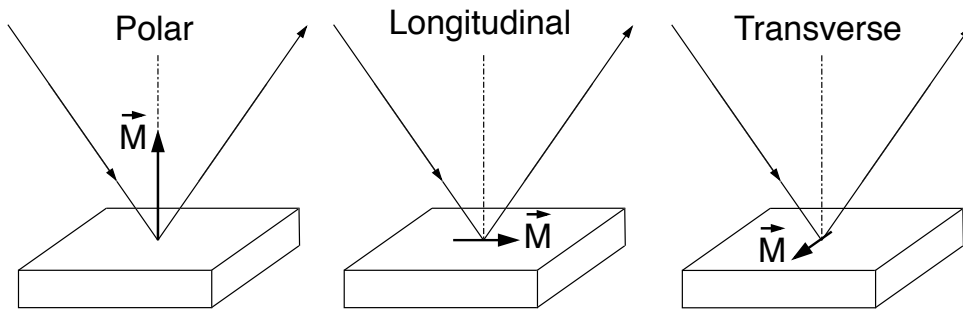


Figure 1.1: Three main geometries of the magneto-optical Kerr effect.

Magnetic oxides have been intensively studied for decades. From the magneto-optical point of view, one of the first attentions was dedicated to ferrimagnetic oxides with garnet structure [3, 4, 5, 6]. 1970's and 1980's were driven by extensive research on magnetic garnet thin films prepared by liquid phase epitaxy (LPE) onto gallium gadolinium garnet (GGG) substrates. The research was motivated by magnetic bubble domain memory, a concept using non-mechanical access to the stored information. Such films are optically transparent for visible light and exhibit large Faraday rotation. Thanks to this property, theoretically predicted domain structures could be verified by using MO microscopy. This enabled progress in the research of static and dynamic properties of magnetic domains. Since the first magneto-optical investigations, rapid development in the field of deposition techniques passed, and today most of the magnetic oxides are usually prepared by pulsed laser deposition (PLD). This technique enables to prepare high quality films with thicknesses below 50 nm.

The discovery of high-temperature superconductivity in cuprates [7] and discovery of the colossal magnetoresistance (CMR) effect [8, 9, 10] renewed the interest in magnetic oxides in 1990's. New low-dimensional oxides such as CuGe_3 [11] or CaV_4O_9 [12] have been studied. However, a large part of the recent interest has been devoted to the mixed-valence manganese oxides, exhibiting a metal-insulator transition accompanied by CMR, motivated by the application in sensors and spintronic devices. For purposes of the device applications, the growth of thin layers of magnetic oxides with well defined structural, magnetic and optical properties is necessary. This is the main technological challenge of these days. Moreover, it is necessary to characterize physical properties of such thin layers reliably. Since these properties are usually bound together, the combination of magneto-optical spectroscopy and spectroscopic ellipsometry appears to be a good probe technique to get information about complex structural, magnetic and optical properties of various magnetic oxides.

Since this thesis presents results for three groups of magnetic oxides, a detailed introduction

to each material with the motivation of the work is included in each experimental chapter. This will make this thesis easy readable.

1.2 Aim of this thesis

This thesis is dedicated to improve our understanding of optical and magnetic properties of selected magnetic oxides thin films. As experimental tools, spectroscopic ellipsometry and magneto-optical spectroscopy are employed. With regard to a small thickness of investigated materials, their properties may differ from those of bulk materials and are dependent on interfaces. Therefore a qualitative comparison of the obtained results with those presented in literature is another goal of this thesis.

1.3 Collaborations

This thesis is based on the optical and magneto-optical investigations of thin films of magnetic oxides which were prepared in collaborating laboratories. Moreover, the experiment of spectroscopic ellipsometry has been performed in co-operation with other laboratory. Therefore we list here all co-operating laboratories, which contributed to the results presented in this thesis.

- *Research Institute of Electronics, Shizuoka University, Hamamatsu, Japan* - Spectroscopic ellipsometry measurements - laboratory of Prof. T. Yamaguchi.
- *Institut d'Electronique Fondamentale, Université Paris Sud, Orsay, France* - Deposition of $\text{La}_{2/3}\text{Sr}_{1/3}\text{MnO}_3$ thin films using PLD technique and their structural characterization - laboratory of Prof. P. Beauvillain and Prof. P. Lecoeur
- *Laboratoire de Cristallographie et Sciences des Matériaux, CNRS, Caen, France* - Deposition of $\text{La}_{2/3}\text{Sr}_{1/3}\text{MnO}_3$ thin films using PLD technique and their structural characterization - laboratory of Prof. B. Mercey and Prof. W. Prellier
- *Indian Institute of Technology, Bombay, India* - Deposition of Bi substituted yttrium iron garnet thin films as well as CuFe_2O_4 thin films and their structural characterization - laboratory of Prof. S. Prasad
- *Laboratoire de Magnetisme et d'Optique, CNRS, Versailles, France* - Bi substituted yttrium iron garnet thin films and CuFe_2O_4 thin films - Prof. R. Krishnan

1.4 Thesis outline

The present work consists of:

- **Chapter 1:** The current introduction.
- **Chapter 2:** Brief introduction into the light polarization phenomenon and its description by the Jones formalism. This chapter define the optical and magneto-optical quantities measured in experiments.
- **Chapter 3:** Here, the basic of the theory of permittivity tensor is given. Two, macroscopic and microscopic, approaches are described, which connects the experimental quantities with microscopical processes inside the matter. The microscopical semiclassical theory is later used for the assignment of observed spectral dependencies to electronic transitions inside investigated material.
- **Chapter 4:** Generalized Yeh's 4x4 matrix formalism is introduced. This framework was applied to derive the elements of the permittivity tensor from experimental data as well as to calculate model polar and longitudinal Kerr spectra.
- **Chapter 5:** Basic description and characteristics of experimental techniques used for spectroscopic ellipsometry and magneto-optical spectroscopy measurements.
- **Chapter 6:** Experimental chapter. In this chapter, original results on $\text{La}_{2/3}\text{Sr}_{1/3}\text{MnO}_3$ thin films deposited on two types of substrates are presented. Besides an experimental data presented in this chapter, a comparison with literature is made resulting in the description of electronic transitions observed in this material. Moreover, comparison of optical and magneto-optical properties of samples deposited on different types of substrates is given.
- **Chapter 7:** Experimental chapter. Seventh chapter describes original results obtained on CuFe_2O_4 thin films. Applying the same procedure as in the previous chapter, the combination of spectroscopic ellipsometry with magneto-optical spectroscopy provided complete information about optically active electron transitions inside this material.
- **Chapter 8:** Experimental chapter. In this chapter, original magneto-optical results obtained on Bi substituted yttrium iron garnet thin films are presented. Utilizing strong interference in the infrared region of the spectra, the thicknesses of investigated films were calculated. Moreover, the experimental spectra were compared with theoretical calculation, showing a good agreement.

- **Chapter 9:** Here the summary of the obtained original results and conclusions are given.

2 Polarization states of light

Since the magneto-optical spectroscopy as well as the spectroscopic ellipsometry are experimental techniques based on the detection of the change of light polarization, it is favourable to make a short introduction to the description of this physical phenomenon. Although there are several approaches for description of polarized light well described in the literature [13, 14], we will focus mainly on the Jones formalism as a powerful tool to easily describe the polarized light and its transformation by polarization optical elements. We will consider the light as a monochromatic electromagnetic wave. Polarization is the general property of all vector waves.

2.1 Polarization ellipse

Without loss of generality, we choose the electric-field vector \mathbf{E} to define the state of polarization of light wave, since the electric field component is dominating in the interaction of light with matter. Once the polarization of \mathbf{E} is determined, the polarization of three remaining field vectors \mathbf{D} , \mathbf{H} and \mathbf{B} can be found using Maxwell equations. For a monochromatic wave the time variation of the electric field vector \mathbf{E} is exactly sinusoidal. In the case of the light wave propagating inside isotropic medium in the \hat{z} direction, the vibration of \mathbf{E} can be resolved into two orthogonal directions along \hat{x} and \hat{y} Cartesian coordinate axes as follows

$$\mathbf{E} = E_x \hat{x} + E_y \hat{y}, \quad (2.1)$$

where

$$E_i(z, t) = E_{0i} \cos(\omega t - \gamma_z z + \delta_i), \quad i = x, y. \quad (2.2)$$

By elimination of the term $(\omega t - \gamma_z z)$ from Eqs.(2.2) and application of simple summation rules, we find the equation

$$\left(\frac{E_x}{E_{0x}}\right)^2 - 2\frac{E_x E_y}{E_{0x} E_{0y}} \cos \delta + \left(\frac{E_y}{E_{0y}}\right)^2 = \sin^2 \delta, \quad (2.3)$$

where $\delta = (\delta_x - \delta_y)$ is the phase difference between the vibrations along the \hat{x} and \hat{y} directions. Equation (2.3) describes the ellipse, which indicates that the electric field vector traces an ellipse in the plane perpendicular to the wavevector at a fixed point in space. In other words, the polarization of the monochromatic light wave is generally elliptical.

2.2. JONES FORMALISM

- *absolute phase* δ ($-\pi \leq \delta \leq \pi$) corresponds to the angle between the major axis of the ellipse and the position of the electric field vector \mathbf{E} in the initial time $t = 0$ according to Fig. 2.1.

To describe the polarization state itself the knowledge of azimuth and ellipticity is sufficient.

2.2 Jones formalism

Polarization state of light is, in general, modified when the light is passing through optical elements. Therefore it is convenient to describe the polarization states in the framework, in which their transformation by optical elements can be easily described. There are several formalisms employed for a description of polarized light and its transformation by polarizing optical elements. However, to phenomenologically explain magneto-optical effects, Jones vectors and the complex plane representation are very appropriate. Hence, in this work we will focus on these two formalisms.

As we already mentioned, in the case of a monochromatic light wave, each Cartesian component of the electric field vector varies sinusoidally with time at all points in space. Under this condition, variation of \mathbf{E} in both x and y directions is described by only two parameters: amplitude E_{0i} and absolute phase δ_i , $i = x, y$ (see Eqs. (2.2)), because the time dependence is given. The use of the complex representation of the electric field is therefore plain enough. In this representation, both E_{0i} and δ_i , are expressed by only one complex variable E'_{0i} as

$$E'_{0i} = E_{0i}e^{j\delta_i}, \quad i = x, y. \quad (2.4)$$

Thus the spatial and time dependence of Cartesian component of the electric field vector takes the form

$$E_i(z, t) = \Re [E'_{0i}e^{j(\omega t - \gamma_z z)}], \quad (2.5)$$

which is equivalent to Eqs. (2.2). In the Eq. (2.5), \Re denotes the real part of the following expression of the electric field in the complex representation. In the real world, the electric field is never complex. Note that we have chosen the $\exp(j\omega t)$ time dependence. This is the convention widely used in the field of spectroscopical ellipsometry [13]

To describe the light polarization and its transformation by an optical device, we do not need the complete description of the wave given by Eq. (2.5). More concise mathematical description for the light wave can be found.

Monochromatic light wave is a vector wave, and we can rewrite Eqs. (2.5) in the vector form

$$\mathbf{E}(z, t) = \Re [\mathbf{E}(z)e^{j\omega t}], \quad (2.6)$$

where

$$\mathbf{E}(z) = e^{-j\gamma z} \begin{bmatrix} E_{0x} e^{j\delta_x} \\ E_{0y} e^{j\delta_y} \end{bmatrix}. \quad (2.7)$$

If we drop the spatial information about the wave by considering the field over one fixed plane, the previous equation takes the form

$$\mathbf{E}(0) = \mathbf{J} = \begin{bmatrix} E_{0x} e^{j\delta_x} \\ E_{0y} e^{j\delta_y} \end{bmatrix} = \begin{bmatrix} J_1 \\ J_2 \end{bmatrix}. \quad (2.8)$$

This vector, called Jones vector of the monochromatic, uniform and transverse electric wave, contains the complete information about amplitudes and phases of the field components. Therefore it carries the information about the polarization of the wave.

The intensity of light wave can be written with the aid of Jones vectors as¹

$$I = \mathbf{J}^\dagger \mathbf{J} = |E_{0x}|^2 + |E_{0y}|^2, \quad (2.9)$$

where \dagger denotes Hermitian adjoint. Any general polarization expressed by Jones vector \mathbf{J} can be expanded in to a linear combination of two orthogonal polarizations \mathbf{J}_1 and \mathbf{J}_2 by expression

$$\mathbf{J}_{12} = a_1 \mathbf{J}_1 + a_2 \mathbf{J}_2, \quad (2.10)$$

where a_1 and a_2 are coefficients of the expansion. The orthogonality condition for two different polarizations can be mathematically expressed as

$$\mathbf{J}_1^\dagger \mathbf{J}_2 = \mathbf{J}_2^\dagger \mathbf{J}_1 = 0. \quad (2.11)$$

Generally, one can express a polarization state by Jones vector with respect to some basis (pair of two orthogonal polarizations). There are two bases mainly used for the description of polarized light. The first, *Cartesian basis*, consist of two linear polarizations along the x and y directions

$$E_X = \begin{bmatrix} 1 \\ 0 \end{bmatrix}, \quad E_Y = \begin{bmatrix} 0 \\ 1 \end{bmatrix}, \quad (2.12)$$

while the second, *Circular basis* is using a set of right and left handed circular polarizations

$$E_R = \frac{1}{\sqrt{2}} \begin{bmatrix} 1 \\ j \end{bmatrix}, \quad E_L = \frac{1}{\sqrt{2}} \begin{bmatrix} 1 \\ -j \end{bmatrix}. \quad (2.13)$$

Both polarization bases are schematically shown in Fig. 2.2.

The Cartesian basis is widely used owing to its intuitive and clear geometric interpretation of polarization states, while the circular basis is useful for the case of the normal incidence in

¹Because, we are not usually interested in the absolute intensity, a constant multiplicative factor was omitted.

2.2. JONES FORMALISM

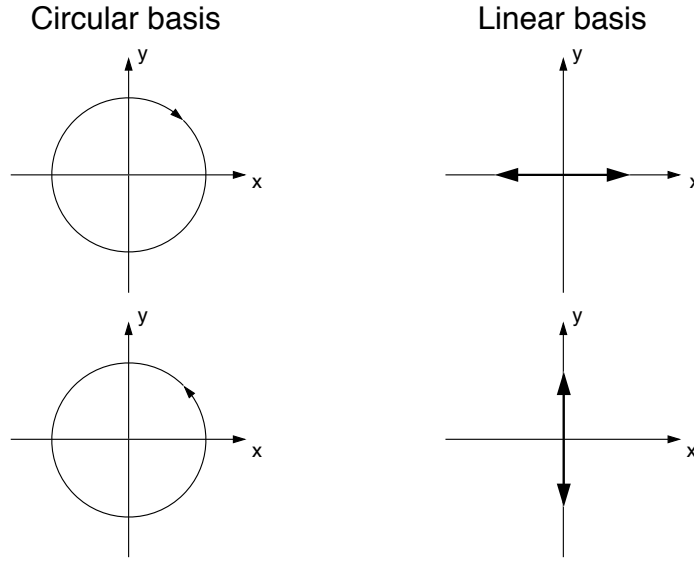


Figure 2.2: Two main bases used for the description of polarized light. Basis of circular polarizations (a) and basis of linear polarizations (b).

polar magneto-optical geometry, where the left and right handed circular polarizations are the eigenmodes propagating in the magneto-optical medium parallel to the magnetization vector. Sometimes, it is convenient to change the basis from Cartesian to circular and conversely. This change is done by a linear transformation, which can be expressed by the matrix equation

$$\mathbf{J}_{LR} = \mathbf{F}_{LR-XY} \mathbf{J}_{XY}, \quad (2.14)$$

where

$$\mathbf{F}_{LR-XY} = \frac{1}{\sqrt{2}} \begin{bmatrix} 1 & j \\ 1 & -j \end{bmatrix} \quad (2.15)$$

is called the transformation matrix from circular LR to Cartesian XY basis. The opposite transformation from Cartesian XY to circular LR basis can be easily written as

$$\mathbf{J}_{XY} = \mathbf{F}_{XY-LR} \mathbf{J}_{LR}, \quad (2.16)$$

where

$$\mathbf{F}_{XY-LR} = \mathbf{F}_{LR-XY}^{-1} = \frac{1}{\sqrt{2}} \begin{bmatrix} 1 & 1 \\ -j & j \end{bmatrix}. \quad (2.17)$$

Generally, any basic change of polarization can be expressed as a transformation of a given Jones vector. Jones vectors of principal polarization states are summarized in Table 2.1.

Polarization	Cartesian basis XY $\mathbf{J}_{XY} = \begin{bmatrix} J_X \\ J_Y \end{bmatrix}$	Circular basis LR $\mathbf{J}_{LR} = \begin{bmatrix} J_L \\ J_R \end{bmatrix}$
Linear along x direction	$\begin{bmatrix} 1 \\ 0 \end{bmatrix}$	$\frac{1}{\sqrt{2}} \begin{bmatrix} 1 \\ 1 \end{bmatrix}$
Linear along y direction	$\begin{bmatrix} 0 \\ 1 \end{bmatrix}$	$\frac{1}{\sqrt{2}} \begin{bmatrix} 1 \\ -1 \end{bmatrix}$
Linear with azimuth θ	$\begin{bmatrix} \cos \theta \\ \sin \theta \end{bmatrix}$	$\frac{1}{\sqrt{2}} \begin{bmatrix} \cos \theta + j \sin \theta \\ \cos \theta - j \sin \theta \end{bmatrix}$
Circular right handed	$\frac{1}{\sqrt{2}} \begin{bmatrix} 1 \\ j \end{bmatrix}$	$\begin{bmatrix} 0 \\ 1 \end{bmatrix}$
Circular left handed	$\frac{1}{\sqrt{2}} \begin{bmatrix} 1 \\ -j \end{bmatrix}$	$\begin{bmatrix} 1 \\ 0 \end{bmatrix}$
Elliptical with $\theta = 0$	$\begin{bmatrix} \cos \epsilon \\ j \sin \epsilon \end{bmatrix}$	$\frac{1}{\sqrt{2}} \begin{bmatrix} \cos \epsilon - j \sin \epsilon \\ \cos \epsilon + j \sin \epsilon \end{bmatrix}$
Elliptical with θ and ϵ	$\begin{bmatrix} \cos \theta \cos \epsilon - j \sin \theta \sin \epsilon \\ \sin \theta \cos \epsilon + j \cos \theta \sin \epsilon \end{bmatrix}$	$\frac{1}{\sqrt{2}} \begin{bmatrix} (\cos \epsilon - \sin \epsilon)e^{i\theta} \\ (\cos \epsilon + \sin \epsilon)e^{-i\theta} \end{bmatrix}$

Table 2.1: Jones vectors of various principal polarizations expressed in both, Cartesian and circular bases.

2.3 Complex plane representation

The Jones vector formalism, discussed in the previous section, is an effective method to describe polarization state of light. It carries the information about the amplitude A , absolute phase δ , azimuth θ and ellipticity angle ϵ of the elliptic vibration of the electric field vector \mathbf{E} . However, as we mentioned above, to describe the polarization ellipse, only two parameters θ and e or ϵ are necessary. Therefore, in cases when the amplitude and absolute phase of the electric vector vibration are of secondary interest, we can describe the polarization state by simpler expression as a ratio of the elements of Cartesian Jones vector

$$\chi = \frac{J_Y}{J_X} = \frac{E_{0y}}{E_{0x}} e^{j(\delta_y - \delta_x)}. \quad (2.18)$$

The absolute value and the argument are

$$|\chi| = \frac{E_{0y}}{E_{0x}}, \quad (2.19)$$

$$\arg(\chi) = \delta_y - \delta_x = \delta. \quad (2.20)$$

2.4. PROPAGATION OF POLARIZED LIGHT THROUGH POLARIZING OPTICAL ELEMENTS

For general elliptical polarization, χ_{XY} can be obtained easily by combination of the Eq. (2.18) and the Jones vector shown in the last line in Tab. 2.1, resulting in

$$\chi = \frac{\sin \theta \cos \epsilon + j \cos \theta \sin \epsilon}{\cos \theta \cos \epsilon - j \sin \theta \sin \epsilon} = \frac{\tan \theta + j \tan \epsilon}{1 - j \tan \theta \tan \epsilon}. \quad (2.21)$$

Eq. (2.21) shows explicitly how each polarization state of elliptically polarized light with azimuth θ and ellipticity angle ϵ can be associated with a single complex number χ . Each complex number χ represents a single point in the complex plane. This representation is called Cartesian complex-plane representation owing to the Cartesian Jones vector elements in the definition of χ .

In the case of very small azimuth and ellipticity angles ($\theta, \epsilon \ll 1$), when usage of the Taylor series is appropriate, Eq. (2.21) is simplified to the form²

$$\chi = \frac{J_Y}{J_X} \approx \theta + j\epsilon. \quad (2.22)$$

Similarly to the case of the Cartesian complex number, we can obtain the complex number χ_{LR} for the circular representation

$$\chi_{LR} = \frac{J_R}{J_L} = \frac{1 + \tan \epsilon}{1 - \tan \epsilon} e^{-2j\theta} = \tan \left(\frac{\pi}{4} + \epsilon \right) e^{-2j\theta}. \quad (2.23)$$

The inverse relations to Eq. (2.22) are

$$\tan \epsilon = \frac{|\chi_{LR}| - 1}{|\chi_{LR}| + 1}, \quad \theta = -\frac{1}{2} \arg(\chi_{LR}). \quad (2.24)$$

The assignment of the polarization states to different points in the complex plane for the Cartesian and circular representation is shown in Fig. 2.3.

2.4 Propagation of polarized light through polarizing optical elements

As we mentioned in the previous sections, the change of the polarization state of light can be expressed, using the Jones formalism, as a linear transformation represented by unitary transformation matrix. Certain class of optical elements (we call them polarizing optical elements) can produce a specific change of the polarization state of light. These special optical elements can be described, within the Jones formalism, by so called Jones matrices. If we define two right handed coordinate systems $[x_I, y_I, z_I]$ and $[x_O, y_O, z_O]$ for incoming and outgoing light

²The quantity χ is often used in magneto-optics as the complex magneto-optical angle ϕ , so the magneto-optical rotation θ and ellipticity ϵ are the real and imaginary parts of the Cartesian complex number.

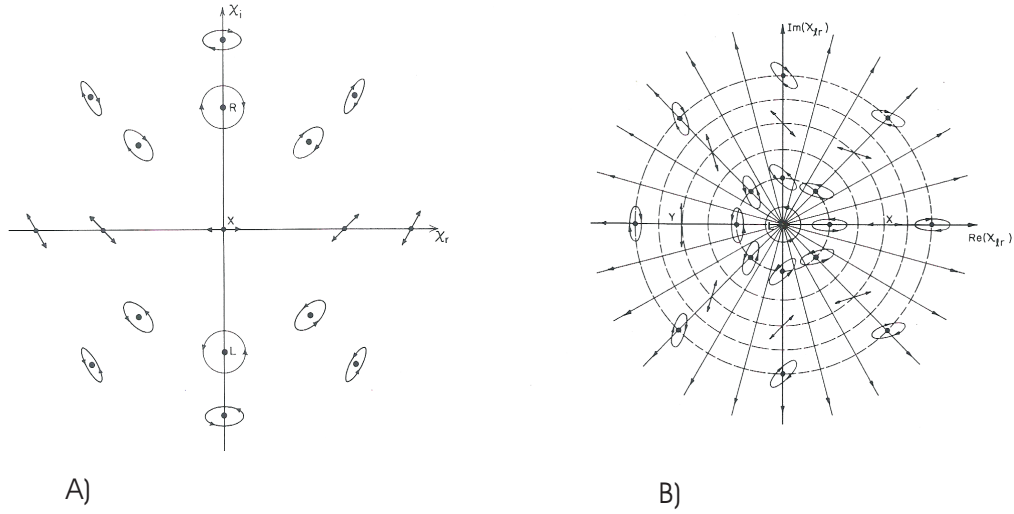


Figure 2.3: Representations of the polarization states in Cartesian (a) and circular (b) bases.

(Fig. 2.4) and describe the polarization states in these coordinate systems by Jones vectors \mathbf{J}_I and \mathbf{J}_O , we can express the polarization change by optical element as

$$\begin{bmatrix} J_{Ox} \\ J_{Oy} \end{bmatrix} = \begin{bmatrix} T_{11} & T_{12} \\ T_{21} & T_{22} \end{bmatrix} \begin{bmatrix} J_{Ix} \\ J_{Iy} \end{bmatrix}, \quad \text{or} \quad \mathbf{J}_O = \mathbf{T} \mathbf{J}_I, \quad (2.25)$$

where the 2×2 matrix \mathbf{T} is the Jones matrix of the optical polarizing element. We already showed that the Jones vector can be written with respect to some basis. Until now, we described the Jones matrix of optical element in the Cartesian basis representation. However, in some cases the use of circular basis representation is more advantageous. The transformation of the Jones matrix form one basis to another is given by simple formula

$$\mathbf{T}_{LR} = \mathbf{F}^{-1} \mathbf{T}_{XY} \mathbf{F}. \quad (2.26)$$

The survey of the Cartesian and circular Jones matrices of the basic optical polarizing elements is listed in Tab. 2.2.

In the real measuring equipment light is not going through only one optical element, but usually through a cascade of optical elements. Therefore we have to introduce, in general, a set of coordinate systems, two for each element. However, the situation become more simple, because the output coordinate system of the i -th element is identical with the input system of the $(i + 1)$ -th element. Therefore, for n optical polarizing elements in the system is valid the equation

$$\mathbf{J}_{n,O} = \mathbf{T}_n \mathbf{J}_{n,I} = \mathbf{T}_n \mathbf{J}_{n-1,O} = \mathbf{T}_n \mathbf{T}_{n-1} \mathbf{J}_{n-2,I} = \mathbf{T}_n \cdots \mathbf{T}_2 \mathbf{T}_1 = \mathbf{T} \mathbf{J}_{1,I}. \quad (2.27)$$

2.5. ELLIPSOMETRIC AND MAGNETO-OPTICAL ANGLES

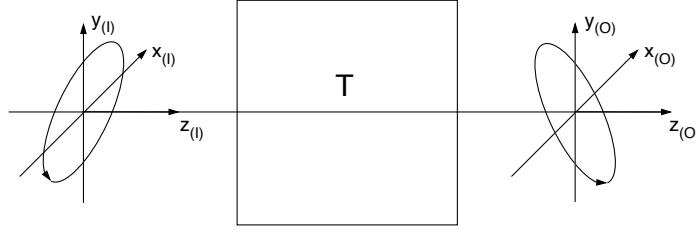


Figure 2.4: Transformation of the polarization state of light due to its passage through an optical element.

It is also possible to describe the polarizing optical element in the complex plane representation. For this purpose, we define a polarization transfer function, which is determined by the elements of the Jones matrix T , using the definition of the complex polarization parameter χ

$$\chi_O = \frac{T_{22}\chi_I + T_{21}}{T_{12}\chi_I + T_{11}}. \quad (2.28)$$

2.5 Ellipsometric and magneto-optical angles

The purpose of the magneto-optical methods is to describe the influence of the magnetized sample on the polarization state of light after its reflection or transmission. In both cases, the optical behavior of the sample can be macroscopically described within the Jones formalism using the Cartesian representation. Owing to the Cartesian representation, we introduce two special polarizations: s - polarization (linear polarization perpendicular to the plane of incidence) and p -polarization (linear polarization parallel to the plane of incidence). We describe Jones matrices of the sample in the basis of s and p polarizations (Fig. 2.5). The response of the sample to the light wave is then expressed for reflected and transmitted light by

$$\mathbf{J}_R = \begin{bmatrix} r_{ss} & r_{ps} \\ r_{sp} & r_{pp} \end{bmatrix} \mathbf{J}_I = \mathbf{R}_{SP} \mathbf{J}_I, \quad (2.29)$$

$$\mathbf{J}_T = \begin{bmatrix} t_{ss} & t_{ps} \\ t_{sp} & t_{pp} \end{bmatrix} \mathbf{J}_I = \mathbf{T}_{SP} \mathbf{J}_I. \quad (2.30)$$

Jones matrices \mathbf{R}_{SP} and \mathbf{T}_{SP} carry the full information about the magneto-optical properties of the sample and their elements are amplitude reflection and transmission coefficients for the s and p waves.

Cartesian basis XY	Circular basis LR
Linear polarizer rotated by angle α with respect to x axis	
$\begin{bmatrix} \cos^2 \alpha & \sin \alpha \cos \alpha \\ \sin \alpha \cos \alpha & \sin^2 \alpha \end{bmatrix}$	$\frac{1}{2} \begin{bmatrix} 1 & e^{2j\alpha} \\ e^{-2j\alpha} & 1 \end{bmatrix}$
Phase plate - linear retarder δ	
$\begin{bmatrix} e^{j\frac{\delta}{2}} & 0 \\ 0 & e^{-j\frac{\delta}{2}} \end{bmatrix}$	$\begin{bmatrix} \cos \frac{\delta}{2} & j \sin \frac{\delta}{2} \\ j \sin \frac{\delta}{2} & \cos \frac{\delta}{2} \end{bmatrix}$
Rotator by angle ξ	
$\begin{bmatrix} \cos \xi & -\sin \xi \\ \sin \xi & \cos \xi \end{bmatrix}$	$\frac{1}{2} \begin{bmatrix} e^{j\xi} & 0 \\ 0 & e^{-j\xi} \end{bmatrix}$

Table 2.2: Jones matrices of basic optical polarizing elements expressed in both, Cartesian and circular bases.

When the material of the sample is isotropic, \mathbf{R}_{SP} and \mathbf{T}_{SP} are diagonal and there is no interaction between the s and p waves. The diagonal elements are related to the material structure and its optical properties. Thus we define the ellipsometric angles Ψ and Δ by following equation

$$\rho = \frac{r_p}{r_s} = \tan \Psi e^{j\Delta}. \quad (2.31)$$

To derive Ψ and Δ angles is the field of the optical ellipsometry. The situation changes when the magnetic field is applied to the sample. The off-diagonal elements become, generally, non zero, which indicates the conversion between s incident and p reflected (r_{ps}) as well as p incident and s reflected (r_{sp}) waves. Although the Jones matrices of reflection and transmission have generally four elements, in the case of three main geometries of magneto-optical setup one can consider the symmetry of the problem to simplify the form of these matrices [15]. The reflection matrices for three main magneto-optical geometries at oblique incidence are given in Tab. 2.3. Moreover, for polar and longitudinal geometries, one can write the relations between the direction of the magnetization vector and the elements of the Jones reflection matrix as

$$r_{ss}(-\mathbf{M}) = r_{ss}(\mathbf{M}), \quad (2.32)$$

$$r_{pp}(-\mathbf{M}) = r_{pp}(\mathbf{M}), \quad (2.33)$$

$$r_{ps}(-\mathbf{M}) = -r_{ps}(\mathbf{M}), \quad (2.34)$$

$$r_{sp}(-\mathbf{M}) = -r_{sp}(\mathbf{M}). \quad (2.35)$$

On the other hand, in the case of the transverse geometry, the wavevector of the incident light beam is perpendicular to \mathbf{M} vector, which yields $r_{sp} = r_{ps} = 0$.

2.5. ELLIPSOMETRIC AND MAGNETO-OPTICAL ANGLES

Polar geometry	$R_{SP} = \begin{bmatrix} r_{ss} & r_{ps} \\ -r_{sp} & r_{pp} \end{bmatrix}$
Longitudinal geometry	$R_{SP} = \begin{bmatrix} r_{ss} & r_{sp} \\ r_{sp} & r_{pp} \end{bmatrix}$
Transverse geometry	$R_{SP} = \begin{bmatrix} r_{ss} & 0 \\ 0 & r_{pp} \end{bmatrix}$

Table 2.3: Jones reflection matrices for three main magneto-optical geometries.

To find the relations between the complex reflection coefficients (elements of the Jones reflection matrix) and the quantities describing the magneto-optical effects (azimuth and ellipticity of the reflected wave), we have to distinguish between two principal incident polarizations commonly used to probe the magneto-optical media. Considering now the s incident polarization, the reflected light is described by the Jones vector

$$\begin{bmatrix} r_{ss} & r_{ps} \\ r_{sp} & r_{pp} \end{bmatrix} \begin{bmatrix} 1 \\ 0 \end{bmatrix} = \begin{bmatrix} r_{ss} \\ r_{sp} \end{bmatrix} = r_{ss} \begin{bmatrix} 1 \\ \frac{r_{sp}}{r_{ss}} \end{bmatrix} = r_{ss} \begin{bmatrix} 1 \\ \chi \end{bmatrix}. \quad (2.36)$$

The reflected light, which is elliptically polarized, is described by the complex number χ . Practically, in the real measurement, the magneto-optical effect can be considered as a very small perturbation ($\chi \ll 1$). Taking into account the Eq. (2.21), one can derive the expression

$$\chi \approx \phi_{Ks} = \theta_{Ks} + j\epsilon_{Ks} = \frac{r_{sp}}{r_{ss}}, \quad (2.37)$$

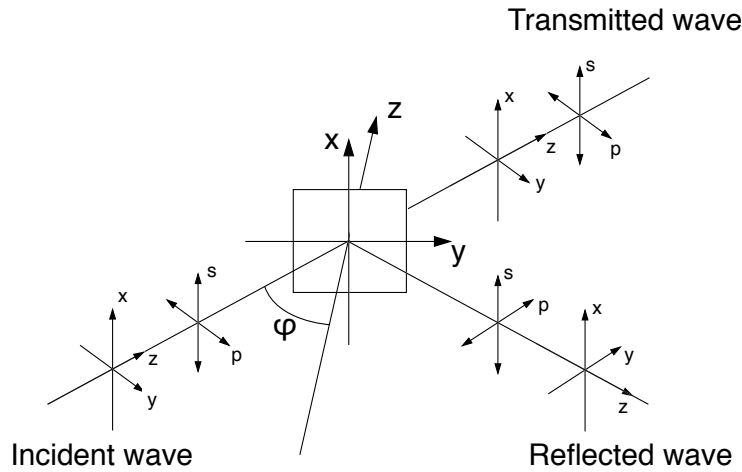


Figure 2.5: Definition of the coordinate system for the description of polarization of incident, reflected and transmitted light.

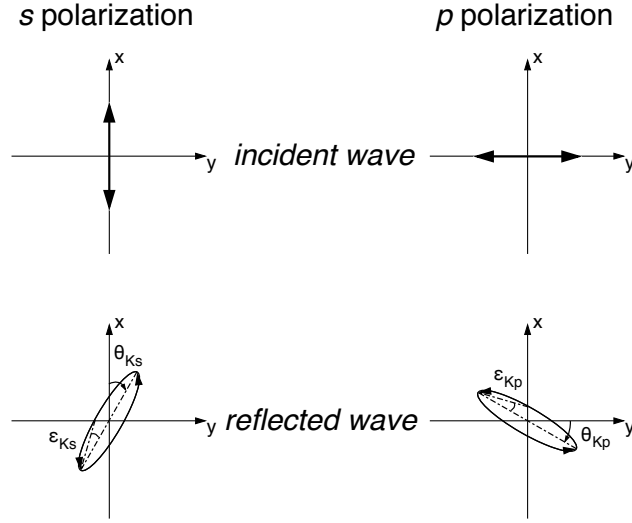


Figure 2.6: Geometrical meaning of magneto-optical variables.

where ϕ_{Ks} , θ_{Ks} and ϵ_{Ks} are the complex magneto-optical angle, Kerr rotation and Kerr ellipticity, respectively (see Fig. 2.6). Similarly, we can derive the relations for p incident wave. The Jones vector of the reflected light is

$$\begin{bmatrix} r_{ss} & r_{ps} \\ r_{sp} & r_{pp} \end{bmatrix} \begin{bmatrix} 0 \\ 1 \end{bmatrix} = \begin{bmatrix} r_{ps} \\ r_{pp} \end{bmatrix} = r_{pp} \begin{bmatrix} \frac{r_{ps}}{r_{pp}} \\ 1 \end{bmatrix} = r_{pp} \begin{bmatrix} \chi^{-1} \\ 1 \end{bmatrix}, \quad (2.38)$$

which leads to the relation

$$\chi^{-1} = \frac{J_X}{J_Y} = -\frac{\tan \theta_{Kp} + j \tan \epsilon_{Kp}}{1 - j \tan \theta_{Kp} \tan \epsilon_{Kp}} \approx -(\theta_{Kp} + j \epsilon_{Kp}). \quad (2.39)$$

Therefore

$$\phi_{Kp} = \theta_{Kp} + j \epsilon_{Kp} = -\frac{r_{ps}}{r_{pp}}. \quad (2.40)$$

The sign of θ_{Kp} is clear from Fig. 2.6.

Equations (2.37) and (2.40) relate the magneto-optical quantities θ and ϵ , measurable by magneto-optical spectroscopy, with complex reflection coefficients (which carry the information about the internal electronic structure of the matter). Thus getting the partial information about the electronic structure of investigated samples by magneto-optical spectroscopy is possible.

The relations for the Faraday magneto-optical angles in transmission can be obtained in a similar way.

3 Material properties described by permittivity tensor

In the previous chapter, we introduced the magneto-optical Kerr effect as a change of the light wave polarization state due to its reflection on magnetized sample. For phenomenological interpretation of measured Kerr effect spectral dependencies, it is not necessary to go into the details of microscopic models describing the interaction between the electromagnetic wave and electronic structure inside the matter. Nowadays, usual models which deal with the calculation of the magneto-optical effects are macroscopic, based on the electromagnetic theory. In such models, properties of the material are described in terms of its permittivity (or dielectric) tensor. With the knowledge of experimental data, it is possible to derive the elements of this tensor to get the information about the properties of investigated material. Thus, the permittivity tensor is the mathematical concept by which microscopic theory and laboratory experiment are related. Therefore it is useful to introduce some of its basic properties and show how this tensor is related to the microscopical transitions induced by incident light wave. This is the aim of this section. The basic properties will be shown within the macroscopic theory utilizing the simple symmetry arguments, while the relation to electron transitions inside the material will be shown with the help of basic microscopic models.

3.1 Macroscopical description

In this work, we deal with the interaction of the light wave with material. Owing to the frequencies of order 10^{15} Hz, the interaction between the electromagnetic wave and electron spins can be neglected [16]. Therefore we can consider only the interaction of the electromagnetic wave with the orbital motion. In the description of common materials, only the interaction of the electric field of the wave with matter can be considered. This leads to the fact that optical properties of matter are usually described in terms of the complex permittivity. Generally this

permittivity can be a second rank tensor expressed as

$$\boldsymbol{\epsilon} = \begin{bmatrix} \epsilon_{xx} & \epsilon_{xy} & \epsilon_{xz} \\ \epsilon_{yx} & \epsilon_{yy} & \epsilon_{yz} \\ \epsilon_{zx} & \epsilon_{zy} & \epsilon_{zz} \end{bmatrix}. \quad (3.1)$$

In various fields of solid state physics, material properties need not to be described only by the permittivity tensor. Therefore it is useful to mention here two other material tensors of optical conductivity and susceptibility.

The relation between the complex permittivity and optical conductivity tensors can be derived from the wave equation

$$\Delta \mathbf{E} - \mu_0 \boldsymbol{\epsilon}' \frac{\partial^2 \mathbf{E}}{\partial t^2} = \mu_0 \boldsymbol{\sigma}' \frac{\partial \mathbf{E}}{\partial t}. \quad (3.2)$$

Here the dielectric properties of matter are described by the real permittivity tensor $\boldsymbol{\epsilon}'$, while the losses are expressed by the real conductivity $\boldsymbol{\sigma}'$. If we will consider the time dependence of \mathbf{E} as $e^{j\omega t}$, we can add the conductivity into the complex permittivity and form the expression

$$\boldsymbol{\epsilon} = \mathbf{1} + \frac{j}{\epsilon_0 \omega} \boldsymbol{\sigma}. \quad (3.3)$$

The relation between optical susceptibility and permittivity can be expressed as [15]

$$\boldsymbol{\epsilon} = \mathbf{1} + \boldsymbol{\chi}. \quad (3.4)$$

3.1.1 Symmetry arguments

The general form of the permittivity tensor can be derived without necessity of microscopic models, utilizing only the symmetry arguments. Let's consider an isotropic medium in the magnetic field. This field induces a magnetic ordering which acts as a small perturbation of the system. If we limit ourselves to the case of collinear magnetic order, we can expand the complex permittivity tensor into the McLaurin power series of the macroscopic magnetization. In the Cartesian coordinating system, we can write [6, 17]

$$\begin{aligned} \epsilon_{ij} &= \epsilon_{ij}^{(0)} + \left(\frac{\partial \epsilon_{ij}}{\partial M_k} \right)_{M=0} M_k + \frac{1}{2} \left(\frac{\partial^2 \epsilon_{ij}}{\partial M_k \partial M_l} \right)_{M=0} M_k M_l + \dots \\ &= \epsilon_{ij}^{(0)} + K_{ijk} M_k + G_{ijkl} M_k M_l. \end{aligned} \quad (3.5)$$

Here $\epsilon_{ij}^{(0)}$ denotes the components of the permittivity tensor without the magnetic field, M_k are components of the magnetization vector. The third-rank axial tensor with components K_{ijk} relates the permittivity to static magnetization. The tensor \mathbf{K} is called the linear magneto-optical tensor. Owing to the properties of this tensor, linear magneto-optical effects are allowed

3.1. MACROSCOPICAL DESCRIPTION

in the crystal point groups that include the spatial inversion operation. This is contrary to the linear electro-optical effects [18].

The components G_{ijkl} belongs to the quadratic magneto-optical polar tensor which relates permittivity (polar tensor) to the product $M_k M_l$ (which form another polar tensor). Indices i, j, k, l denote here the Cartesian x, y, z axes. The Onsager principle of reciprocity [6, 19, 20, 21], which requires the simultaneous reversal of time and magnetic field, can be written as

$$\varepsilon_{ij}(\mathbf{M}) = \varepsilon_{ji}(-\mathbf{M}). \quad (3.6)$$

From this relation follows that the symmetric part of the permittivity tensor is even function of \mathbf{M} . Contrary the antisymmetric part is odd function of \mathbf{M} .

Let's now show how the symmetry of the problem can simplify the general permittivity tensor (3.1). We consider an originally isotropic material inserted into a magnetic field with the magnetization vector oriented along the principal axis parallel to the Cartesian z axis. Its symmetry point group contains all rotations about the principal axis and products of rotations and reflections in the plane normal to the principal axis. In Schönflies notation, it is denoted as $C_{\infty h}$ [22]. Therefore the permittivity tensor has to be invariant under the operations of the group represented by matrix transformation

$$\varepsilon(\mathbf{M}) = \begin{bmatrix} \cos \varphi & \sin \varphi & 0 \\ -\sin \varphi & \cos \varphi & 0 \\ 0 & 0 & \pm 1 \end{bmatrix} \begin{bmatrix} \varepsilon_{xx} & \varepsilon_{xy} & \varepsilon_{xz} \\ \varepsilon_{yx} & \varepsilon_{yy} & \varepsilon_{yz} \\ \varepsilon_{zx} & \varepsilon_{zy} & \varepsilon_{zz} \end{bmatrix} \begin{bmatrix} \cos \varphi & -\sin \varphi & 0 \\ \sin \varphi & \cos \varphi & 0 \\ 0 & 0 & \pm 1 \end{bmatrix}, \quad (3.7)$$

where φ is the angle of the rotation about the z axis and the \pm signs indicates the proper (+) and improper (-) rotations, respectively. The general form of the permittivity tensor resulting from the latter equation is

$$\varepsilon = \begin{bmatrix} \varepsilon_{xx} & \varepsilon_{xy} & 0 \\ -\varepsilon_{xy} & \varepsilon_{xx} & 0 \\ 0 & 0 & \varepsilon_{zz} \end{bmatrix}. \quad (3.8)$$

The aim of this work is to investigate the material properties using magneto-optical Kerr spectroscopy. Because the Kerr effect is linear in magnetization, we can restrict our work only to linear magneto-optical effects, which implies $\varepsilon_{zz} = \varepsilon_{xx}$. Thus we can rewrite the permittivity tensor in the special form

$$\varepsilon \approx \begin{bmatrix} \varepsilon_1 & j\varepsilon_2 & 0 \\ -j\varepsilon_2 & \varepsilon_1 & 0 \\ 0 & 0 & \varepsilon_1 \end{bmatrix}. \quad (3.9)$$

This notation is widely used in the literature devoted to the magneto-optical effects. In this work, we will keep normal Cartesian notation as is written in Eq. (3.1). However, in the case

of microscopic theory of permittivity tensor, we will sometimes use the special form (3.9) to consistently compare our results with those published in literature. Owing to the practical use in magneto-optical calculations, we focus ourselves here to the permittivity tensor, although the same symmetry arguments hold also for the complex optical susceptibility tensor χ and complex optical conductivity tensor σ .

Reflections by any plane containing the principal axis do not belong to the symmetry group of uniform magnetization. They corresponds to the magnetization reversal

$$\boldsymbol{\varepsilon}(\mathbf{M}) = \begin{bmatrix} -\cos 2\Phi & \sin 2\Phi & 0 \\ \sin 2\Phi & \cos 2\Phi & 0 \\ 0 & 0 & 1 \end{bmatrix} \begin{bmatrix} \varepsilon_{xx} & \varepsilon_{xy} & 0 \\ -\varepsilon_{xy} & \varepsilon_{xx} & 0 \\ 0 & 0 & \varepsilon_{zz} \end{bmatrix} \begin{bmatrix} -\cos 2\Phi & \sin 2\Phi & 0 \\ \sin 2\Phi & \cos 2\Phi & 0 \\ 0 & 0 & 1 \end{bmatrix}. \quad (3.10)$$

Thanks to the cylindrical symmetry, the result of the transformation does not depend on the angle Φ , which specifies the orientation of the reflection planes [15]. Equation (3.10) gives the following expressions

$$\varepsilon_{xx}(M_z) = \varepsilon_{xx}(-M_z), \quad (3.11)$$

$$\varepsilon_{zz}(M_z) = \varepsilon_{zz}(-M_z), \quad (3.12)$$

$$\varepsilon_{xy}(M_z) = -\varepsilon_{xy}(-M_z) = -\varepsilon_{yx}(M_z). \quad (3.13)$$

From these equations, we can deduce that in an originally isotropic magnetized material, the diagonal and off-diagonal elements of the permittivity tensor are even and odd functions of magnetization M . Thus without the magnetic field the off-diagonal elements vanish. These results are consistent with Onsager principle (3.6).

Similarly, the symmetry arguments can be applied for the case of in-plane magnetization and thereby one can derive the form of the permittivity tensor when the magnetization vector is parallel to the y axis

$$\boldsymbol{\varepsilon}_L = \begin{bmatrix} \varepsilon_{xx} & 0 & -\varepsilon_{zx} \\ 0 & \varepsilon_{xx} & 0 \\ \varepsilon_{zx} & 0 & \varepsilon_{zz} \end{bmatrix} \approx \begin{bmatrix} \varepsilon_1 & 0 & -j\varepsilon_2 \\ 0 & \varepsilon_1 & 0 \\ j\varepsilon_2 & 0 & \varepsilon_1 \end{bmatrix}. \quad (3.14)$$

3.2 Microscopic theory of material tensors

As was already mentioned, the material tensors carry the information about the microscopical properties of investigated material due to its response to an electromagnetic wave. To obtain the information about the diagonal elements of these tensors is the aim of spectroscopic ellipsometry, while for the determination of off-diagonal elements one can use magneto-optical

3.2. MICROSCOPIC THEORY OF MATERIAL TENSORS

spectroscopy (in this case called magneto-optical ellipsometry [23]). To assign the experimental data to microscopic processes in the material, various models describing the interaction between the light wave and the matter have been developed. In this section, we make a brief introduction into the microscopic interpretations of permittivity tensor.

3.2.1 Lorentz model

The Lorentz model represents the simplest microscopic approach to the medium response to an electromagnetic wave. It describes an interaction of the electromagnetic wave with elastically bounded electrically charged point particle situated in homogeneous, time independent magnetic field. The particle, which is in our case an electron, has a finite relaxation time τ . This simple model provides essential information about the spectra of the permittivity tensor, although a rigorous account would require the relativistic quantum theory (which is, however, beyond the classical physics).

Single particle classical Hamiltonian of the system can be written as

$$H(\mathbf{r}, \mathbf{p}, t) = \frac{1}{2m} [\mathbf{p} - q\mathbf{A}(\mathbf{r}, t)]^2 + qU(\mathbf{r}, t) + V(\mathbf{r}), \quad (3.15)$$

where

$$V(\mathbf{r}) = \frac{1}{2}m\omega_0^2 r^2 \quad (3.16)$$

is the central parabolic potential and m , q , \mathbf{r} and \mathbf{p} denotes the particles mass, charge, coordinate and momentum, respectively. Considering the classical Hamilton equations and introducing a phenomenological viscous damping term

$$\Gamma \frac{d\mathbf{r}}{dt} = \tau^{-1}, \quad (3.17)$$

one can derive the equation of motion for the charged particle bound in a parabolic potential excited by the electric field component¹ of the electromagnetic wave propagating along the z axis of the Cartesian coordinate system in the external magnetic field $\mathbf{B}_E = (0, 0, -B_z)$ [15, 24]

$$m \frac{\partial^2 \mathbf{r}}{\partial t^2} + m\Gamma \frac{\partial \mathbf{r}}{\partial t} + m\omega_0^2 \mathbf{r} - q \frac{\partial \mathbf{r}}{\partial t} \times \mathbf{B}_E = qE_0 e^{j\omega t}. \quad (3.18)$$

This equation can be decomposed into three scalar components

$$\frac{\partial^2 x}{\partial t^2} + \Gamma \frac{\partial x}{\partial t} + \omega_0^2 x - \omega_c \frac{\partial y}{\partial t} = qE_{0x} \frac{e}{m} e^{j\omega t}, \quad (3.19)$$

$$\frac{\partial^2 y}{\partial t^2} + \Gamma \frac{\partial y}{\partial t} + \omega_0^2 y + \omega_c \frac{\partial x}{\partial t} = qE_{0y} \frac{e}{m} e^{j\omega t}, \quad (3.20)$$

$$\frac{\partial^2 z}{\partial t^2} + \Gamma \frac{\partial z}{\partial t} + \omega_0^2 z = qE_{0z} \frac{e}{m} e^{j\omega t}, \quad (3.21)$$

¹We neglected the interaction of the magnetic field of the electromagnetic wave with the particle, since at optical frequencies this interaction is very small.

where ω_0 denotes the natural frequency and $\omega_c = -qB_z/m$ denotes the cyclotron frequency of electron motion in the magnetic field. The last equation can be easily solved for $z = z_0 e^{j\omega t}$. Therefore

$$z_0 = \frac{q}{m} \frac{E_{0z}}{\omega_0^2 - \omega^2 + i\Gamma\omega}. \quad (3.22)$$

Taking into account the definition of the average dipole moment per unit volume

$$\mathbf{P} = Nq\mathbf{r} = \varepsilon_0\boldsymbol{\chi}\mathbf{E} \quad (3.23)$$

and Eq. (3.4) we can express the relative permittivity as

$$\varepsilon_{ij} = \frac{Ne}{\varepsilon_0} \frac{\partial r_i}{\partial E_j} + \delta_{ij}, \quad (3.24)$$

where ε_0 is the permittivity of vacuum. Substituting Eq. (3.22) into (3.24) we derive the expression for the diagonal element of permittivity tensor

$$\varepsilon_{zz} = 1 + \frac{Ne^2}{m\varepsilon_0} \frac{1}{\omega_0^2 - \omega^2 + i\Gamma\omega} = 1 + \omega_p^2 \frac{1}{\omega_0^2 - \omega^2 + i\Gamma\omega}. \quad (3.25)$$

This is a well-known classical formula describing the permittivity of an isotropic absorbing medium [25], where ω_p is the so-called plasma frequency. The situation in the case ε_{xx} , ε_{yy} , and ε_{xy} is more complicated, since the magnetic field \mathbf{B}_E couples the motions in the x and y directions (see Eqs. (3.19) and (3.20)). This leads to the optical anisotropy expressed by following tensor elements

$$\varepsilon_{xx} = \varepsilon_{yy} = 1 + \omega_p^2 \frac{\omega_0^2 - \omega^2 + i\Gamma\omega}{(\omega_0^2 - \omega^2 + i\Gamma\omega) - \omega_c^2 \omega^2}, \quad (3.26)$$

$$\varepsilon_{xy} = -\varepsilon_{yx} = \omega_p^2 \frac{i\omega\omega_c}{(\omega_0^2 - \omega^2 + i\Gamma\omega) - \omega_c^2 \omega^2}. \quad (3.27)$$

These results are consistent with the permittivity tensor form (3.8) obtained by utilizing the symmetry arguments. In the case of isotropic medium without magnetic field ($\omega_c \rightarrow 0$), the diagonal elements have the same form of ε_{zz} and off-diagonal elements vanish.

3.2.2 Semiclassical theory of material tensors

Semiclassical theories of magneto-optical interactions were developed to provide a deeper insight in the problem of the interaction between electromagnetic wave and magnetically ordered material. They usually treat the action of classical electromagnetic radiation on a quantum system. In this description, concepts of electron spin and spin orbit coupling are essential to deal with. Magneto-optical effects result from the splitting of the ground or excited state energy levels of optical transitions due to an applied field or magnetization. In the magneto-optical

3.2. MICROSCOPIC THEORY OF MATERIAL TENSORS

effects a difference in the optical constants is impressed on the right and left handed circularly polarized waves, which would be zero without \mathbf{H} or \mathbf{M} .

The theory of the response of an atomic system to electromagnetic plane waves has been described in details in literature [26]. The pioneering work dealing with the description of magneto-optical effects within the semiclassical theory was published by Shen [27]. He considered the response to circularly polarized light of a single atomic system. He employed the density matrix formalism to obtain the final expression for electronic transitions with the final linewidth in terms of the optical susceptibility tensor. Afterwards, the semiclassical model was employed by Kahn *et al.* [28], Crosley *et al.* [29], Wittekoek *et al.* [30], LeGall *et al.* [31], Suits [5], and others. It is beyond the scope of this work to derive the complete theory, thus one can find more details in references listed above. Since most of the analyses of the magneto-optical properties of magnetic oxides have been done using the theory employed first by Kahn *et al.*, to be consistent with previously published interpretation, we will also follow this work. Therefore we have to note that the following description will be done in terms of the special form of permittivity tensor (3.9).

Since the contributions of allowed magnetic-dipole transitions are usually too small [32] to account in the interpretation, we limit ourselves to electric-dipole transitions, which have considerably greater oscillator strengths. Let's now consider a material with N saturated spin systems per unit volume in ground states $|g\rangle$. Then the contributions of these transitions to the diagonal elements of permittivity tensor can be written as [33]

$$\begin{aligned}\varepsilon_1(\omega) &= 1 + \sum_e \varepsilon_{1e} = 1 + \sum_{e,\nu} \varepsilon_{1e(\nu)} \\ &= 1 + \frac{4\pi Nq^2}{m} \sum_{e,\nu} f_{ge(\nu)} \frac{\omega_{ge(\nu)}^2 - \omega^2 + \Gamma_{ge(\nu)}^2 - 2j\omega\Gamma_{ge(\nu)}}{(\omega_{ge(\nu)}^2 - \omega^2 + \Gamma_{ge(\nu)}^2)^2 + 4\omega^2\Gamma_{ge(\nu)}^2},\end{aligned}\quad (3.28)$$

where

$$f_{ge(\nu)} = \frac{2m\omega_{ge(\nu)}}{\hbar} |\langle g|x|e(\nu)\rangle|^2 \quad (3.29)$$

is the oscillator strength of the transition $|g\rangle \rightarrow |e(\nu)\rangle$ [28] which occurs at resonance frequency $\omega_{ge(\nu)}$, and $\Gamma_{ge(\nu)}$ is the corresponding line-width. The summation is taken over all excited states $|e(\nu)\rangle$, where ν numbers the sublevels of $|e\rangle$ which are split by the spin-orbit interaction.

If the condition $\Gamma_{ge(\nu)}/\omega_{ge(\nu)} \ll 1$ is valid and $\varepsilon''_{1e(\nu)}$ exhibits the maximum for $\omega = \omega_{e(\nu)}$, the oscillator strength is given to a good approximation by

$$f_{ge(\nu)} \approx \frac{m}{2\pi Nq^2 L} \omega_{ge(\nu)} \Gamma_{ge(\nu)} (\varepsilon''_{1e(\nu)})_{max}. \quad (3.30)$$

Here L is the Lorentz local field correction, $L = [(n^2 + 2)^2/9]$ [34]. This correction should be applied for materials which are not satisfying the condition $|\varepsilon_1 - 1| \ll 1$. Since all systems are initially in the ground states, we will omit the subscripts g in following expressions.

The contributions of electric dipole transitions to the off-diagonal permittivity tensor elements can be written as

$$\begin{aligned}\varepsilon_2(\omega) &= 1 + \sum_e \varepsilon_{2e} = 1 + \sum_{e,\nu} \varepsilon_{2e(\nu)} \\ &= \frac{2\pi Nq^2}{m} \sum_{e,\nu} \frac{f_{-e(\nu)} - f_{+e(\nu)}}{\omega^2 - \omega_{e(\nu)}^2 - \Gamma_{e(\nu)}^2 - 2j\omega\Gamma_{e(\nu)}} \frac{\omega - j\Gamma_{e(\nu)}}{\omega_{e(\nu)}},\end{aligned}\quad (3.31)$$

where

$$f_{\pm e(\nu)} = \frac{m\omega_{e(\nu)}}{\hbar} |\langle g|x \pm jy|e(\nu)\rangle|^2 \quad (3.32)$$

are the oscillator strengths for circularly polarized transitions.

3.2.3 Diamagnetic and paramagnetic transitions

In ferromagnetic materials the direct effect of the magnetic field is much smaller than the effects of spin-orbit interactions when spins are oriented [35]. Therefore in these materials the dominant magneto-optical effects result from the interaction between the orbital motion and the spin orientation. It is appropriate to neglect the direct effect of an external magnetic field [28] and consider only the net spin alignment. The spin-orbit interaction enables the electron system to distinguish between two senses of circularly polarization for electric-dipole transitions. Without the spin-orbit interaction $\omega_e(\nu)$ and $\Gamma_e(\nu)$ are independent of ν . Moreover, the sums over the oscillator strengths, $\sum_\nu f_{\pm e(\nu)}$, are identical and Eq. (3.31) becomes zero. Thus no magneto-optical effect can be observed². Historically there are two special types of electron transitions observed in magneto-optical spectra, each with different line shape, which were of particular interest. The spectral shapes of both types of transitions are shown in Fig. 3.1.

Type I: diamagnetic transition: In this case the spin-orbit coupling splits the degeneracy of excited states. Thus $|e(+)\rangle \neq |e(-)\rangle$ and the energy difference can be expressed in the first order in M as

$$\Delta E = 2\hbar\Delta\omega_e = 2\hbar(\omega_{e(+)} - \omega_{e(-)}) \quad (3.33)$$

However the oscillator strength remains the same for transition to both excited states. Therefore we can derive from the Eq. (3.31) an expression

$$\varepsilon_{2e} = -\Gamma_e \Delta\omega_e (\varepsilon''_{1e})_{max} \times \frac{(\omega - \omega_e)^2 - (\Gamma_e^2 + \Delta\omega_e^2) + 2j\Gamma_e(\omega - \omega_e)}{[(\omega - \omega_e)^2 - (\Gamma_e^2 + \Delta\omega_e^2)]^2 + 4\Gamma_e^2(\omega - \omega_e)^2}, \quad (3.34)$$

where

$$\omega_e = \frac{1}{2}(\omega_{e+} + \omega_{e-}), \quad (3.35)$$

$$\Gamma_{e+} = \Gamma_{e-} = \Gamma_e, \quad (3.36)$$

²In the real situation spin-independent contributions to ε_2 can be also found within the electric-dipole approximation. However, they are several orders of magnitude smaller than those being discussed.

3.2. MICROSCOPIC THEORY OF MATERIAL TENSORS

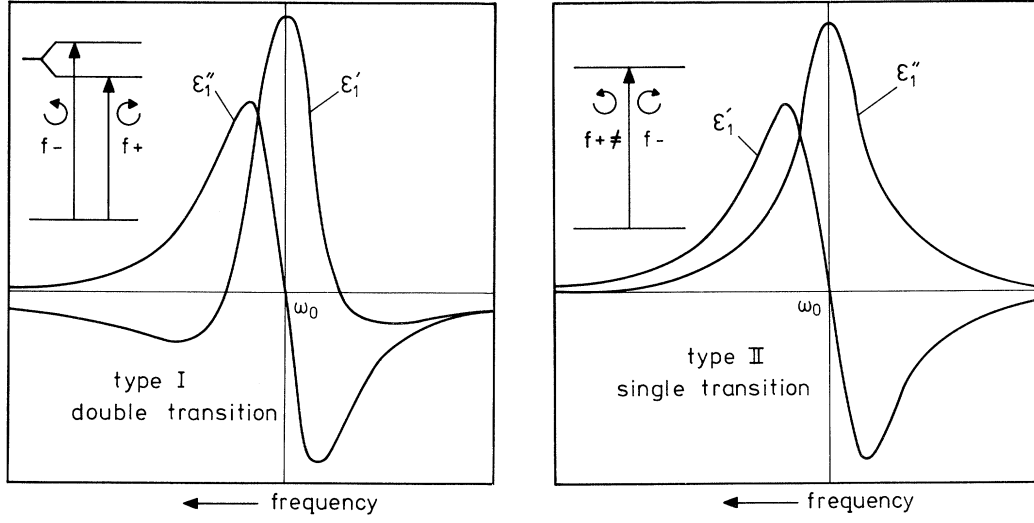


Figure 3.1: Spectral shapes of diamagnetic (left side) and paramagnetic (right side) transitions [30].

and the identity

$$\frac{\omega - j\Gamma_e}{\omega^2 - \omega_e^2 - \Gamma_e^2 - 2j\omega\Gamma_e} = \frac{1}{2} \left(\frac{1}{\omega_e + (\omega - j\Gamma_e)} - \frac{1}{\omega_e - (\omega - j\Gamma_e)} \right) \quad (3.37)$$

was used.

From Eq. (3.34), it follows that ε'_{2e} and ε''_{2e} are even and odd functions of $(\omega - \omega_e)$. Moreover, if $\Delta\omega_e \ll \Gamma_e$, the real and imaginary part of ε_{2e} exhibit the spectral shapes shown in Fig. 3.1. The maximum $\varepsilon'_{2e}(\omega)$ occurs for $\omega = \omega_0$ and is given by

$$(\varepsilon'_{2e})_{max} = \frac{\Delta\omega_e}{\Gamma_e} (\varepsilon''_{1e})_{max} \quad (3.38)$$

to first order in $\Delta\omega_e/\Gamma_e$ and Γ_e/ω_e . With help of the latter equation, we can rewrite Eq. (3.34) into the form suitable for computer fitting

$$\varepsilon_{2e} = -\Gamma_e^2 (\varepsilon'_{2e})_{max} \frac{(\omega - \omega_e)^2 - \Gamma_e^2 + 2j\Gamma_e(\omega - \omega_e)}{[(\omega - \omega_e)^2 + \Gamma_e^2]^2}, \quad (3.39)$$

which describes the contribution of the diamagnetic transition into the spectrum of ε_2 .

Type II: paramagnetic transition: The spin-orbit coupling induces the difference between $f_{+e(\nu)}$ and $f_{-e(\nu)}$. This is caused by the difference in the ground state population due to its spin-orbit splitting. We can therefore write

$$\xi_e \equiv \frac{f_{-e} - f_{+e}}{f_{-e} + f_{+e}}. \quad (3.40)$$

The quantity ξ_e is called fractional dichroism.

Similarly to the case of diamagnetic transition, we can derive the expression

$$\varepsilon_{2e} = -2\xi_e \Gamma_e (\varepsilon_{1e}'')_{max} \times \frac{\omega(\omega^2 - \omega_e^2 + \Gamma_e^2) - j\Gamma_e(\omega^2 + \omega_e^2 - \Gamma_e^2)}{(\omega^2 - \omega_e^2 - \Gamma_e^2) + 4\Gamma_e^2\omega^2}. \quad (3.41)$$

The spectral dependences of the real and imaginary part of ε_{2e} are opposite to those for the diamagnetic shape. The maximum in $\varepsilon_{2e}''(\omega)$ occurs for $\omega = \omega_e$ and is given by

$$(\varepsilon_{2e}'')_{max} = \xi_e (\varepsilon_{1e}'')_{max}, \quad (3.42)$$

which allows to transform the Eq. (3.41) in to the form

$$\varepsilon_{2e} = -2\Gamma_e (\varepsilon_{2e}'')_{max} \frac{\omega(\omega^2 - \omega_e^2 + \Gamma_e^2) - j\Gamma_e(\omega^2 + \omega_e^2 - \Gamma_e^2)}{(\omega^2 - \omega_e^2 - \Gamma_e^2) + 4\Gamma_e^2\omega^2}, \quad (3.43)$$

which describes the contribution of paramagnetic transition into the spectrum of ε_2 and is easy to use in the computer fitting.

For the analysis of magneto-optical spectra observed in magnetic oxides, where the main contribution to ε_2 is due to d electrons, this theory functions well. In experimental chapters, Eq. (3.39) and (3.43) were used to analyze the spectral dependencies of ε_2 obtained from experiment.

4 Optics of magnetic materials

In this chapter, we outline the response of magnetic media to electromagnetic waves. In the beginning we derive the wave equation for an anisotropic medium characterized by a general permittivity tensor and subsequently find the solutions. Then this approach is applied to the propagation of electromagnetic wave parallel to the magnetization. We also derive the general expressions for the complex polar Kerr effect on the bulk material, which are widely used to obtain the off-diagonal elements of permittivity tensor.

In the second part of this chapter, we introduce the generalized Yeh's 4x4 matrix formalism for absorbing layered magnetically ordered media as a unified approach to the problem of electromagnetic response in magnetized anisotropic multilayers. We define general reflection and transmission coefficients, which allow us to calculate ellipsometric and magneto-optical quantities.

4.1 Wave equation in anisotropic medium

Light propagation in anisotropic media can be described using the wave equation. To derive its form, we have to start from the set of Maxwell's equations without sources

$$\nabla \times \mathbf{H} - \frac{\partial \mathbf{D}}{\partial t} = 0, \quad (4.1)$$

$$\nabla \cdot \mathbf{D} = 0, \quad (4.2)$$

$$\nabla \times \mathbf{E} + \frac{\partial \mathbf{B}}{\partial t} = 0, \quad (4.3)$$

$$\nabla \cdot \mathbf{B} = 0. \quad (4.4)$$

At optical frequencies we consider $\mu = \mu_{vac}$. We rewrite Eq. (4.1) in to the form

$$\nabla \times \mathbf{B} = c^{-2} \epsilon \frac{\partial \mathbf{E}}{\partial t}, \quad (4.5)$$

where $c = (\epsilon_{vac} \mu_{vac})^{-1/2}$ denotes the light wave phase velocity in vacuum and ϵ is the relative permittivity tensor. By eliminating the magnetic flux density, \mathbf{B} , we obtain the wave equation for the electric field vector \mathbf{E}

$$\nabla \times (\nabla \times \mathbf{E}) = -c^{-2} \epsilon \frac{\partial^2 \mathbf{E}}{\partial t^2}. \quad (4.6)$$

The solution to this equation can be written in the form of a monochromatic plane wave with \mathbf{E} given by

$$\mathbf{E} = \mathbf{E}_0 \exp[j(\omega t - \boldsymbol{\gamma} \cdot \mathbf{r})], \quad (4.7)$$

where \mathbf{E}_0 is the complex vector amplitude of the wave electric field, ω is the angular frequency and $\boldsymbol{\gamma}$ is the propagation wavevector. Evaluating the double vector multiplication $\nabla \times (\nabla \times \mathbf{E})$ and substituting Eq. (4.7) into Eq. (4.6) one can derive the wave equation in the form

$$\boldsymbol{\gamma}^2 \mathbf{E}_0 - \boldsymbol{\gamma}(\boldsymbol{\gamma} \cdot \mathbf{E}_0) = \frac{\omega^2}{c^2} \boldsymbol{\varepsilon} \mathbf{E}_0. \quad (4.8)$$

The wavevector can be written in Cartesian components as

$$\boldsymbol{\gamma} = \frac{\omega}{c} (N_x \hat{\mathbf{x}} + N_y \hat{\mathbf{y}} + N_z \hat{\mathbf{z}}), \quad (4.9)$$

and the vector wave equation (4.8) can be written in the matrix form

$$\begin{bmatrix} \varepsilon_{xx} - N_y^2 - N_z^2 & \varepsilon_{xy} + N_x N_y & \varepsilon_{xz} + N_x N_z \\ \varepsilon_{yz} - N_x N_y & \varepsilon_{yy} - N_x^2 - N_z^2 & \varepsilon_{yz} + N_y N_z \\ \varepsilon_{zx} + N_x N_z & \varepsilon_{zy} + N_y N_z & \varepsilon_{zz} - N_x^2 - N_y^2 \end{bmatrix} \begin{bmatrix} E_{0x} \\ E_{0y} \\ E_{0z} \end{bmatrix} = 0. \quad (4.10)$$

For given values of N_x and N_y the equation system (4.10) gives the eigenvalues N_{zj} , $j = 1, \dots, 4$, which are the solutions of the quartic form eigenvalue equation [15]. However the problem can be simplified, without any loss of generality, by eliminating the Cartesian component of the complex propagation vector parallel to the interfaces and normal to plane of incidence. For our purpose, we choose the coordinate system for which $N_x = 0$. Then the wavevector is reduced to

$$\boldsymbol{\gamma} = \frac{\omega}{c} (N_y \hat{\mathbf{y}} + N_z \hat{\mathbf{z}}), \quad (4.11)$$

and the matrix wave equation (4.10) has the form

$$\begin{bmatrix} (N_y^2 + N_z^2 - \varepsilon_{xx}) & -\varepsilon_{xy} & -\varepsilon_{xz} \\ -\varepsilon_{yz} & (N_x^2 + N_z^2 - \varepsilon_{yy}) & -(N_y N_z + \varepsilon_{yz}) \\ -\varepsilon_{zx} & -(N_y N_z + \varepsilon_{zy}) & (N_y^2 - \varepsilon_{zz}) \end{bmatrix} \begin{bmatrix} E_{0x} \\ E_{0y} \\ E_{0z} \end{bmatrix} = 0. \quad (4.12)$$

The eigenvalue equation for this system of equations can be written as

$$\begin{aligned} & \varepsilon_{zz} N_z^4 + (\varepsilon_{yz} + \varepsilon_{zy}) N_y N_z^3 \\ & - [\varepsilon_{yy}(\varepsilon_{zz} - N_y^2) + \varepsilon_{zz}(\varepsilon_{xx} - N_y^2) - \varepsilon_{xz}\varepsilon_{zx} - \varepsilon_{yz}\varepsilon_{zy}] N_z^2 \\ & - [(\varepsilon_{xx} - N_y^2)(\varepsilon_{yz} + \varepsilon_{zy}) - \varepsilon_{xy}\varepsilon_{zx} - \varepsilon_{yz}\varepsilon_{xz}] N_y N_z \\ & + \varepsilon_{yy}[(\varepsilon_{xx} - N_y^2)(\varepsilon_{zz} - N_y^2) - \varepsilon_{xz}\varepsilon_{zx}] - \varepsilon_{xy}\varepsilon_{yx}(\varepsilon_{zz} - N_y^2) \\ & - \varepsilon_{yz}\varepsilon_{zy}(\varepsilon_{xx} - N_y^2) + \varepsilon_{xy}\varepsilon_{zx}\varepsilon_{yz} + \varepsilon_{yx}\varepsilon_{xz}\varepsilon_{zy} = 0. \end{aligned} \quad (4.13)$$

4.2. PROPAGATION PARALLEL TO THE MAGNETIZATION VECTOR

In the latter equation, the only unknown are the eigenvalues of N_z , while other parameters describe the material properties and the value of N_y can be easily obtained from Snell law

$$\boldsymbol{\gamma} \cdot \hat{\boldsymbol{y}} = \frac{\omega}{c} N_y. \quad (4.14)$$

If one considers an incident light coming from a vacuum space, N_y simply represents the sine of the incident angle.

Solving the Eq. (4.13), one can obtain the eigenmodes of the propagation of the light wave inside an anisotropic medium. These eigenmodes have the form

$$\mathbf{e}_j = C_j \begin{bmatrix} -\varepsilon_{xy}(\varepsilon_{zz} - N_y^2) + \varepsilon_{xz}(\varepsilon_{zy} - N_y N_{zj}) \\ (\varepsilon_{zz} - N_y^2)(\varepsilon_{xx} - N_y^2 - N_{zj}^2) - \varepsilon_{xz}\varepsilon_{zx} \\ -(\varepsilon_{xx} - N_y^2 - N_{zj}^2)(\varepsilon_{zy} + N_y N_{zj}) + \varepsilon_{zx}\varepsilon_{xy} \end{bmatrix}, \quad (4.15)$$

where C_j is the corresponding normalization coefficient. Derived eigenmodes are not modified during the propagation in the medium. With respect to the linearity of Eq. (4.10) in \mathbf{E} , it is useful to describe the electric field of the plane wave in the basis of eigenmodes. Thus, the electric field takes the form of a linear superposition of obtained eigenmodes

$$\mathbf{E} = \sum_{j=1}^4 E_{0j} \mathbf{e}_j \exp\{j\omega t - j\frac{\omega}{c}[N_y y + N_{zj} z]\}. \quad (4.16)$$

Equations (4.10) and (4.12) hold for a general case with an arbitrary orientation of magnetization vector and their solution is rather difficult. Fortunately, in real situations the general permittivity tensor is reduced to a special form. Therefore the Eq. (4.13) often becomes bi-quadratic and can be solved easily. An analytical method to solve the forth-order equation was proposed by Mansuripur [36].

4.2 Propagation parallel to the magnetization vector

Now we show the solution to the wave equation for the simplest case, which is the propagation of the light wave in the medium with magnetization vector parallel to the z axis. The permittivity tensor of such medium has the form written in Eq. (3.8). Moreover, this situation corresponds to the normal light incidence for which $N_y = 0$. Hence the matrix wave equation (4.12) transforms into

$$\begin{bmatrix} (N_z^2 - \varepsilon_{xx}) & -\varepsilon_{xy} & 0 \\ \varepsilon_{xy} & (N_z^2 - \varepsilon_{xx}) & 0 \\ 0 & 0 & -\varepsilon_{zz} \end{bmatrix} \begin{bmatrix} E_{0x} \\ E_{0y} \\ E_{0z} \end{bmatrix} = 0, \quad (4.17)$$

which leads to the eigenvalue equation

$$\varepsilon_{zz}[N_z^4 - 2\varepsilon_{xx}N_z^2 + (\varepsilon_{xx}^2 + \varepsilon_{xy}^2)] = 0. \quad (4.18)$$

This equation can be treated as a complex quadratic equation in N_z^2 giving the solutions conventionally distinguished by \pm signs

$$(N_{z\pm})^2 = \varepsilon_{xx} \pm j\varepsilon_{xy}. \quad (4.19)$$

The eigenvalues of the complex index of refraction are independent of the sense of propagation [15]. This behavior is typical for the MO effect linear in magnetization.

It can be shown [15, 24], that the eigenmodes in the medium magnetized parallel to the wave propagation corresponding to eigenvalues derived above are the left and right circularly polarized eigen polarizations. Thus any solution of the vector wave equation (4.6) can be expressed in terms of four complex scalar amplitudes $E_0^{(j)}$, where $j = 1 \dots 4$.

The forward and backward CP waves propagating with wavevectors $\pm \frac{\omega}{c} N_{z+}$ can be expressed as

$$\mathbf{E}_1 = 2^{-1/2}(\hat{\mathbf{x}} + j\hat{\mathbf{y}})E_0^{(1)} \exp \left[j \left(\omega t - N_{z+} \frac{\omega}{c} z \right) \right], \quad (4.20)$$

$$\mathbf{E}_2 = 2^{-1/2}(\hat{\mathbf{x}} - j\hat{\mathbf{y}})E_0^{(2)} \exp \left[j \left(\omega t + N_{z+} \frac{\omega}{c} z \right) \right]. \quad (4.21)$$

To be consistent with the description of classical ellipsometry, we assort the forward propagating wave \mathbf{E}_1 as right circularly polarized (RCP) and backward propagating wave \mathbf{E}_2 as left circularly polarized (LCP). Similarly, we can obtain the waves propagating with wavevectors $\pm \frac{\omega}{c} N_{z-}$

$$\mathbf{E}_3 = 2^{-1/2}(\hat{\mathbf{x}} - j\hat{\mathbf{y}})E_0^{(3)} \exp \left[j \left(\omega t - N_{z-} \frac{\omega}{c} z \right) \right], \quad (4.22)$$

$$\mathbf{E}_4 = 2^{-1/2}(\hat{\mathbf{x}} + j\hat{\mathbf{y}})E_0^{(4)} \exp \left[j \left(\omega t + N_{z-} \frac{\omega}{c} z \right) \right], \quad (4.23)$$

where the solutions denotes LCP forward and RCP backward waves. To describe the propagation in the isotropic media, one can proceed similarly with $N_{z+} = N_{z-}$, which is the consequence of the isotropy when $\varepsilon_{xy} = 0$.

4.3 Polar Kerr effect at normal light incidence

As follows from previous sections, a general solution to the eigenvalue and eigenmode problem can be rather difficult if one solves it generally. However in special geometries of the experimental setup the calculation becomes more simple. The simplest case is the semi-infinite

4.3. POLAR KERR EFFECT AT NORMAL LIGHT INCIDENCE

magnetic material (suitable for bulk) magnetized normally to the surface interface at normal incidence. Therefore in this calculation, we will consider only the interface between vacuum and the material. The incident and reflected fields are related by Jones matrix of reflection. Owing to the geometry of the problem, the Jones matrix has the form shown in Tab. 2.3. Moreover, due to the normal incidence, the symmetry of the problem is higher and $r_{yy} = r_{xx}$. Thus we can write

$$\begin{bmatrix} J_x^{(r)} \\ J_y^{(r)} \end{bmatrix} = \begin{bmatrix} r_{xx} & r_{xy} \\ -r_{xy} & r_{xx} \end{bmatrix} \begin{bmatrix} J_x^{(i)} \\ J_x^{(i)} \end{bmatrix}. \quad (4.24)$$

As was shown in previous sections, the eigenmodes for the propagation along the M are circularly polarized and the propagation of these modes in the medium is described in terms of the complex refractive indices N_{z+} and N_{z-} . Moreover, RCP and LCP waves of equal amplitudes have different Fresnel reflection coefficients at the interface with vacuum [37, 4]

$$r_{\pm} = \frac{1 - N_{\pm}}{1 + N_{\pm}}. \quad (4.25)$$

Therefore it is useful to transform the Jones matrix of reflection into the representation of circular polarizations

$$\begin{aligned} 2^{-1/2} \begin{bmatrix} 1 & -j \\ 1 & j \end{bmatrix} \begin{bmatrix} r_{xx} & r_{xy} \\ -r_{xy} & r_{xx} \end{bmatrix} 2^{-1/2} \begin{bmatrix} 1 & 1 \\ j & -j \end{bmatrix} &= \begin{bmatrix} r_{xx} + jr_{xy} & 0 \\ 0 & r_{xx} - jr_{xy} \end{bmatrix} \\ &\equiv \begin{bmatrix} r_+ & 0 \\ 0 & r_- \end{bmatrix}. \end{aligned} \quad (4.26)$$

We also transform to the CP representation the Jones vector of reflected wave

$$\begin{bmatrix} J_+^{(r)} \\ J_-^{(r)} \end{bmatrix} = 2^{-1/2} \begin{bmatrix} J_x^{(r)} - jJ_y^{(r)} \\ J_x^{(r)} + jJ_y^{(r)} \end{bmatrix} = \begin{bmatrix} r_+ & 0 \\ 0 & r_- \end{bmatrix} 2^{-1/2} \begin{bmatrix} J_x^{(i)} - jJ_y^{(i)} \\ J_x^{(i)} + jJ_y^{(i)} \end{bmatrix}. \quad (4.27)$$

Therefore we can write the Eq. (4.24) in the circular representation as

$$\begin{bmatrix} J_+^{(r)} \\ J_-^{(r)} \end{bmatrix} = 2^{-1/2} \begin{bmatrix} r_+ & 0 \\ 0 & r_- \end{bmatrix} \begin{bmatrix} 1 \\ 1 \end{bmatrix} J_x^{(i)}. \quad (4.28)$$

The Jones vector of the reflected wave can be transformed back to the Cartesian representation with help of r_+ and r_- by the following expression

$$\begin{bmatrix} J_x^{(r)} \\ J_y^{(r)} \end{bmatrix} = \frac{1}{2} \begin{bmatrix} r_+ + r_- \\ j(r_+ - r_-) \end{bmatrix} J_x^{(i)}. \quad (4.29)$$

Using the latter equation with help of Eqs. (2.22) and (2.37), one can describe the polarization state of reflected wave by the complex number

$$\chi_r^{(pol)} = \frac{J_y^{(r)}}{J_x^{(r)}} = \frac{j(r_+ - r_-)}{r_+ + r_-} = j \frac{N_+ - N_-}{N_+ N_- - 1} \approx \theta_K^{(pol)} + j\epsilon_K^{(pol)}. \quad (4.30)$$

To relate the polar Kerr rotation and ellipticity to the material properties (described here by the permittivity tensor components) we assume that $\varepsilon_{xy} \ll \varepsilon_{xx}$ and use the following equations [15]

$$N_+ - N_- \approx j\varepsilon_{xy}\varepsilon_{xx}^{-1/2}, \quad (4.31)$$

$$N_+N_- \approx \varepsilon_{xx} = N^2 = (n - jk)^2. \quad (4.32)$$

Therefore

$$\chi_r^{(pol)} \approx \theta_K^{(pol)} + j\epsilon_K^{(pol)} \approx \frac{\varepsilon_{xy}}{\sqrt{\varepsilon_{xx}}(1 - \varepsilon_{xx})}. \quad (4.33)$$

Since ε_{xx} and ε_{xy} are complex numbers, $\varepsilon = \varepsilon' - j\varepsilon''$, for practical purposes it is useful to express Eq. (4.33) in terms of ε' and ε'' . Assuming $\sqrt{\varepsilon_{xx}} = (n - jk)$, where n and k are refractive index and index of absorption of magnetic materials, we can write the expressions for the polar Kerr rotation and ellipticity for the reflection at a single interface as

$$\theta^{(pol)} \approx \frac{\varepsilon'_{xy}(3nk^2 - n^3 + n) + \varepsilon''_{xy}(3n^2k - k^3 - k)}{(n^2 + k^2)[(n^2 + k^2) - 2n^2 + 2k^2 + 1]}, \quad (4.34)$$

$$\epsilon^{(pol)} \approx \frac{\varepsilon''_{xy}(3nk^2 - n^3 + n) - \varepsilon'_{xy}(3n^2k - k^3 - k)}{(n^2 + k^2)[(n^2 + k^2) - 2n^2 + 2k^2 + 1]}. \quad (4.35)$$

Eqs. (4.33), or (4.34) and (4.35) can be used to determine the off-diagonal elements of the dielectric tensor from experimental polar Kerr spectra, utilizing the knowledge of the dispersion relations of either n and k or ε_{xx} . This is often used for the magneto-optical characterization of magnetic materials, because as was shown in previous sections, the dispersion relations of ε_{xy} carry the information about electron transitions inside the matter. In practice, one can often use the optical constant taken from literature. This of course affects the accuracy of the determination of ε_{xy} since it depends on the accuracy of the optical constants. For better results, magneto-optical spectroscopy is often used along with the spectroscopic ellipsometry, which ensures the determination of optical properties of investigated material.

The calculation performed above works reasonably when the thickness of the material is much larger than the penetration depth of the light wave. Therefore it is suitable for bulk materials. However, when the thickness of investigated sample is comparable or smaller than the penetration depth (usual case of thin films), a more sophisticated model of a thin layer on a substrate is necessary to consider. In the next section we introduce a general formalism which is suitable for layered structures.

4.4 Anisotropic multilayers

There have been various approaches for macroscopic description of magneto-optical effects [36, 38, 39, 40, 41, 42, 43] since the systematic interest in magneto-optics started in early 1960's.

4.4. ANISOTROPIC MULTILAYERS

Here, we will describe the interaction of plane optical waves within anisotropic layered media with help of the 4x4 matrix formalism introduced by Yeh [44] for non-absorbing materials and extended in 1986 to absorbing media for the description of magneto-optical effects. This formalism is very powerful since it treats an arbitrary permittivity tensor without approximations. This is a big advantage which makes it suitable for numerical modelling.

We consider the planar structure, consisting of N layers separated by parallel interfaces normal to the z axis, sandwiched between two half spaces. This is schematically shown in Fig. 4.1. Each layer is homogeneous and characterized by a general complex permittivity tensor $\varepsilon^{(n)}$ and thickness $t^{(n)}$, ($n = 1 \dots N$). Owing to the Snell law, the components of the propagation vector γ parallel to the interface planes are invariant, *e. g.* are the same in all layers of the structure. As we have shown in Section 4.1, in any anisotropic medium, the solution to the wave equation (4.12) can be expressed in terms of four eigenmodes corresponding to the four roots of the characteristic equation. Therefore the calculation procedure is following.

For all layers (including two sandwiching half spaces), we have to find the components N_{zj} and corresponding eigenmodes e_j as was already shown in Section 4.1. Afterwards, using the boundary conditions which require a continuity of the tangential components of electric (\mathbf{E}) and magnetic (\mathbf{B}) field vectors at the interfaces, we relate the fields in adjacent layers.

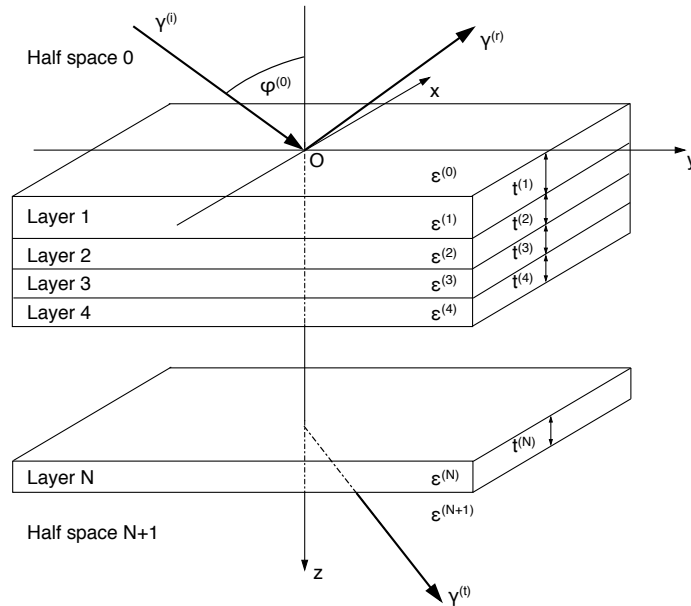


Figure 4.1: Schematic picture of the interaction of polarized optical wave with an anisotropic multilayered structure containing N anisotropic layers, separated by planar interfaces, and characterized by permittivity tensor $\varepsilon^{(n)}$.

Applying this approach recursively to all interfaces we can find the relation between the fields in two half-spaces at boundaries with the multilayered structure. Finally, the fields at the front and the back of the multilayer are related in terms of reflection and transmission coefficients for the eigenmodes in the isotropic half-spaces. From these coefficients one can calculate the magneto-optical and ellipsometric angles.

4.4.1 Matrix representation of multilayered structure

Using the Eq. (4.16), we can write the vector of electric field in n -th layer as

$$\mathbf{E}^{(n)} = \sum_{j=1}^4 E_{0j}^{(n)} \mathbf{e}_j^{(n)} \exp\{j\omega t - j\frac{\omega}{c}[N_y y + N_{zj}^{(n)}(z - z^{(n)})]\}, \quad (4.36)$$

where $z^{(n)}$ denotes the plane between n -th and $(n + 1)$ -th layers, $E_{0j}^{(n)}$ is the complex amplitude of the j -th eigenmode and $\mathbf{e}_j^{(n)}$ is the complex vector specifying the polarization of the eigenmode.

The magnetic field can be obtained with help of the Faraday law

$$\nabla \times \mathbf{E} = -\frac{\partial \mathbf{B}}{\partial t}. \quad (4.37)$$

Thus

$$c\mathbf{B}^{(n)} = \sum_{j=1}^4 E_{0j}^{(n)} \mathbf{b}_j^{(n)} \exp\{j\omega t - j\frac{\omega}{c}[N_y y + N_{zj}^{(n)}(z - z^{(n)})]\}, \quad (4.38)$$

where

$$\mathbf{b}_j^{(n)} = (N_y \hat{\mathbf{y}} + N_{zj} \hat{\mathbf{z}}) \times \mathbf{e}_j^{(n)}. \quad (4.39)$$

The continuity requirement for tangential components of electric and magnetic field vectors at the interface $z = z^{(n)}$ between $(n - 1)$ -th and n -th layers leads to the conditions

$$\sum_{j=1}^4 E_{0j}^{(n-1)} \mathbf{e}_j^{(n-1)} \cdot \hat{\mathbf{x}} = \sum_{j=1}^4 E_{0j}^{(n)} \mathbf{e}_j^{(n)} \cdot \hat{\mathbf{x}} \exp\left(j\frac{\omega}{c} N_{zj}^{(n)} t^{(n)}\right), \quad (4.40)$$

$$\sum_{j=1}^4 E_{0j}^{(n-1)} \mathbf{e}_j^{(n-1)} \cdot \hat{\mathbf{y}} = \sum_{j=1}^4 E_{0j}^{(n)} \mathbf{e}_j^{(n)} \cdot \hat{\mathbf{y}} \exp\left(j\frac{\omega}{c} N_{zj}^{(n)} t^{(n)}\right), \quad (4.41)$$

$$\sum_{j=1}^4 E_{0j}^{(n-1)} \mathbf{b}_j^{(n-1)} \cdot \hat{\mathbf{x}} = \sum_{j=1}^4 E_{0j}^{(n)} \mathbf{b}_j^{(n)} \cdot \hat{\mathbf{x}} \exp\left(j\frac{\omega}{c} N_{zj}^{(n)} t^{(n)}\right), \quad (4.42)$$

$$\sum_{j=1}^4 E_{0j}^{(n-1)} \mathbf{b}_j^{(n-1)} \cdot \hat{\mathbf{y}} = \sum_{j=1}^4 E_{0j}^{(n)} \mathbf{b}_j^{(n)} \cdot \hat{\mathbf{y}} \exp\left(j\frac{\omega}{c} N_{zj}^{(n)} t^{(n)}\right). \quad (4.43)$$

Here, $t^{(n)}$ denotes the thickness of the n -th layer. It is useful to note that the introduction of the layer thickness removed the dependence on the position of the interface on the z axis. Now, the

4.4. ANISOTROPIC MULTILAYERS

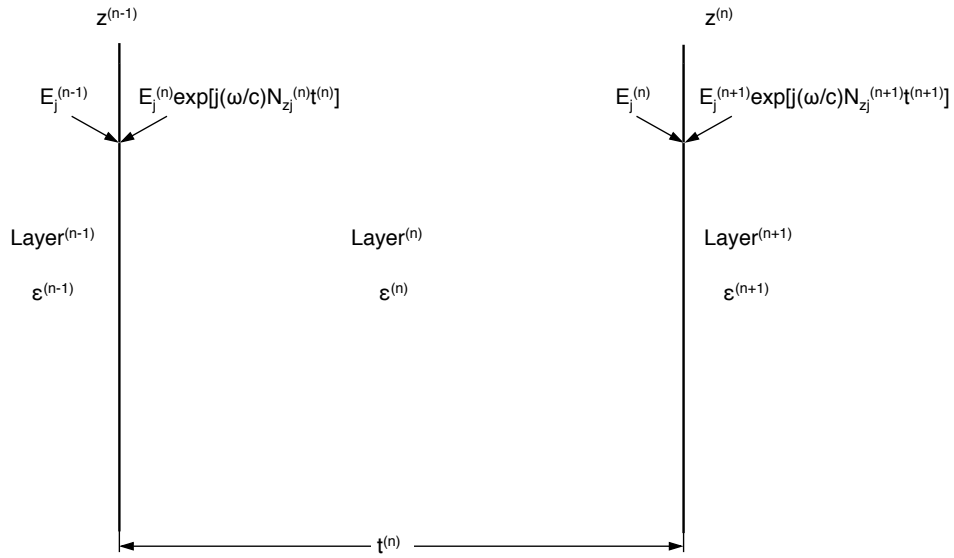


Figure 4.2: Boundary conditions for eigenmodes at both interfaces of the n -th layer.

amplitudes of the electric field vector at the $z^{(n-1)}$ interface in the n -th layer are given by the amplitudes of the electric field vector in the same layer at opposite interface $z^{(n)}$ multiplied by the propagation factor $\exp\left(j\frac{\omega}{c}N_{z_j}^{(n)}t^{(n)}\right)$ (see Fig 4.2).

Equations (4.40) - (4.43) can be rewritten into a matrix notation as

$$\begin{aligned}
 & \begin{bmatrix} \mathbf{e}_1^{(n-1)} \cdot \hat{\mathbf{x}} & \mathbf{e}_2^{(n-1)} \cdot \hat{\mathbf{x}} & \mathbf{e}_3^{(n-1)} \cdot \hat{\mathbf{x}} & \mathbf{e}_4^{(n-1)} \cdot \hat{\mathbf{x}} \\ \mathbf{b}_1^{(n-1)} \cdot \hat{\mathbf{y}} & \mathbf{b}_2^{(n-1)} \cdot \hat{\mathbf{y}} & \mathbf{b}_3^{(n-1)} \cdot \hat{\mathbf{y}} & \mathbf{b}_4^{(n-1)} \cdot \hat{\mathbf{y}} \\ \mathbf{e}_1^{(n-1)} \cdot \hat{\mathbf{y}} & \mathbf{e}_2^{(n-1)} \cdot \hat{\mathbf{y}} & \mathbf{e}_3^{(n-1)} \cdot \hat{\mathbf{y}} & \mathbf{e}_4^{(n-1)} \cdot \hat{\mathbf{y}} \\ \mathbf{b}_1^{(n-1)} \cdot \hat{\mathbf{x}} & \mathbf{b}_2^{(n-1)} \cdot \hat{\mathbf{x}} & \mathbf{b}_3^{(n-1)} \cdot \hat{\mathbf{x}} & \mathbf{b}_4^{(n-1)} \cdot \hat{\mathbf{x}} \end{bmatrix} \begin{bmatrix} E_{01}^{(n-1)} \\ E_{02}^{(n-1)} \\ E_{03}^{(n-1)} \\ E_{04}^{(n-1)} \end{bmatrix} \\
 = & \begin{bmatrix} \mathbf{e}_1^{(n)} \cdot \hat{\mathbf{x}} & \mathbf{e}_2^{(n)} \cdot \hat{\mathbf{x}} & \mathbf{e}_3^{(n)} \cdot \hat{\mathbf{x}} & \mathbf{e}_4^{(n)} \cdot \hat{\mathbf{x}} \\ \mathbf{b}_1^{(n)} \cdot \hat{\mathbf{y}} & \mathbf{b}_2^{(n)} \cdot \hat{\mathbf{y}} & \mathbf{b}_3^{(n)} \cdot \hat{\mathbf{y}} & \mathbf{b}_4^{(n)} \cdot \hat{\mathbf{y}} \\ \mathbf{e}_1^{(n)} \cdot \hat{\mathbf{y}} & \mathbf{e}_2^{(n)} \cdot \hat{\mathbf{y}} & \mathbf{e}_3^{(n)} \cdot \hat{\mathbf{y}} & \mathbf{e}_4^{(n)} \cdot \hat{\mathbf{y}} \\ \mathbf{b}_1^{(n)} \cdot \hat{\mathbf{x}} & \mathbf{b}_2^{(n)} \cdot \hat{\mathbf{x}} & \mathbf{b}_3^{(n)} \cdot \hat{\mathbf{x}} & \mathbf{b}_4^{(n)} \cdot \hat{\mathbf{x}} \end{bmatrix} \\
 \times & \begin{bmatrix} \exp\left(j\frac{\omega}{c}N_{z1}^{(n)}t^{(n)}\right) & 0 & 0 & 0 \\ 0 & \exp\left(j\frac{\omega}{c}N_{z2}^{(n)}t^{(n)}\right) & 0 & 0 \\ 0 & 0 & \exp\left(j\frac{\omega}{c}N_{z3}^{(n)}t^{(n)}\right) & 0 \\ 0 & 0 & 0 & \exp\left(j\frac{\omega}{c}N_{z4}^{(n)}t^{(n)}\right) \end{bmatrix} \\
 \times & \begin{bmatrix} E_{01}^{(n)} \\ E_{02}^{(n)} \\ E_{03}^{(n)} \\ E_{04}^{(n)} \end{bmatrix}. \tag{4.44}
 \end{aligned}$$

This can be consistently rewritten as

$$\mathbf{D}^{(n-1)} \mathbf{E}_0^{(n-1)} = \mathbf{D}^{(n)} \mathbf{P}^{(n)} \mathbf{E}_0^{(n)}. \tag{4.45}$$

For practical purposes it is better to write the latter equation as

$$\mathbf{E}_0^{(n-1)} = (\mathbf{D}^{(n-1)})^{-1} \mathbf{D}^{(n)} \mathbf{P}^{(n)} \mathbf{E}_0^{(n)}. \tag{4.46}$$

In Eqs. (4.45) and (4.46) the matrix $\mathbf{D}^{(n)}$ is called *dynamical matrix* and performs the transformation of waves at the interfaces. Rows of this matrix are obtained from the x and y components of the eigenmodes. Utilizing Eqs. (4.15) and (4.38) one can derive the expressions

$$D_{1j}^{(n)} = \mathbf{e}_j^{(n)} \cdot \hat{\mathbf{x}} = C_j^{(n)} [-\varepsilon_{xy}^{(n)}(\varepsilon_{zz}^{(n)} - N_y^2) + \varepsilon_{xz}^{(n)}(\varepsilon_{zy}^{(n)} + N_y^{(n)} N_{zj}^{(n)})], \tag{4.47}$$

$$D_{2j}^{(n)} = \mathbf{b}_j^{(n)} \cdot \hat{\mathbf{y}} = C_j^{(n)} N_{zj}^{(n)} [-\varepsilon_{xy}^{(n)}(\varepsilon_{zz}^{(n)} - N_y^2) + \varepsilon_{xz}^{(n)}(\varepsilon_{zy}^{(n)} + N_y^{(n)} N_{zj}^{(n)})], \tag{4.48}$$

$$D_{3j}^{(n)} = \mathbf{e}_j^{(n)} \cdot \hat{\mathbf{y}} = C_j^{(n)} [(\varepsilon_{zz}^{(n)} - N_y^2)(\varepsilon_{xx}^{(n)} - N_y^2 - N_{zj}^{(n)2}) - \varepsilon_{xz}^{(n)} \varepsilon_{zx}^{(n)}], \tag{4.49}$$

$$\begin{aligned}
 D_{4j}^{(n)} = \mathbf{b}_j^{(n)} \cdot \hat{\mathbf{x}} &= C_j^{(n)} [-(\varepsilon_{xx}^{(n)} - N_y^2 - N_{zj}^{(n)2})(N_y \varepsilon_{zy}^{(n)} + N_{zj}^{(n)} \varepsilon_{zz}^{(n)}) \\ &+ N_{zj}^{(n)} \varepsilon_{xz}^{(n)} \varepsilon_{zx}^{(n)} + N_y \varepsilon_{zx}^{(n)} \varepsilon_{xy}^{(n)}]. \tag{4.50}
 \end{aligned}$$

The second matrix in Eqs. (4.45) and (4.46) is called *propagation matrix* and describes the propagation of plane waves in the n -th layer. One can express this matrix using the Kronecker

4.4. ANISOTROPIC MULTILAYERS

symbol δ_{ij} as

$$P_{ij}^{(n)} = \delta_{ij} \exp\left(j \frac{\omega}{c} N_{zj}^{(n)} t^{(n)}\right). \quad (4.51)$$

Finally the vector $\mathbf{E}_0^{(n)}$ is a four-component vector of the complex eigen polarization amplitudes.

The equation (4.46) can be rewritten with help of so-called *transfer matrix* defined by Yeh [44] into the form

$$\mathbf{E}_0^{(n-1)} = (\mathbf{D}^{(n-1)})^{-1} \mathbf{D}^{(n)} \mathbf{P}^{(n)} \mathbf{E}_0^{(n)} = \mathbf{T}^{(n-1,n)} \mathbf{E}_0^{(n)}. \quad (4.52)$$

In the case of multilayered structure containing N layers, one can proceed recursively and relate the fields in the two isotropic half spaces subsequently

$$\begin{aligned} \mathbf{E}_0^{(0)}(z_0) &= (\mathbf{D}^{(0)})^{-1} \mathbf{D}^{(1)} \mathbf{P}^{(1)} (\mathbf{D}^{(1)})^{-1} \mathbf{D}^{(2)} \mathbf{P}^{(2)} \dots \\ &\dots (\mathbf{D}^{(N-1)})^{-1} \mathbf{D}^{(N)} \mathbf{P}^{(N)} (\mathbf{D}^{(N)})^{-1} \mathbf{D}^{(N+1)} \mathbf{E}_0^{(N+1)}(z_N) \\ &= \left[\prod_{n=1}^{N+1} \mathbf{T}^{n-1,n} \right] \mathbf{E}_0^{N+1}(z_N) = \mathbf{M} \mathbf{E}_0^{(N+1)}(z_N). \end{aligned} \quad (4.53)$$

Here, the matrix \mathbf{M} can describe the optical properties of any stratified anisotropic medium. To calculate this matrix, one has to solve the eigenvalue equations in each layer to derive the eigenmodes and dynamical and propagation matrices.

4.4.2 Eigenmodes in isotropic regions

Until now, we solved the wave equation in the anisotropic, homogenous medium magnetized along chosen direction. However, to calculate the optical response of multilayered structure described previously, we have to know the dynamical and propagation matrices of isotropic sandwiching half spaced as well. These spaces are described by scalar permittivities $(N^{(s)})^2$, where $s = 0$ or $N + 1$. In such case, the propagation wavevectors take two possible values

$$\gamma_{\pm}^{(s)} = \frac{\omega}{c} [N_y \hat{\mathbf{y}} \pm (N^{(s)2} - N_y^2)^{1/2} \hat{\mathbf{z}}]. \quad (4.54)$$

The substitution into the wave equation (4.8) shows that the eigenmodes are two pairs of orthogonal elliptically polarized waves [23, 45]. Therefore we can write the eigenmodes with $\gamma_+^{(s)}$

$$\mathbf{e}_1^{(s)} = \begin{bmatrix} p^{(s)} \\ q^{(s)} \cos \varphi^{(s)} \\ -q^{(s)} \sin \varphi^{(s)} \end{bmatrix}, \quad (4.55)$$

$$\mathbf{e}_3^{(s)} = \begin{bmatrix} -q^{(s)*} \\ p^{(s)*} \cos \varphi^{(s)} \\ -p^{(s)*} \sin \varphi^{(s)} \end{bmatrix}, \quad (4.56)$$

while the eigenmodes with $\gamma_-^{(s)}$

$$\mathbf{e}_2^{(s)} = \begin{bmatrix} p^{(s)} \\ q^{(s)} \cos \varphi^{(s)} \\ q^{(s)} \sin \varphi^{(s)} \end{bmatrix}, \quad (4.57)$$

$$\mathbf{e}_4^{(s)} = \begin{bmatrix} -q^{(s)*} \\ p^{(s)*} \cos \varphi^{(s)} \\ p^{(s)*} \sin \varphi^{(s)} \end{bmatrix}. \quad (4.58)$$

Here $\varphi^{(s)}$ denotes the angle of incidence ($N_y = N^{(s)} \sin \varphi^{(s)}$) and the complex numbers p and q satisfy the normalization condition

$$pp^* + qq^* = 1. \quad (4.59)$$

In nonabsorbing media, they takes the form [13]

$$p^{(s)} = \cos \theta^{(s)} \cos \epsilon^{(s)} - j \sin \theta^{(s)} \sin \epsilon^{(s)}, \quad (4.60)$$

$$q^{(s)} = \sin \theta^{(s)} \cos \epsilon^{(s)} + j \cos \theta^{(s)} \sin \epsilon^{(s)}. \quad (4.61)$$

Similarly, we can obtain the eigenmodes for magnetic fields propagating with $\gamma_+^{(s)}$

$$\mathbf{b}_1^{(s)} = N^{(s)} \begin{bmatrix} -q^{(s)} \\ p^{(s)} \cos \varphi^{(s)} \\ -p^{(s)} \sin \varphi^{(s)} \end{bmatrix}, \quad (4.62)$$

$$\mathbf{b}_3^{(s)} = N^{(s)} \begin{bmatrix} -p^{(s)*} \\ -q^{(s)*} \cos \varphi^{(s)} \\ q^{(s)*} \sin \varphi^{(s)} \end{bmatrix}, \quad (4.63)$$

and propagating with $\gamma_-^{(s)}$

$$\mathbf{e}_2^{(s)} = \begin{bmatrix} q^{(s)} \\ -p^{(s)} \cos \varphi^{(s)} \\ -p^{(s)} \sin \varphi^{(s)} \end{bmatrix}, \quad (4.64)$$

$$\mathbf{e}_4^{(s)} = \begin{bmatrix} p^{(s)*} \\ q^{(s)*} \cos \varphi^{(s)} \\ q^{(s)*} \sin \varphi^{(s)} \end{bmatrix}. \quad (4.65)$$

4.4. ANISOTROPIC MULTILAYERS

With the knowledge of all eigenmodes in isotropic medium, we can now construct the matrix $D^{(s)}$

$$D^{(s)} = \begin{bmatrix} p^{(s)} & p^{(s)} & -q^{(s)*} & -q^{(s)*} \\ N^{(s)}p^{(s)} \cos \varphi^{(s)} & -N^{(s)}p^{(s)} \cos \varphi^{(s)} & -N^{(s)}q^{(s)*} \cos \varphi^{(s)} & N^{(s)}q^{(s)*} \cos \varphi^{(s)} \\ q^{(s)} \cos \varphi^{(s)} & q^{(s)} \cos \varphi^{(s)} & p^{(s)*} \cos \varphi^{(s)} & p^{(s)*} \cos \varphi^{(s)} \\ -N^{(s)}q^{(s)} & N^{(s)}q^{(s)} & -N^{(s)}p^{(s)*} & N^{(s)}p^{(s)*} \end{bmatrix}, \quad (4.66)$$

and its inverse

$$(D^{(s)})^{-1} = (2N^{(s)} \cos \varphi^{(s)})^{-1} \begin{bmatrix} N^{(s)}p^{(s)*} \cos \varphi^{(s)} & p^{(s)*} & N^{(s)}q^{(s)*} & -q^{(s)*} \cos \varphi^{(s)} \\ N^{(s)}p^{(s)*} \cos \varphi^{(s)} & -p^{(s)*} & N^{(s)}q^{(s)*} & q^{(s)*} \cos \varphi^{(s)} \\ -N^{(s)}q^{(s)} \cos \varphi^{(s)} & -q^{(s)} & N^{(s)}p^{(s)} & -p^{(s)} \cos \varphi^{(s)} \\ -N^{(s)}q^{(s)*} \cos \varphi^{(s)} & q^{(s)} & N^{(s)}p^{(s)} & p^{(s)*} \cos \varphi^{(s)} \end{bmatrix}. \quad (4.67)$$

The propagation matrix in the isotropic medium has the form

$$P^{(s)} = \begin{bmatrix} e^{j\beta^{(s)}} & 0 & 0 & 0 \\ 0 & e^{-j\beta^{(s)}} & 0 & 0 \\ 0 & 0 & e^{j\beta^{(s)}} & 0 \\ 0 & 0 & 0 & e^{-j\beta^{(s)}} \end{bmatrix}, \quad (4.68)$$

where $\beta^{(s)} = \frac{\omega}{c} (N^{(s)2} - N_y^2)^{1/2} t^{(s)}$.

4.4.3 Reflection and transmission coefficients

Knowledge of the D and P matrices for each anisotropic layer in the multilayer structure as well as for the isotropic regions allows us to obtain the total matrix of the structure M

$$\begin{bmatrix} E_{01}^{(0)} \\ E_{02}^{(0)} \\ E_{03}^{(0)} \\ E_{04}^{(0)} \end{bmatrix} = \begin{bmatrix} M_{11} & M_{12} & M_{13} & M_{14} \\ M_{21} & M_{22} & M_{23} & M_{24} \\ M_{31} & M_{32} & M_{33} & M_{34} \\ M_{41} & M_{42} & M_{43} & M_{44} \end{bmatrix} \begin{bmatrix} E_{01}^{(N+1)} \\ E_{02}^{(N+1)} \\ E_{03}^{(N+1)} \\ E_{04}^{(N+1)} \end{bmatrix}. \quad (4.69)$$

In the front half space (0) the incident electromagnetic wave can be expressed as a mixture of two orthogonal polarization $e_1^{(0)}$ and $e_3^{(0)}$, not necessarily linear. Since there is no light coming from the back half space, we set the amplitudes of the waves propagating towards the structure from this half space equal to 0.

$$E_{02}^{N+1} = E_{04}^{N+1} = 0. \quad (4.70)$$

This simplifies the Eq. (4.69) into the form

$$\begin{bmatrix} E_{01}^{(0)} \\ E_{02}^{(0)} \\ E_{03}^{(0)} \\ E_{04}^{(0)} \end{bmatrix} = \begin{bmatrix} M_{11} & M_{12} & M_{13} & M_{14} \\ M_{21} & M_{22} & M_{23} & M_{24} \\ M_{31} & M_{32} & M_{33} & M_{34} \\ M_{41} & M_{42} & M_{43} & M_{44} \end{bmatrix} \begin{bmatrix} E_{01}^{(N+1)} \\ 0 \\ E_{03}^{(N+1)} \\ 0 \end{bmatrix}. \quad (4.71)$$

For orthogonally polarized incident, transmitted, and reflected modes in the sandwiching half spaces, we can define the global reflection coefficients as

$$r_{21}^{0,N+1} = \left(\frac{E_{02}^{(0)}}{E_{01}^{(0)}} \right)_{E_{03}^{(0)}=0} = \frac{M_{21}M_{33} - M_{23}M_{31}}{M_{11}M_{22} - M_{13}M_{31}}, \quad (4.72)$$

$$r_{41}^{0,N+1} = \left(\frac{E_{04}^{(0)}}{E_{01}^{(0)}} \right)_{E_{03}^{(0)}=0} = \frac{M_{41}M_{33} - M_{43}M_{31}}{M_{11}M_{22} - M_{13}M_{31}}, \quad (4.73)$$

$$r_{43}^{0,N+1} = \left(\frac{E_{04}^{(0)}}{E_{03}^{(0)}} \right)_{E_{01}^{(0)}=0} = \frac{M_{11}M_{43} - M_{41}M_{13}}{M_{11}M_{22} - M_{13}M_{31}}, \quad (4.74)$$

$$r_{23}^{0,N+1} = \left(\frac{E_{02}^{(0)}}{E_{03}^{(0)}} \right)_{E_{01}^{(0)}=0} = \frac{M_{11}M_{23} - M_{21}M_{13}}{M_{11}M_{22} - M_{13}M_{31}}. \quad (4.75)$$

The obtained coefficients can be arranged to form a (2 x 2) Jones matrix of reflection introduced by (2.29) in the representation of s and p incident waves

$$\mathbf{R}_{SP} = \begin{bmatrix} r_{ss} & r_{ps} \\ r_{sp} & r_{pp} \end{bmatrix} = \begin{bmatrix} r_{21}^{0,N+1} & r_{23}^{0,N+1} \\ r_{41}^{0,N+1} & r_{43}^{0,N+1} \end{bmatrix}. \quad (4.76)$$

To define the global transmission coefficients, we proceed the same way

$$t_{11}^{0,N+1} = \left(\frac{E_{01}^{(0)}}{E_{01}^{(0)}} \right)_{E_{03}^{(0)}=0} = \frac{M_{33}}{M_{11}M_{22} - M_{13}M_{31}}, \quad (4.77)$$

$$t_{31}^{0,N+1} = \left(\frac{E_{03}^{(0)}}{E_{01}^{(0)}} \right)_{E_{03}^{(0)}=0} = \frac{-M_{31}}{M_{11}M_{22} - M_{13}M_{31}}, \quad (4.78)$$

$$t_{33}^{0,N+1} = \left(\frac{E_{03}^{(0)}}{E_{03}^{(0)}} \right)_{E_{01}^{(0)}=0} = \frac{M_{11}}{M_{11}M_{22} - M_{13}M_{31}}, \quad (4.79)$$

$$t_{13}^{0,N+1} = \left(\frac{E_{01}^{(0)}}{E_{03}^{(0)}} \right)_{E_{01}^{(0)}=0} = \frac{-M_{13}}{M_{11}M_{22} - M_{13}M_{31}}. \quad (4.80)$$

Then the (2 x 2) Jones matrix of transmission (2.30) can be arranged as

$$\mathbf{T}_{SP} = \begin{bmatrix} t_{ss} & t_{ps} \\ t_{sp} & t_{pp} \end{bmatrix} = \begin{bmatrix} t_{11}^{0,N+1} & t_{13}^{0,N+1} \\ t_{31}^{0,N+1} & t_{33}^{0,N+1} \end{bmatrix}. \quad (4.81)$$

4.4. ANISOTROPIC MULTILAYERS

There is no restriction on the polarization of the involved waves.

The Jones matrices of reflection and transmission constructed here are connecting the model based on the Yeh's formalism and experimental configurations used for experimental studies in spectroscopic ellipsometry and magneto-optical spectroscopy. With the help of definitions of optical and magneto-optical angles, one can calculate them theoretically from the material parameters.

Moreover, as was shown by Yeh [44], the condition

$$M_{11}M_{33} - M_{13}M_{31} = 0 \quad (4.82)$$

presents the dispersion relation for the propagation of guided waves in the structure. In particular, the propagation in planar multilayer magneto-optic waveguides can be studied this way [46].

The Yeh's formalism extended to magnetic anisotropic absorbing media provides a unified general approach to the problem of electromagnetic interaction in multilayered planar structures. Besides the characterization of investigated materials, it can be also used as a powerful method to design special structures which enhance the magneto-optical response in the material [47]. Such structures are of interest for sensing weak magnetic fields in small volumes.

For the purpose of our studies, we wrote a computer calculation program based on the Yeh's formalism to calculate the magneto-optical response in polar and longitudinal geometries. In these special cases the permittivity tensor takes the form (3.8) and (3.14). Although the problem of a thin film on a thick substrate in polar and longitudinal geometries, which is the case of all samples presented in this work, can be solved analytically [15], it is favourable to construct a computer program based on Yeh's matrices, because it can be easily extended to more complex structures.

5 Experimental techniques

Methods of optical spectroscopy are widely used for the determination of physical properties of matter in many physical branches. In solid state physics, the information about the thickness, surface morphology as well as the information about the electronic structure of investigated material, chemical composition, etc. can be derived from the detection of the light change after its transmission or reflection on the sample. The main advantage of majority of optical techniques is a non-destructive approach.

To describe optical properties of matter and their spectral dependence is the main objective of spectroscopic ellipsometry. This technique, highly developed in 1990's, measures the change of incident light polarization upon its reflection or transmission. Typically, ellipsometry is done only in the reflection setup. The exact nature of polarization change is determined by the sample properties (thickness, complex refractive index or dielectric function tensor). Therefore, a spectral dependence of complex refractive index or dielectric function can be obtained from the fit of measured ellipsometric quantities.

To go further in optical investigation of magnetic materials, magneto-optical spectroscopy is useful and sensitive technique to use. Optical transitions, which are active only in applied magnetic field can be revealed by interpretation of experimental data. As was mentioned before, magneto-optical effects are only a small perturbation to the optical properties of magnetic materials. This requires high precision detection techniques.

In this chapter, we introduce basic principles of experimental setups of spectroscopic ellipsometry and magneto-optical spectroscopy which were used to obtain experimental data in this thesis.

5.1 Spectroscopic ellipsometry

There are several ellipsometric techniques nowadays used for the determination of material properties. Each of them has its own advantages and disadvantages for a particular purpose. Main ideas of ellipsometry including basic notions on polarization and experimental techniques are treated in the book written by Azzam and Bashara [13]. In this section we restrict ourselves to the description of a specific ellipsometer used in our experiments and corresponding data

5.1. SPECTROSCOPIC ELLIPSOMETRY

processing.

5.1.1 Basic experimental setup

To obtain the spectral dependence of the dielectric function of investigated materials, we used a for-zone null ellipsometer of the Research Institute of Electronics in Shizuoka University, Hamamatsu, Japan.

A standard optical sequence of the null ellipsometer consists of polarizer, sample, compensator and analyzer (PSCA), where the compensator is usually a phase-retarding tool. In order to follow the state of polarization of the light beam as it passes through the ellipsometer, we describe the light beam by its Jones vector and the optical elements by their Jones matrices. In following description we consider the optically isotropic and non-gyrotropic sample, the eigenpolarizations of which are the s and p polarizations. This leads to a diagonal Cartesian Jones matrix of reflection in the form

$$\mathbf{S} = \begin{bmatrix} r_s & 0 \\ 0 & r_p \end{bmatrix}. \quad (5.1)$$

The orthogonal polarizations s and p create the absolute coordinate system of all the optical components. Therefore all coordinate systems of the optical elements will be rotated to this coordinate system. The Jones vector of the light at the output of the analyzer can be written as

$$\mathbf{J}_O = \begin{bmatrix} 1 & 0 \\ 0 & 0 \end{bmatrix} \begin{bmatrix} \cos(\beta - \gamma) & \sin(\beta - \gamma) \\ -\sin(\beta - \gamma) & \cos(\beta - \gamma) \end{bmatrix} \begin{bmatrix} e^{j\frac{\delta}{2}} & 0 \\ 0 & e^{-j\frac{\delta}{2}} \end{bmatrix} \begin{bmatrix} r_s & 0 \\ 0 & r_p \end{bmatrix} \times \\ \begin{bmatrix} \cos(-\alpha) & \sin(-\alpha) \\ -\sin(-\alpha) & \cos(-\alpha) \end{bmatrix} \begin{bmatrix} 1 \\ 0 \end{bmatrix}, \quad (5.2)$$

where α , β , γ are the rotation angles of polarizer, compensator and analyzer. The intensity detected by the detector is given by the relation

$$I = I_0 \mathbf{J}_O \mathbf{J}_O^\dagger = I_0 |L|, \quad (5.3)$$

where I_0 denotes the intensity of the incident light beam. The latter equation defines the complex quantity L as

$$L = r_s \cos \alpha \left[e^{j\delta} \cos \gamma \cos(\beta - \gamma) - \sin \gamma \sin(\beta - \gamma) \right] \\ + r_p \sin \alpha \left[\cos \gamma \sin(\beta - \gamma) + e^{j\delta} \sin \gamma \cos(\beta - \gamma) \right]. \quad (5.4)$$

In the light of fore-zone null technique it is more convenient to rewrite this definition into the form [48]

$$L = r_s \sin \bar{\alpha} \left[e^{j\delta} \cos \gamma \sin(\bar{\beta} - \gamma) - \sin \gamma \sin(\bar{\beta} - \gamma) \right] \\ + r_p \sin \bar{\alpha} \left[\cos \gamma \sin(\bar{\beta} - \gamma) + e^{j\delta} \sin \gamma \cos(\bar{\beta} - \gamma) \right], \quad (5.5)$$

Zone	Ψ	Δ
1	$\bar{\alpha}$	$2\bar{\beta} + \frac{\pi}{2}$
2	$-\bar{\alpha}$	$2\bar{\beta} - \frac{\pi}{2}$
3	$\bar{\alpha}$	$-2\bar{\beta} - \frac{\pi}{2}$
4	$-\bar{\alpha}$	$-2\bar{\beta} + \frac{\pi}{2}$

Table 5.1: Four zones of the null intensity in an ellipsometer with PSCA configuration [48].

where

$$\bar{\alpha} = \alpha - \frac{\pi}{2}, \quad \text{and} \quad \bar{\beta} = \beta - \frac{\pi}{2}. \quad (5.6)$$

By searching the right values of α and β at a fixed γ the null ellipsometry provides a zero intensity of the light at the output. This gives the ellipsometric ratio ρ (see definition (2.31)). Under this fact, we can rewrite the Eq. (5.5) for the case of $L = 0$ into the form

$$\rho = -\tan \bar{\alpha} \frac{\tan \gamma + e^{j\delta} \tan(\bar{\beta} - \gamma)}{1 - e^{j\delta} \tan \gamma \tan(\bar{\beta} - \gamma)} \quad (5.7)$$

In our setup, the compensator was a quarter-wave retarder ($\delta = \frac{\pi}{2}$) operating at two opposite positions $\gamma^{(\pm)} = \pm \frac{\pi}{2}$. Taking this under the consideration along with the substitution $\rho = \tan \Psi e^{j\Delta}$ one can derive the following expressions for ellipsometric quantities

$$\tan \Psi e^{j\Delta} = -\tan \bar{\alpha} e^{2j(\bar{\beta} - \frac{\pi}{2})}, \quad (5.8)$$

$$\tan \Psi e^{j\Delta} = \tan \bar{\alpha} e^{-2j(\bar{\beta} + \frac{\pi}{2})}. \quad (5.9)$$

These two equations (the first for $\gamma^{(+)}$ and the second for $\gamma^{(-)}$) have generally four solutions. Thus we have four so-called null zones, as is written in Tab. 5.1. From each zone, we can derive requested Ψ and Δ quantities. Therefore to eliminate slight misalignments in the setup of polarizing components, the ellipsometric quantities are taken in all zones and finally their averages are calculated

$$\Psi = \frac{1}{4}(\bar{\alpha}_1 - \bar{\alpha}_2 + \bar{\alpha}_3 - \bar{\alpha}_4), \quad (5.10)$$

$$\Delta = \frac{1}{4}(\bar{\beta}_1 + \bar{\beta}_2 - \bar{\beta}_3 - \bar{\beta}_4), \quad (5.11)$$

where $\bar{\alpha}_i$ and $\bar{\beta}_i$ are the null positions of the polarizer and analyzer corresponding to the i -th zone. The experimental system (see the schematic picture in Fig. 5.1) was fully automated, where the positions of the polarizer, compensator and analyzer were set by high precision stepping motors and measured data were collected by the computer.

5.1. SPECTROSCOPIC ELLIPSOMETRY

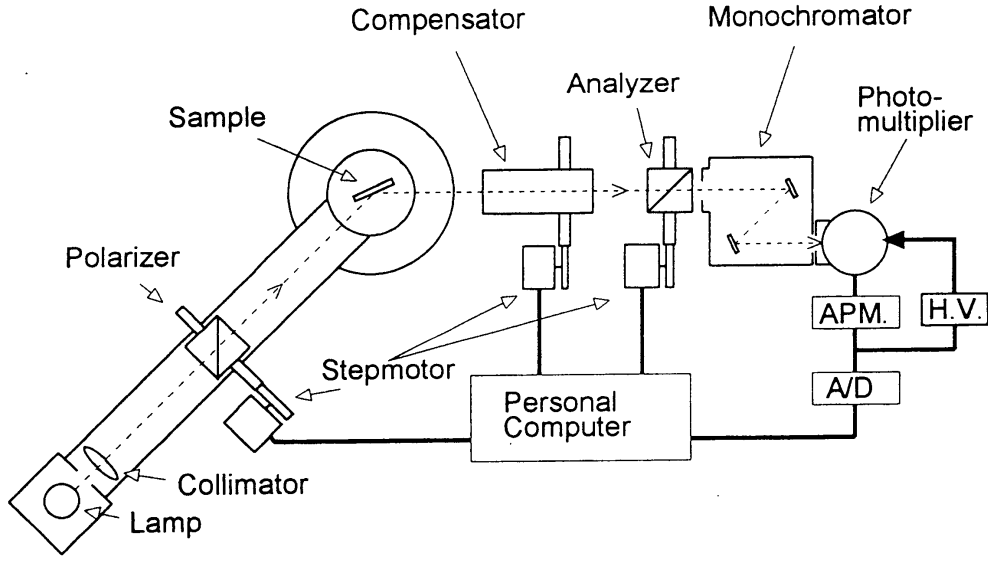


Figure 5.1: Experimental setup of four zone null ellipsometer which was used for ellipsometric experiments.

5.1.2 Experimental data processing

To derive diagonal elements of permittivity tensor, one has to fit the experimental angles Ψ and Δ . To minimize difference between experimental and calculated data, it is favourable to evaluate it as the angular distance between the measured and simulated points projected on Poiancaré's sphere using the expression

$$\cos D_j = \mathbf{S}_{exp,j} \cdot \mathbf{S}_{calc,j}, \quad (5.12)$$

where D_j denoted the error of j -the value, while

$$\mathbf{S}_{exp,j} = \begin{bmatrix} \sin 2\Psi_{exp,j} \cos \Delta_{exp,j} \\ \sin 2\Psi_{exp,j} \sin \Delta_{exp,j} \\ \cos 2\psi_{exp,j} \end{bmatrix}, \quad (5.13)$$

$$\mathbf{S}_{calc,j} = \begin{bmatrix} \sin 2\Psi_{calc,j} \cos \Delta_{calc,j} \\ \sin 2\Psi_{calc,j} \sin \Delta_{calc,j} \\ \cos 2\psi_{calc,j} \end{bmatrix} \quad (5.14)$$

are the three-dimensional normalized Stokes vectors [13] of j -th experimental and calculated ellipsometric angle, respectively. The Stokes vectors are here expressed with respect to an ideal nondepolarizing system. The value, which is minimized by the least-square method is a

summation of squares of partial errors, expressed as

$$D^2 = \sum_j D_j^2. \quad (5.15)$$

To parametrize the spectral dependence of permittivity, we used the model dielectric function (MDF). This allowed us to express the spectral dependence analytically. Therefore the spectral dependence of the permittivity is, generally, parametrized as a summation of various types of MDFs [48]. In this work, with respect to magnetic oxides, we used a summation of damped harmonic oscillators (DHO) and nondispersive term

$$\varepsilon_1(E) = \varepsilon_{1\infty} + \sum_{n=1}^N \frac{A_n E_n^2}{E_n^2 - E^2 + i\Gamma_n E_n E}, \quad (5.16)$$

where A , E_n and Γ_n denote an amplitude, resonant frequency and broadening of n -th oscillator. Using the Yeh's formalism simplified for isotropic medium we can calculate the reflection coefficients and subsequently theoretical values of Ψ and Δ . Thus the total error between theoretical and experimental values to be minimized has the form

$$D^2(p_1, p_2, \dots, d_1, d_2, \dots) = \sum_{j=1}^M D_j^2[\varepsilon_j(p_1, p_2, \dots), d_1, d_2, \dots], \quad (5.17)$$

where p_j are fitted parameters of MDFs, while d_j are fitted geometrical parameters.

5.2 Magneto-optical spectroscopy

There are two basic classes of experimental techniques which are employed for studies of weak magneto-optical effects. First class is measuring the direct change of the intensity of light at the output of optical element sequence. Second class, more sophisticated one, is based on the modulation of azimuth or ellipticity of incident light. In combination with synchronic detection system, modulation techniques increase the signal to noise ratio. However, both classes are used in different specific situations.

5.2.1 DC measurement techniques

Nearly crossed polarizers intensity detection is the simplest intensity technique employed in magneto-optical measurement devices. The optical element sequence consists of a light source, polarizer (oriented at an angle α with respect to the x axis), compensator or phase plate (angle 0° with respect to the x axis, phase shift δ), sample, analyzer (oriented at $\pi/2$ with respect to the x axis) and photodetector. Such sequence is schematically shown in Fig. 5.2. In practice, the

5.2. MAGNETO-OPTICAL SPECTROSCOPY

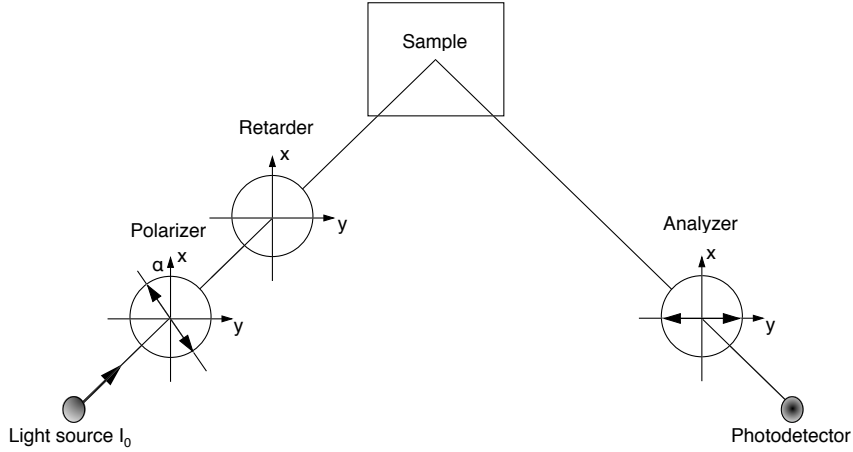


Figure 5.2: Optical sequence of the magneto-optical experimental setup with nearly crossed polarizers.

angle α is typically adjusted to several degrees. Although being very old, it is used nowadays in Kerr microscopes for observation of magnetic domains [49, 50] as well as in the simple sensor systems for weak magnetic field detection.

Another DC technique is using differential intensity detection, which enhances a signal to noise ratio. This method was the basis of magneto-optical data storage systems. Today is mainly used in the magneto-optical magnetometry to study magnetization processes. The schematic picture of the experimental setup is shown in Fig. 5.3. The optical element sequence consists of a polarizer (usually adjusted at s or p polarization), sample (described by Jones matrix of reflection), retarder (with phase shift $\delta = \pi$ rotated by angle α), Wollaston prism (separates incident light into two orthogonally polarized beams) and two photodetector systems connected to the computer.

The experiment is performed for the retarder angles $\alpha = \frac{(2n+1)\pi}{8}$, where n is the integer number. In this case, the measured differential intensity is [51]

$$\Delta I = I_1 - I_2 = I_0 |r_{ss}|^2 \theta_{Ks}. \quad (5.18)$$

Therefore measured differential intensity is proportional to the Kerr rotation. In Eq. (5.18) I_0 is the incident light intensity and $|r_{ss}|^2$ is the reflectivity of the sample. For further reading about DC measurements techniques see Refs. [24, 51]

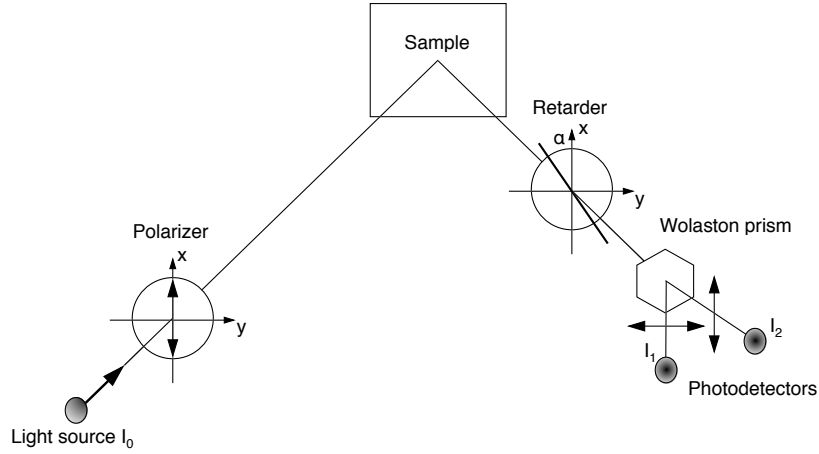


Figure 5.3: Optical sequence typically used in the differential intensity detection technique.

5.2.2 Modulation techniques

Owing to the simplicity of DC intensity detection techniques, they suffer from the sensitivity to the noise of detectors, vibrations of optical elements or temperature changes in the laboratory. This negatively affects the signal quality and the precision of the measurement. Contrary to DC detection, modulation techniques reduce the noise and increase the accuracy of polarizer and analyzer crossing. There are two basic techniques, using the time modulation of the light polarization. First, intensity method, is based on the modulation of ellipticity of light wave using the photoelastic modulator (described in detail in [24]). This method allows a fast measurement, which makes it suitable for the study of the dynamics of magnetization processes. Because it is an intensity method, the calibration of the equipment is required in each measurement. This makes it inconvenient for spectroscopical experiments. Therefore we will not discuss this technique here. Here we apply the second technique based on the azimuth modulation.

The azimuth of polarization ellipse can be modulated in time utilizing the Faraday rotation in glass. Such modulator, called the Faraday cell, consists of a fused quartz rod with optically polished faces, inserted into a solenoid coil (see Fig. 5.4). Owing to the sinusoidal time dependence of the modulation current in the coil, generated by a high power audio amplifier, the azimuth of the light wave passing through the cell is harmonically modulated in time. One can imagine the Faraday cell as a rotator with time dependent angle of rotation. Jones matrix of the Faraday modulation cell can be written as

$$\mathbf{M} = \begin{bmatrix} \cos(\beta_0 \sin \omega t) & -\sin(\beta_0 \sin \omega t) \\ \sin(\beta_0 \sin \omega t) & \cos(\beta_0 \sin \omega t) \end{bmatrix}, \quad (5.19)$$

where β_0 is the amplitude of modulation and ω is modulation frequency. In real measurements the amplitude β_0 is smaller than 3° . In combination with synchronic detection provided by

5.2. MAGNETO-OPTICAL SPECTROSCOPY

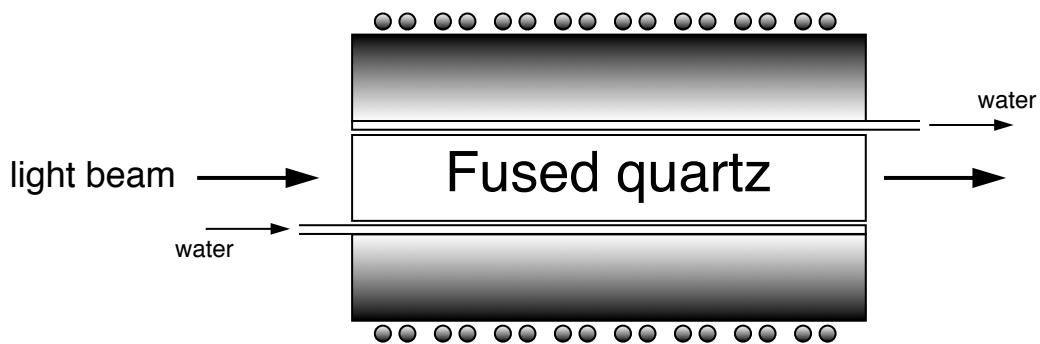


Figure 5.4: Schematic cross-section of the Faraday cell after [24].

lock-in amplifier, one can detect the ω -component carrying the useful information.

5.2.3 Magneto-optical spectrometer based on the azimuth modulation technique

The magneto-optical spectrometer which was used to obtain the experimental data for this thesis is based on the azimuth modulation technique in combination with the azimuth compensation controlled by a negative feedback. This feedback controls the intensity of light at the output of the analyzer. The experimental setup for the measurement of Kerr rotation was developed by Kahn and later extended for the extraction of Kerr ellipticity. The optical element sequence consists of [24]

- Polarizer (oriented at α)
- Faraday modulation cell, described in previous subsection
- Faraday null cell, where the change η of the azimuth is proportional to the current which is controlled electronically by a feedback circuit
- Phase plates (oriented at 0 with phase shift δ)
- Sample mounted in electromagnet
- Analyzer (oriented at ξ)
- Detector

The diagram of the setup is displayed in Fig. 5.6. To describe the function of the spectrometer in detail, we will follow the work of Nývlt [24]. Using the Jones matrix formalism, we can describe the polarization state of the light at the output of the analyzer as a product

$$\mathbf{J}_O = \begin{bmatrix} \cos^2 \xi & \sin \xi \cos \xi \\ \sin \xi \cos \xi & \sin^2 \xi \end{bmatrix} \begin{bmatrix} r_{ss} & r_{ps} \\ r_{sp} & r_{pp} \end{bmatrix} \begin{bmatrix} e^{j\frac{\delta}{2}} & 0 \\ 0 & e^{-j\frac{\delta}{2}} \end{bmatrix} \times \\ \times \begin{bmatrix} \cos(\beta_0 \sin \omega_m t) & -\sin(\beta_0 \sin \omega_m t) \\ \sin(\beta_0 \sin \omega_m t) & \cos(\beta_0 \sin \omega_m t) \end{bmatrix} \begin{bmatrix} \cos \eta & -\sin \eta \\ \sin \eta & \cos \eta \end{bmatrix} \begin{bmatrix} \sin \alpha \\ \cos \alpha \end{bmatrix}. \quad (5.20)$$

We measure the Kerr effect only for two special cases of the incident light polarization (s and p polarized light). Accordingly, the analyzer is set to transmit either the s polarized ($\xi = 0$) or p polarized ($\xi = \frac{\pi}{2}$) waves. Taking this into account, the Jones vector of the polarized light at the output has the form

$$\mathbf{J}_O = \begin{bmatrix} \cos^2 \xi (r_{ss} e^{j\frac{\delta}{2}} \cos \Omega + r_{ps} e^{-j\frac{\delta}{2}} \sin \Omega) \\ \sin^2 \xi (r_{sp} e^{j\frac{\delta}{2}} \cos \Omega + r_{pp} e^{-j\frac{\delta}{2}} \sin \Omega) \end{bmatrix}, \quad (5.21)$$

where

$$\Omega = \alpha + \eta + \beta_0 \sin \omega_m t. \quad (5.22)$$

Let us now consider the case of the p transmission of analyzer ($\xi = \frac{\pi}{2}$). For small values of magneto-optical effects $|\eta| \ll 1$, modulation amplitude $|\beta_0| \ll 1$, and polarizer angle $|\alpha| \ll 1$, the intensity on the detector can be approximated

$$I \approx \frac{1}{2} [|r_{sp}|^2 + |r_{pp}|^2 \Omega^2 + (r_{sp} r_{pp}^* e^{j\delta} + r_{sp}^* r_{pp} e^{-j\delta}) \Omega]. \quad (5.23)$$

The intensity component which is time dependent

$$I_{\omega_m} \approx |r_{pp}|^2 \left[\alpha + \eta + \Re \left(\frac{r_{sp}}{r_{pp}} e^{j\delta} \right) \right] \beta_0 \sin \omega_m t \quad (5.24)$$

is a linear function of α , η and $\Re \left(\frac{r_{sp}}{r_{pp}} e^{j\delta} \right)$.

The Faraday null cell is controlled by a negative feedback circuit. To understand the function of this feedback, one can take a look at the Fig. 5.5. For better mathematical description and explanation, we introduce the angle $\Gamma(\delta)$, which is representing the magneto-optical response of the sample in the intensity I_{ω_m} at ω_m . For a given δ

$$\Gamma(\delta) = -\Re \left(\frac{r_{sp}}{r_{pp}} e^{j\delta} \right). \quad (5.25)$$

The total amplification of the apparatus without the feedback can be written as

$$A_S = \frac{\partial U_{out}}{\partial (\alpha + \eta - \Gamma(\delta))} \quad [V \cdot deg^{-1}], \quad (5.26)$$

5.2. MAGNETO-OPTICAL SPECTROSCOPY

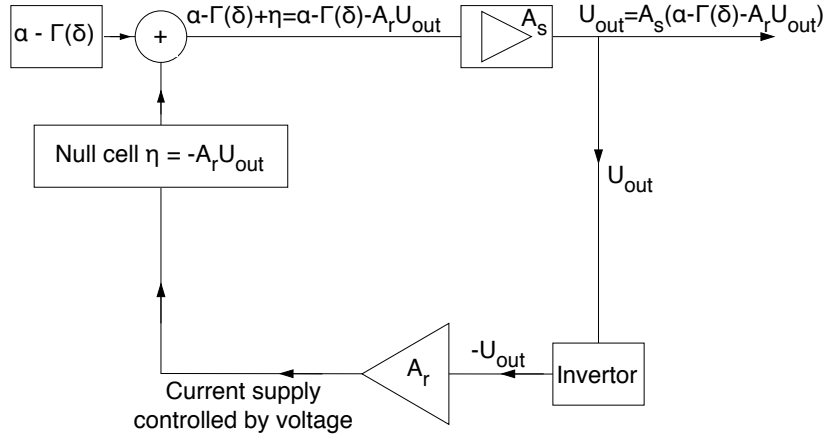


Figure 5.5: Functioning of the negative feedback loop.

while the total amplification of the feedback regulation part is given by

$$A_R = \frac{\partial \eta}{\partial U_{out}} \quad [deg \cdot V^{-1}], \quad (5.27)$$

and the total feedback loop amplification is given by their product as

$$g = A_R A_S. \quad (5.28)$$

With the help of the Fig. 5.5 we can obtain the equation for the rotation angle of the Faraday null cell in the form

$$\eta = -\frac{A_R A_S}{1 + A_R A_S} (\alpha - \Gamma(\delta)) = -\frac{g}{1 + g} (\alpha - \Gamma(\delta)). \quad (5.29)$$

It is possible to set up the measurement system to obtain high value of total amplification $|g| \gg 1$. In this case, the last equation has the approximative solution

$$\eta + \alpha - \Gamma(\delta) \approx 0. \quad (5.30)$$

Equation (5.30) in combination with Eq. (5.24) describes the real nature of the function of the Faraday null cell. This cell automatically turns the plane of polarization by a certain angle to adjust $I_{\omega_m} \approx 0$ and therefore compensates all changes produced by magneto-optical effects in the sample or by rotation of the polarizer. Measured signal on the output is then proportional to the magneto-optical effect of the sample and it decreases with increasing amplification of the feedback regulator. It is necessary to note that $\alpha - \Gamma(\delta)$ can not be completely compensated by η , because at least a small signal has to be present to control the feedback. With regard to the definition of $\Gamma(\delta)$, we can rewrite the Eq. 5.30 in the form

$$\alpha + \eta \approx \Gamma(\delta) = -\Re \left(\frac{r_{sp}}{r_{pp}} e^{j\delta} \right). \quad (5.31)$$

The latter equation holds generally for any experimental geometry with arbitrary orientation of magnetization vector. However, in this work we present the experimental results measured in polar and longitudinal geometries only. Therefore we focus ourselves to these two special cases and relate the angle $\Gamma(\delta)$ to magneto-optical quantities which are the objectives of our research. It can be done with help of the definition (2.40) and leads to

$$\Gamma(\delta) = -\Re\left(-\frac{r_{ps}}{r_{pp}}e^{j\delta}\right) = -\theta_{K_p} \cos \delta + \epsilon_{K_p} \sin \delta \quad (5.32)$$

for polar geometry and

$$\Gamma(\delta) = -\Re\left(\frac{r_{ps}}{r_{pp}}e^{j\delta}\right) = \theta_{K_p} \cos \delta - \epsilon_{K_p} \sin \delta \quad (5.33)$$

for longitudinal geometry.

To derive the equations for s polarized transmission of the analyzer, one can proceed in similar way as for p polarization. Because this time $\eta = 0$ the polarizer should be adjusted to nearly 90 degree

$$\alpha = \frac{\pi}{2} + \zeta. \quad (5.34)$$

This leads to output intensity

$$I_{\omega_m} \approx \left[\zeta + \eta - \Re\left(\frac{r_{ps}}{r_{ss}}e^{-j\delta}\right) \right] \beta_0 \sin \omega_m t. \quad (5.35)$$

When the negative feedback is turned on, the measured signal becomes

$$\zeta + \eta \approx \Gamma'(\delta) = \Re\left(\frac{r_{ps}}{r_{ss}}e^{-j\delta}\right). \quad (5.36)$$

To express $\Gamma'(\delta)$ using magneto-optical quantities, we take into account the definition (2.37). Then for polar configuration

$$\Gamma'(\delta) = \Re\left(-\frac{r_{sp}}{r_{ss}}e^{-j\delta}\right) = -\theta_{K_s} \cos \delta - \epsilon_{K_s} \sin \delta \quad (5.37)$$

and for longitudinal configuration

$$\Gamma'(\delta) = \Re\left(\frac{r_{sp}}{r_{ss}}e^{-j\delta}\right) = \theta_{K_s} \cos \delta + \epsilon_{K_s} \sin \delta. \quad (5.38)$$

Equations (5.32), (5.33), (5.37), (5.38) have similar form except the signs. It means that measured signal is generally a mixture of the Kerr rotation θ_K and the Kerr ellipticity ϵ_K . The ratio of these two quantities depends on the phase shift δ introduced by the phase retarder. The pure Kerr rotation is obtained when $\delta = 0$, while pure Kerr ellipticity is obtained for $\delta = \frac{\pi}{2}$.

For all measurements and geometries we used a fixed phase plate to achieve a good signal stability. Therefore to obtain the complex Kerr effect spectra, we performed two independent

5.2. MAGNETO-OPTICAL SPECTROSCOPY

measurements. First we measured the spectrum without presence of phase plate and obtained a pure Kerr rotation. Afterwards, we put a phase plate ($0 < \delta < \frac{\pi}{2}$) and measured the signal. Along with the knowledge of pure Kerr rotation, we can calculate Kerr ellipticity using a simple formula.

In the real measurement, the signal is recorded for two opposite orientations of magnetic field and the resulting magneto-optical quantities are calculated from a half of this difference

$$\Gamma(\delta) = \frac{\Delta(\alpha + \eta)}{2}. \quad (5.39)$$

The main advantages of the compensation technique with azimuth modulation are

- Azimuth modulation with synchronic detection notably increase the signal to noise ratio.
- Intensity dependence at the output is a linear function of a deviation from crossed polarizers.
- Crossing of polarizers is, owing to the null cell controlled by a negative feedback, completely automatic without mechanical input and at high amplifications g is very precise.
- Value of the measured angle at high g is not dependent on the intensity of output light (null method).

Now we take a detailed look on the experimental setup shown in Fig. 5.6. As a light source, a high pressure 450W Xe lamp (Osram XBO 450W/1) was employed. Afterwards, the light was monochromatized by a prism monochromator SPM-2 Carl Zeiss Jena. All optical elements, including lenses and glass rods for modulation and null cell, were made from suprasil quartz glass with extended transmission to UV. The temperature of the Faraday cells was kept constant using a closed water circuit with a thermostat. The signal modulation frequency was approximately 2 kHz. A pair of calcite polarizers served as a polarizer and analyzer. To detect the signal in the blue region and near UV, a photomultiplier tube EMI with S20 cathode, mounted in quartz envelope, was employed. On the other hand, in the infrared region this photomultiplier was replaced by Hamamatsu R3310-02 with InGaAs photocathode. The synchronic detection was provided by a lock-in amplifier Stanford Research System, model SR830DSP. The negative feedback is introduced by means of analog output signal from the lock-in detector. This signal is used to control the current supply for the null cell. Owing to very high stability of this supply, the resolution of the spectrometer is in the order of 10^{-4} deg. Measured sample is mounted in electromagnet with variable magnetic circuit to measure the Kerr effect in polar, longitudinal or transverse geometry. Usual values of the magnetic field during the measurements were 470 mT at 2 A for polar configuration and 100 mT at 2 A for longitudinal configuration. The magnetic

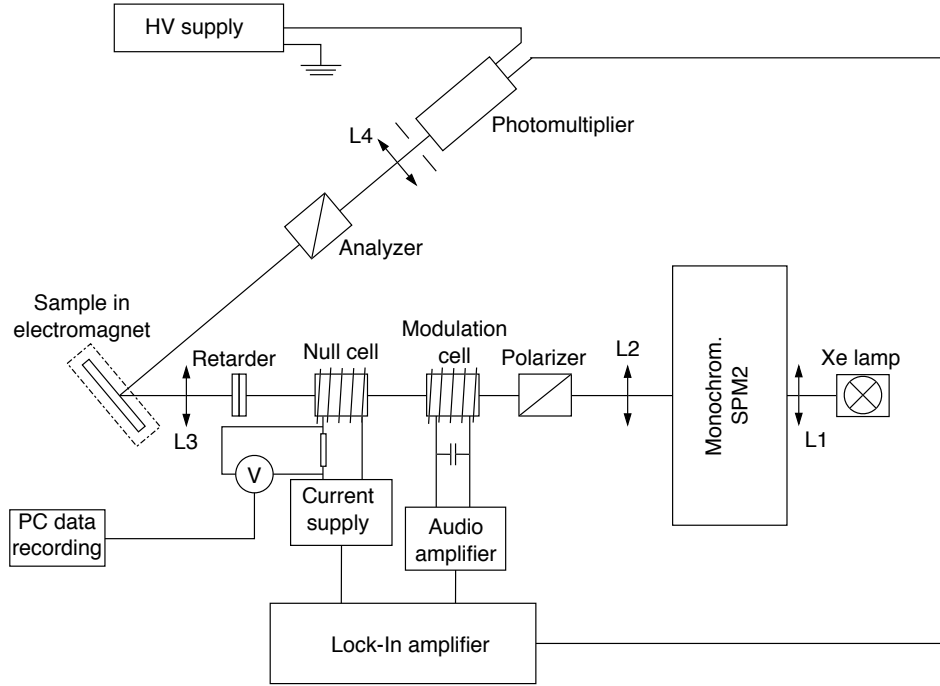


Figure 5.6: Experimental setup for magneto-optical measurements in the photon energy range from 1.2 to 5 eV.

field in the electromagnet as well as the wavelength of the incident light is controlled by the a computer. The computer also collects current values on the null cell measured by Keithley multimeter connected by GPIB interface. The computer program for spectrometer control has been written by Dr. M. Nývlt.

5.2.4 Calibration procedure and experimental data processing

Although the data are automatically stored by the computer, it is necessary after the measurement to calculate a Kerr angle from the current applied to the Faraday null cell. To proceed the calculation, one has to know the calibration constant of the spectrometer. For this purpose a calibration procedure in modified configuration of optical elements is performed. The optical sequence in this case consists of the polarizer (oriented at α), phase plates (with a phase shift δ), modulation and null Faraday cells and the analyzer (oriented at $\frac{\pi}{2}$). Owing to the basic property of the null cell to rotate the light polarization to be perpendicular to the transmission axis of the analyzer we can write the equation

$$\tan 2\eta = -\tan 2\alpha \cos \delta. \quad (5.40)$$

5.2. MAGNETO-OPTICAL SPECTROSCOPY

In the case without phase plates ($\delta = 0$), it is evident that the null cell can be calibrated by a rotation of polarizer about a well defined angle. The angle of rotation of Faraday null cell is therefore given by

$$\eta(\lambda) = C_N I_N \quad (5.41)$$

and is proportional to the current I_N . From the latter equation it is easy to obtain the relation

$$C_N = \frac{\Delta\eta}{\Delta I_N} = \frac{-\Delta\alpha}{\Delta I_N}. \quad (5.42)$$

In this work, the calibration constant was parametrized by the expression

$$C_N(E) = 0.0002E^3 + 0.0001E^2 + 0.0013E - 0.0007, \quad (5.43)$$

where E denotes the energy.

The calibration of phase plates is obtained from the second measurement. For each wavelength we determine the calibration constant

$$D_N = -\frac{\Delta\alpha}{\Delta I_N}. \quad (5.44)$$

For small angles the Eq. (5.40) can be linearized

$$\eta \approx -\alpha \cos \delta, \quad (5.45)$$

and the angles η and α can be replaced by $\Delta\eta$ and $\Delta\alpha$. Then

$$\cos \delta \approx \frac{C_N}{D_N}. \quad (5.46)$$

This calibration is good at $\delta \sim \frac{\pi}{2}$. For smaller angles the accuracy is decreasing.

6 Experimental results on $\text{La}_{2/3}\text{Sr}_{1/3}\text{MnO}_3$ thin films

6.1 Material Introduction

The hole doped manganese oxides $\text{La}_{1-x}\text{M}_x\text{MnO}_3$ ($\text{M} = \text{Ca}, \text{Sr}, \text{Ba}$) with perovskite - type structure are promising materials for the fabrication of novel magnetic devices due to their colossal magnetoresistance (CMR) effect [8, 10, 52, 53] and high degree of spin polarization. These materials exhibit a mixed-valence behavior of $\text{Mn}^{3+}/\text{Mn}^{4+}$ ions owing to the substitution by divalent atoms (Ca, Sr, Ba). This leads to metallic conductivity and, simultaneously, to ferromagnetic ordering, which was explained by a double-exchange interaction, where Mn ions can exchange their valency by a simultaneous jump of the e_g electron of Mn^{3+} on the O p -orbital and from the O p -orbital to the empty e_g orbital of Mn^{4+} [54, 55, 56]. According to the experiments performed on polycrystalline samples, ferromagnetic metallic behavior occurs in a certain range of divalent atom concentrations centered around $x \sim 1/3$. Recent extensive studies showed that also other interactions, such as antiferromagnetic (AF) superexchange [57], Jahn-Teller (JT) [58] or charge - orbital ordering [59] interactions may affect an overall electrical and magnetic properties of manganese oxides. These interactions are strongly coupled with the lattice through the orbital degrees of freedom of the e_g electrons on Mn^{3+} ions in the MnO_6 octahedron surrounded by oxygen atoms. Electronic configuration of Mn^{3+} ions is $t_{2g}^3 e_g^1$ with spin quantum number $S = 2$. Because nearly degenerate e_g orbitals have lobes directed to the oxygen ligands, the $3d - 2p$ electron hybridization together with its anisotropy strongly depends on the Mn - O bond length. Hence, physical properties of manganese oxides deposited on commonly used substrates as LaAlO_3 (LAO) and SrTiO_3 (STO) are different due to their different lattice constants and are very sensitive to the induced strain [58, 60, 61]. Different magnetic properties were also observed for $\text{La}_{2/3}\text{Sr}_{1/3}\text{MnO}_3$ (LSMO) thin films deposited on STO substrates with different crystallographic orientations [62]. The knowledge of spin-dependent electronic structure of LSMO along with the information about its dependence on induced strain and structural properties is therefore a necessary for the application of these materials to magnetic devices.

Motivated by device applications in sensors and spintronics, special attention is paid to high

6.1. MATERIAL INTRODUCTION

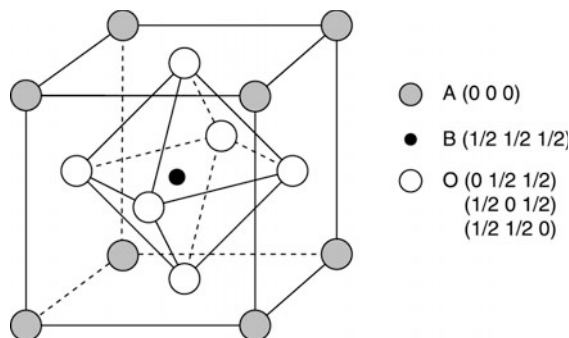


Figure 6.1: Schematic picture of the cubic perovskite structure [79].

quality $\text{La}_{1-x}\text{M}_x\text{MnO}_3$ films with $x \sim 0.3$. These can be grown by pulsed laser deposition (PLD), e.g., onto SrTiO_3 (STO) single-crystal substrates. The bulk crystals of this composition are distinguished by optimal CMR and the highest Curie temperature, $T_C = 380$ K. In films, T_C is reduced due to the sensitivity of the double exchange to the strain induced by the substrate-film lattice constant mismatch. In the last decade, optical reflectance measurements were used as a nondestructive method to obtain the information about optical properties and electronic structure of manganese oxides [63, 64, 65, 66]. Magneto-optical properties were studied in the polar [67, 68, 69, 70, 71, 72, 73, 74] and transverse [75, 76] geometries on various types of samples. Theoretical studies were also reported [77]. Recently, with a rapid development of suitable deposition techniques, ultra-thin manganese oxide films were obtained [78]. This brought up the question about physical properties of such thin films, since all previous studies were performed on bulk crystals or single-crystal layers with thicknesses exceeding 100 nm. To our knowledge, there is no report on the magneto-optical spectroscopy of LSMO thin films with the thickness below 50 nm (except our studies), although the knowledge of physical properties of such thin layers is fundamental for the application to novel devices. Besides, due to the small thickness of investigated samples, which is below the penetration depth of incident light, measured spectra give also the information about the interface between deposited film and substrate.

The crystallographic structure of a general $R_{1-x}M_x\text{MnO}_3$ material is nearly cubic perovskite as shown in Fig. 6.1. The large sized R trivalent ions and M divalent ions occupy the A-site with 12-fold oxygen coordination. In the center of the cube, smaller Mn ions in the mixed valence state $\text{Mn}^{3+} - \text{Mn}^{4+}$ are situated, surrounded by an oxygen octahedron with 6-fold coordination. However, in practice the crystalline structure differs from cubic and manganites have, at least at low temperature, a lower symmetry rhombohedral or orthorhombic structure. This is the case of LaMnO_3 compound with orthorhombic structure, which is widely used as a

parent compound for the synthesis of manganese oxides for various device applications. More information about structural and magnetic properties as well as electronic structure can be found elsewhere [79, 80].

In this chapter, we present systematic study of optical and magneto-optical properties of LSMO thin films grown on STO substrates of (100) and (110) crystallographic orientations. We carefully compare our results with previous studies on bulk material and thick films, and propose an assignment of the electron transitions observed in optical and magneto-optical spectra to provide a more complete description of optical and magneto-optical transitions in LSMO thin films with low thicknesses.

6.2 Sample deposition

Investigated samples were prepared in collaboration with Institut d'Electronique Fondamentale, Université Paris Sud, Orsay, France and Laboratoire de Cristallographie et Sciences des Matériaux, CNRS, Caen, France. LSMO thin films were deposited by pulsed laser deposition (PLD) technique (Lambda Physik KrF, $\lambda = 248$ nm, repetition rate 1 Hz, fluence close to 170 mJ/cm^2) [81] onto STO ($a = 0.3905$ nm, cubic) substrates with crystallographic orientations (100) and (110). The target-to-substrate distance D was fixed to 5 cm. Depositions were achieved under a dynamic vacuum with an oxygen pressure P 100 mTorr (which satisfied the condition for smooth surface and large grain growth, resulting from the PD^3 law [82]) at a deposition temperature 630°C . To assure a full oxygen stoichiometry, films were cooled after the deposition to

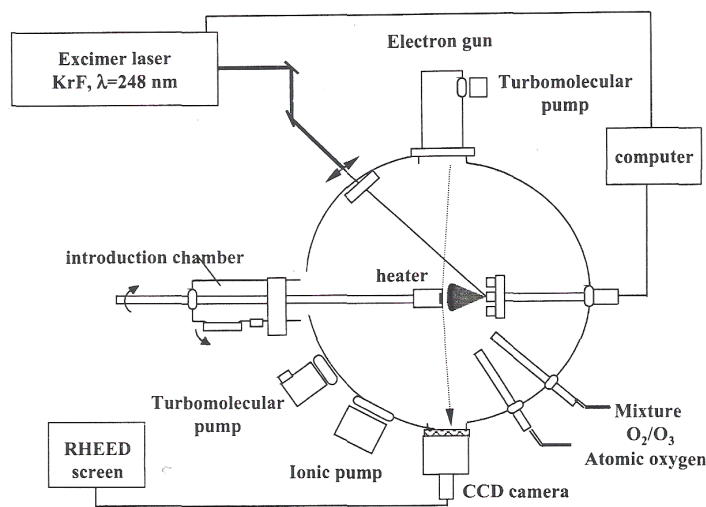


Figure 6.2: Pulsed laser deposition equipment used for the growth of LSMO thin films.

6.2. SAMPLE DEPOSITION

Sample	t_{nom} [nm]	t_{el} [nm]
(100) STO substrate		
ng523	10	11.9
ng524	20	22.8
ng517	30	35.2
ng487	40	-
(110) STO substrate		
ing614	10	10.8
ing615	19	14.5
ing616	31	31.2
ing613	51	48

Table 6.1: Thicknesses of LSMO thin films deposited on (100) and (110) STO substrates. In this table t_{nom} denotes the nominal thickness and t_{el} denotes the thickness calculated from the results of spectroscopic ellipsometry.

room temperature (RT) under an oxygen pressure 0.5 atm. for 30 minutes. The use of STO substrate imposed an in-plane tensile strain due to the lattice mismatch of 0.41%. Investigated films with nominal thicknesses of 10, 20, 30 and 40 nm were deposited on (100) STO substrates and films with nominal thicknesses 10, 18, 30 and 50 nm were deposited on (110) STO substrates. Thicknesses of all samples are summarized in Tab. 6.1

A schematic picture of the deposition equipment is displayed in Fig. 6.2. The light beam generated by a high power pulsed laser is impacting the ceramic target of chosen material and rip out its atoms. In presence of a specific gas pressure (usually oxygen), a plasma of the target material is produced and condensates on the heated substrate. To increase the homogeneity of the film the heated substrate usually rotates. Typical lasers used for the LSMO deposition are UV excimer lasers KrF with $\lambda = 248$ nm (our case), XeCl with $\lambda = 308$ nm [83] and ArF with $\lambda = 193$ nm [84]. For in-situ monitoring of the growth, Reflection High Energy Electron Diffraction (RHEED) is used. PLD technique is widely used to grow LSMO thin films. Its merit consists in the conservation of the target stoichiometry. High quality thin films with the roughness of the order of one elementary cell can be grown by this technique.

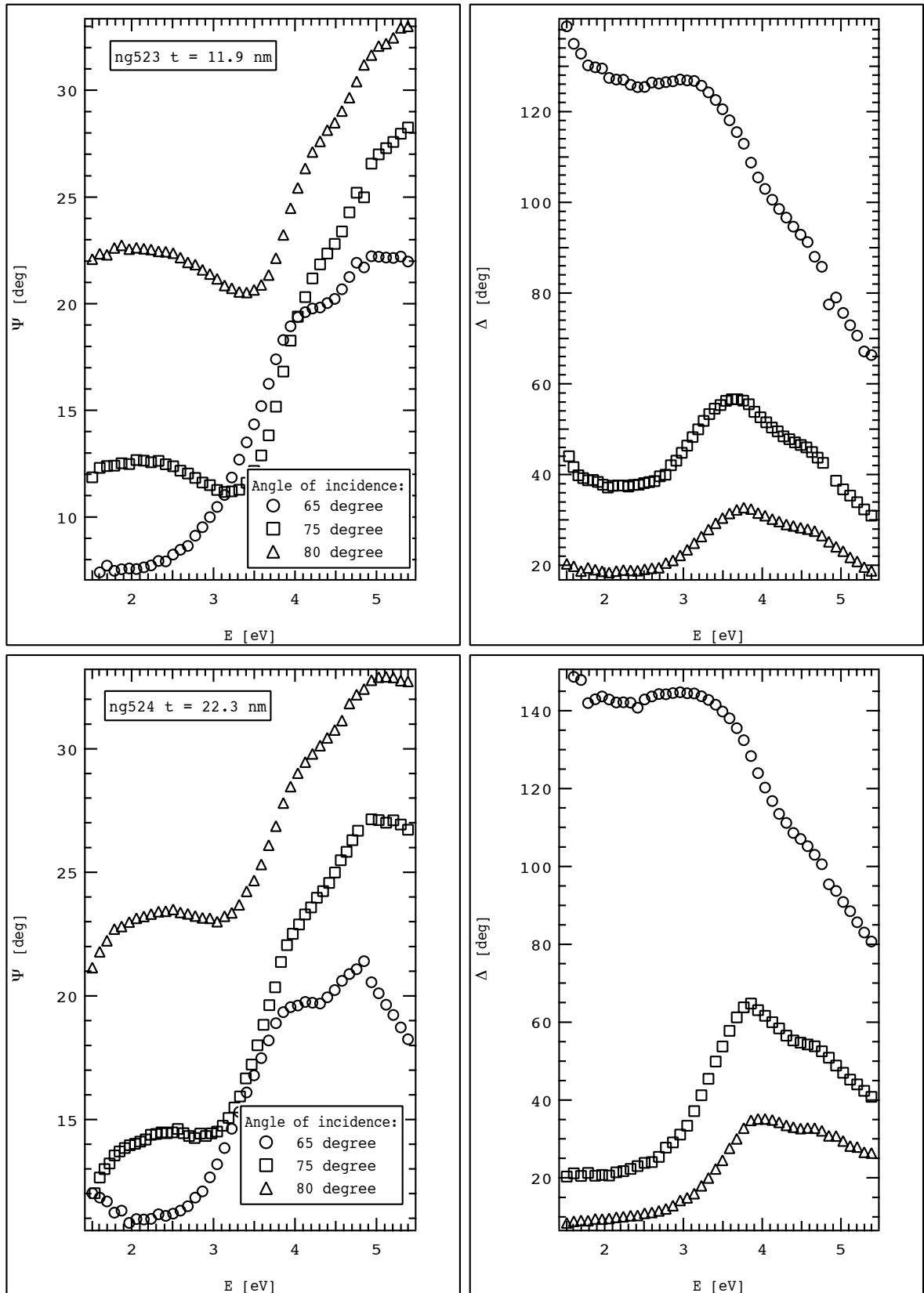


Figure 6.3: Experimental ellipsometric data of thin LSMO films deposited onto (100) STO substrates, measured at indicated angles of incidence.

6.2. SAMPLE DEPOSITION

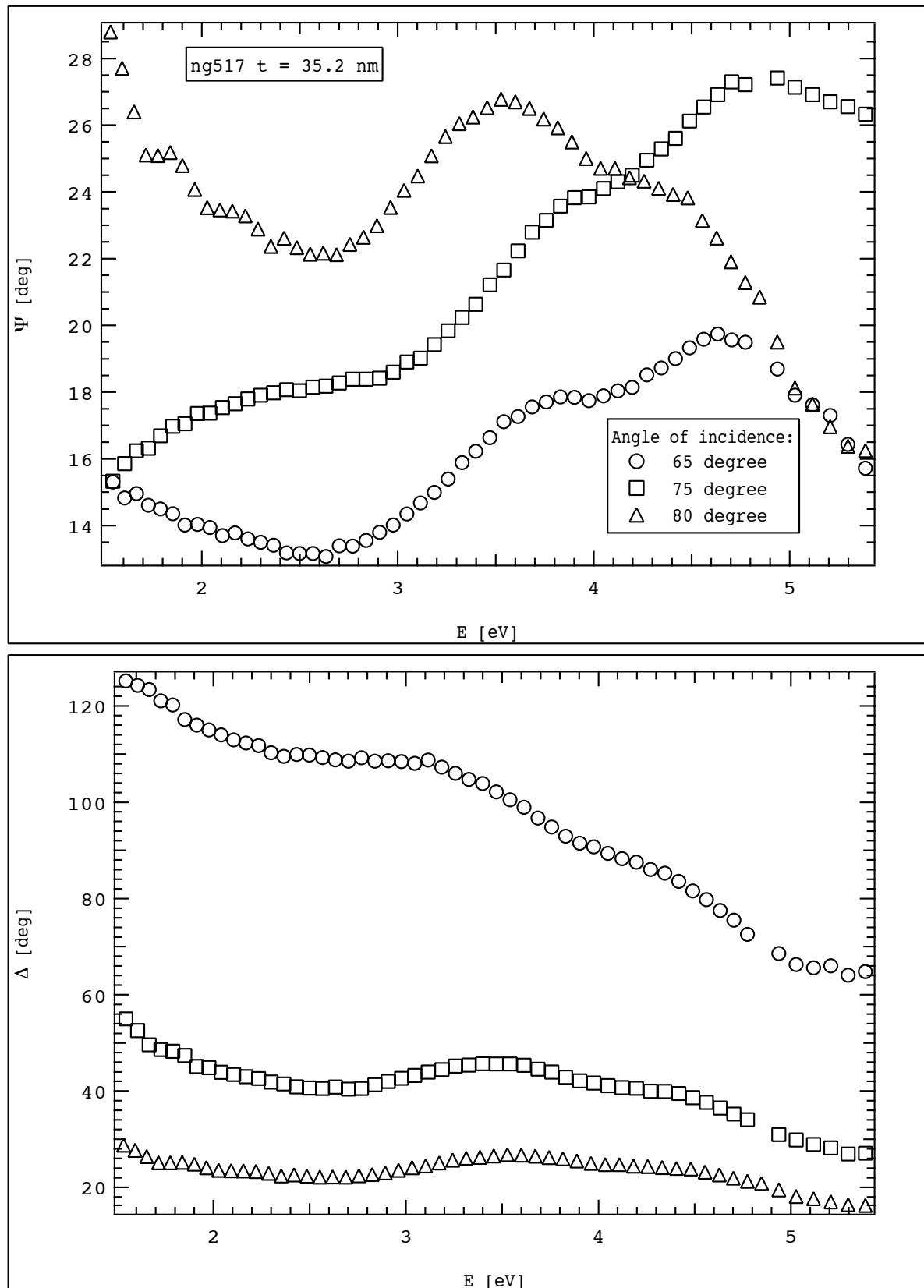


Figure 6.4: Experimental ellipsometric data of thin LSMO film deposited onto (100) STO substrate, measured at indicated angles of incidence.

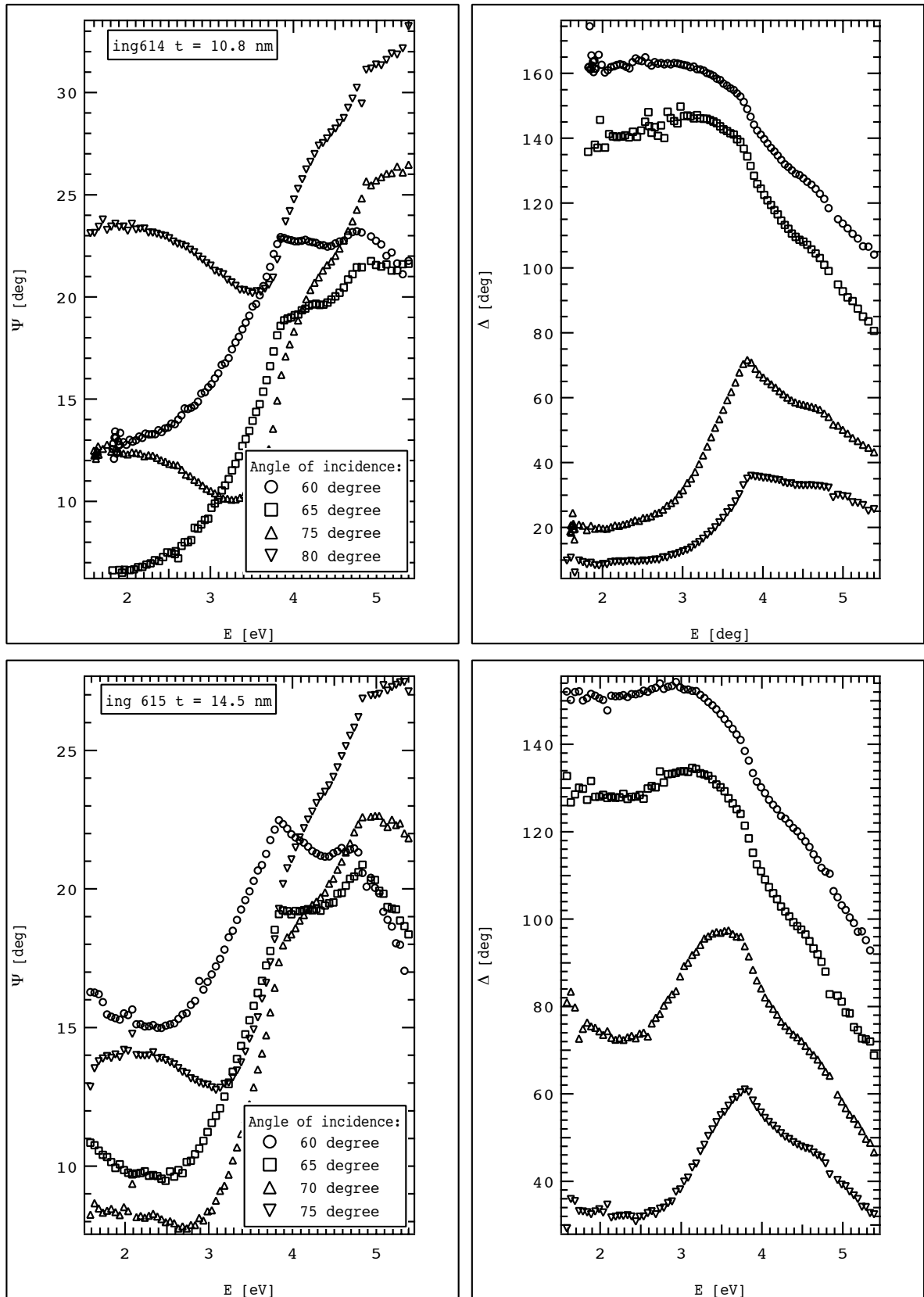


Figure 6.5: Experimental ellipsometric data of thin LSMO films deposited onto (110) STO substrates, measured at indicated angles of incidence.

6.2. SAMPLE DEPOSITION

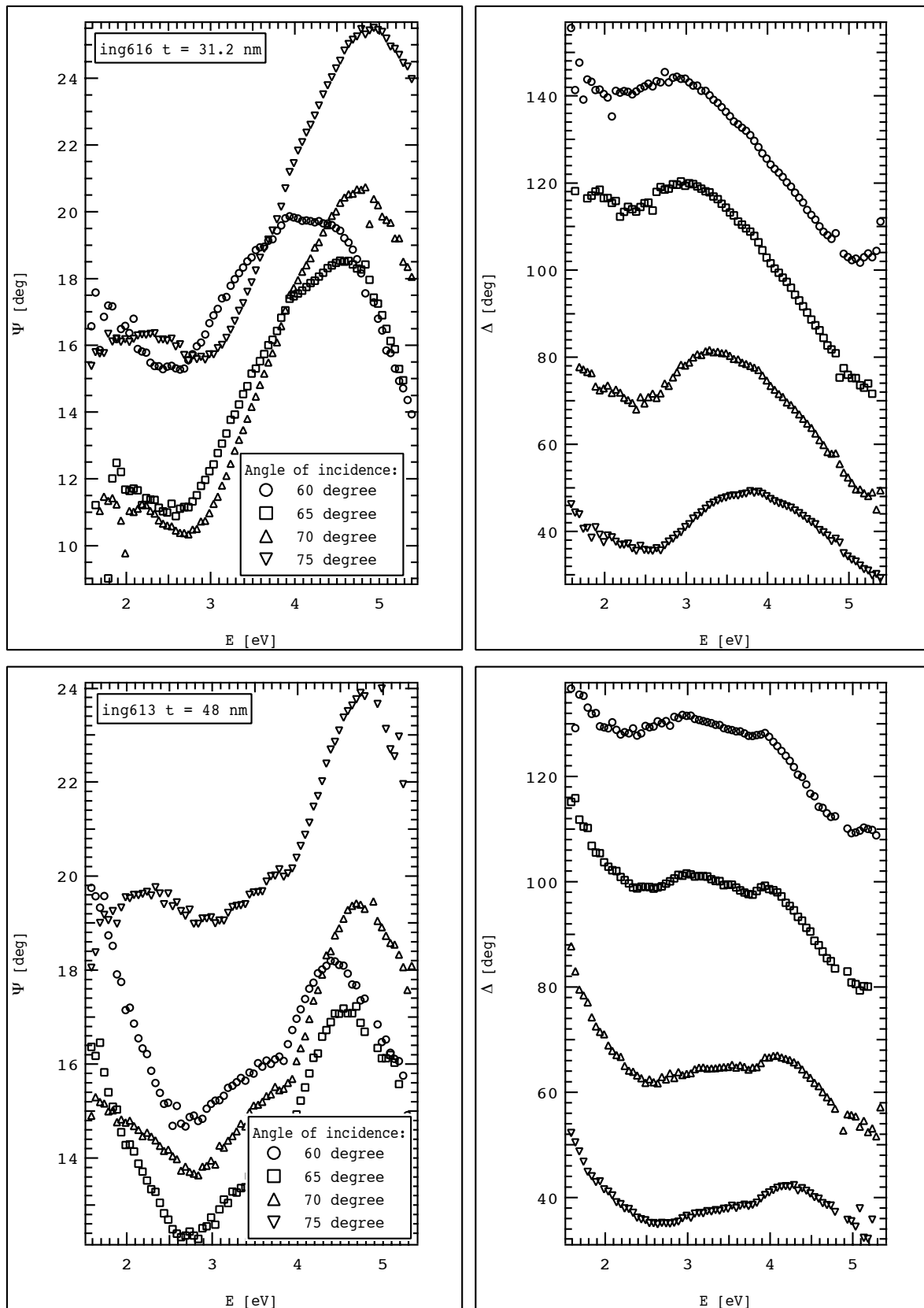


Figure 6.6: Experimental ellipsometric data of thin LSMO films deposited onto (110) STO substrates, measured at indicated angles of incidence.

6.3 Spectroscopic Ellipsometry

Ellipsometric parameters Ψ and Δ were measured by a computer controlled four-zone null spectroscopic ellipsometer (described in Chapter 5.) in the spectral range from 1.5 to 5.4 eV (wavelength region from 230 to 840 nm). Spectra of Ψ and Δ with variable incident angle were recorded. These spectra are shown for both (100) and (110) STO substrate orientations in Figs. 6.3, 6.4, 6.5 and 6.6. Diagonal permittivity spectra of investigated films were parametrized by the sum of three damped Lorentz oscillators and non-dispersive term. According to Eq. (5.16), we get

$$\varepsilon_1 = \varepsilon_{1\infty} + \sum_{n=1}^3 \frac{A_n E_n^2}{E_n^2 - E^2 + i\Gamma_n E_n E}. \quad (6.1)$$

The least square method was used (with the ellipsometric angles projected on the Poincaré sphere) to adjust the transition energy E_n , strength A_n and broadening Γ_n for each oscillator, as well as the thickness t of the film. Computed thicknesses of all samples are summarized in Tab. 6.1. In the following text we will use the thicknesses derived from ellipsometry to label the samples.

Figures 6.7 and 6.8 show the spectral behavior of the diagonal elements of the dielectric tensor. These spectra were obtained by numerical analysis of measured ellipsometric quantities using the equation (6.1). We use them later to derive off-diagonal elements of the dielectric tensor from experimental magneto-optical spectra. As follows from Figs. 6.7 and 6.8, the optical constants (the diagonal elements of the dielectric tensor) exhibit similar amplitude and spectral behavior independently on the crystallographic orientation of the STO substrate. We can consider the same optical transitions in both sets of samples. This was expected owing to the same target material used for the deposition of both sets of samples. Slight variation of the ε_{xy} spectra with the LSMO layer thickness indicates the thickness dependent film and surface properties with respect to partial relaxation of the tensile strain induced by STO substrate.

These results are consistent with those reported by Liu *et al.* [69] on LSMO films with thicknesses above 50 nm, i.e. thicker than those which are studied here. Owing to the fact that published optical investigations have been mainly done by reflectivity measurements, we calculated the reflectivity and optical conductivity of LSMO layers, using the optical constants obtained from ellipsometry. These results are shown in Fig. 6.9 and are consistent with previously published studies [63, 85].

The spectroscopic ellipsometry fits revealed three transitions in LSMO films centered near 1 eV, 4 eV and 7 eV. The transition near 1 eV exhibits the biggest broadening and the largest amplitude. Assuming that Sr doping introduces holes in the Mn e_g - derived levels, we expect that the transition should involve these levels [63]. Kaplan *at. al* [63] in their study of

6.3. SPECTROSCOPIC ELLIPSOMETRY

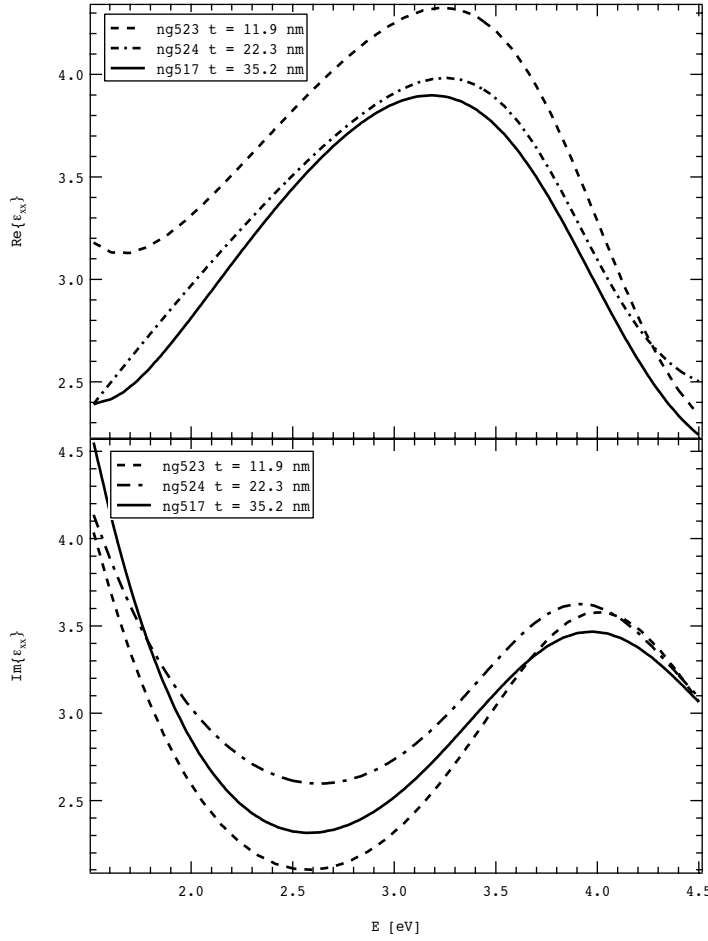


Figure 6.7: Spectra of the real and imaginary part of the diagonal element ϵ_{xx} of the permittivity tensor in the LSMO films grown on (100) STO substrates computed from the spectroscopic ellipsometry data.

$\text{Nd}_{0.7}\text{Sr}_{0.3}\text{MnO}_3$ thin films found the strong temperature and magnetic dependence of the optical conductivity peak near 1 eV. This peak is evident in the paramagnetic phase and loses its intensity when the temperature is decreasing below the T_C . Owing to these observations, either the initial or final states of such transition must have large e_g components. We can therefore follow previous studies [63, 64] and assign this transition to the charge transfer from the Mn^{3+} e_g states to the unoccupied Mn^{4+} states on an adjacent site. The next transition derived from ellipsometry is centered near the energy of 4 eV and can be assigned to the charge transfer excitation from O $2p$ to Mn $3d$ states ($\text{O } 2p \rightarrow e_{g\uparrow}^2$)[65, 66, 85, 64, 86]. To analyze the last optical transition centered near 7 eV is more difficult, since most of the previous optical studies did not cover this energy region. Jung *et al.* [65] observed an electric dipole allowed transition near 7.7 eV in LaMnO_3 polycrystalline samples and assigned it to the minority spin charge transfer

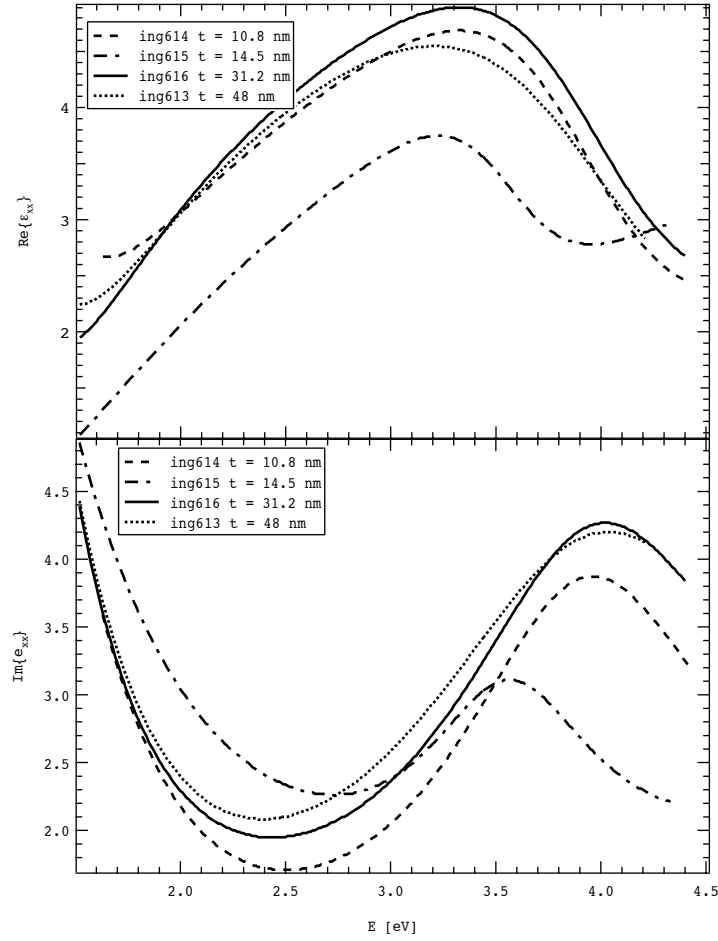


Figure 6.8: Spectra of the real and imaginary part of the diagonal element ϵ_{xx} of the permittivity tensor in the LSMO films grown on (110) STO substrates computed from the spectroscopic ellipsometry data.

excitation $\text{O } 2p \rightarrow e_{g\downarrow}^2$. The transition energy is higher than in our case. However, since he reported [87] the decrease of JT splitting with Ca doping, we can expect similar behavior in the case of Sr doping. Therefore, the transition energy can be shifted toward the lower energies and we can associate the optical transition observed near 7 eV to the same charge transfer excitation.

6.4 Magneto-optical spectroscopy

The magneto-optical spectra were measured in both polar and longitudinal geometries. According to the results from the superconducting quantum interference device (SQUID) magnetometer for the samples deposited on (100) STO substrates, the magnetizations of the films

6.4. MAGNETO-OPTICAL SPECTROSCOPY

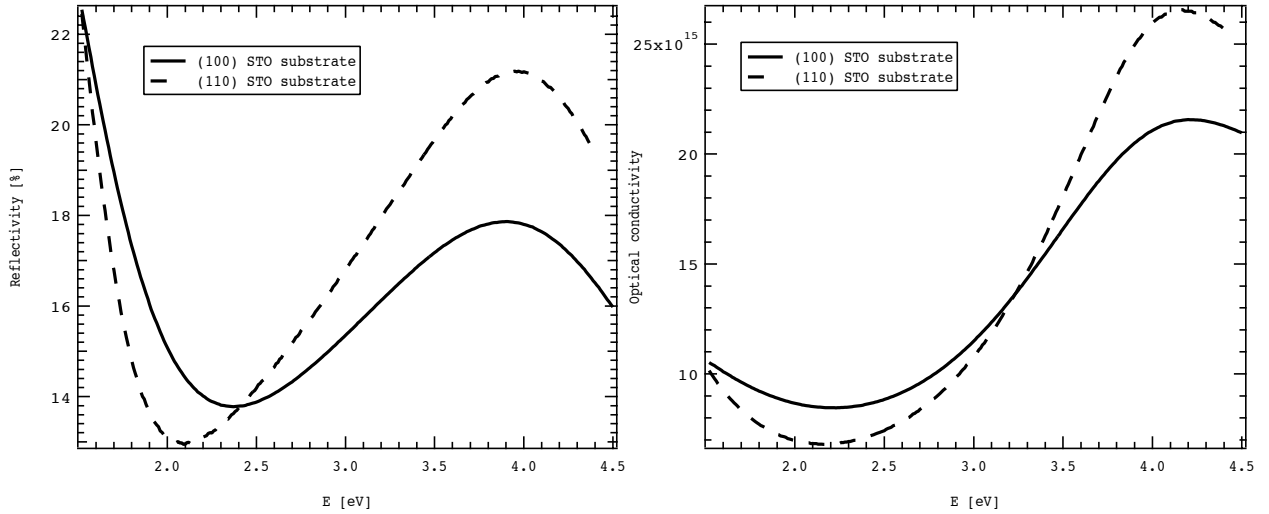


Figure 6.9: Optical reflectivity and conductivity of LSMO films on the (100) and (110) oriented STO substrates. The spectra were computed using ε_{xx} derived from samples ng517 ($t = 35.2$ nm) and ing616 ($t = 31.2$ nm).

are strongly temperature dependent in the vicinity of 300 K and the Curie temperatures (T_C) are around 330 K. On the other hand, samples deposited on (110) substrates exhibit higher T_C around 345 K. For both crystallographic orientations, T_C depends on the film thickness. To ensure the reasonable spectra, the experiment had to be performed at a stabilized temperature of 285 K for all samples in the polar geometry and ambient temperature of 295 K in the longitudinal geometry. Applied magnetic field was as high as 470 mT in the polar geometry, while in the longitudinal geometry was 100 mT. This was sufficient to achieve magnetic saturation of the samples.

Figures 6.10 and 6.11 display experimental Kerr rotation and ellipticity spectra measured in polar configuration for samples deposited on (100) and (110) STO substrates. These results have similar overall spectral behavior with previously published magneto-optical studies on thick films [69, 71, 74], single crystals [68], and bulk crystalline pellets [67]. We have to note that the thicknesses of our films are smaller than the thicknesses of samples in other studies. In such thin films, the change in optical and magneto-optical properties compared to the bulk material is expected.

Polar Kerr rotation spectra exhibit two main spectroscopic peaks of opposite signs near energies 2.6 and 3.6 eV. The thickness dependence of the amplitude and broadening of the peak centered at 3.6 eV are also evident. Polar Kerr ellipticity reaches its maximum near 3.2 eV and minimum near 4.2 eV with similar amplitude.

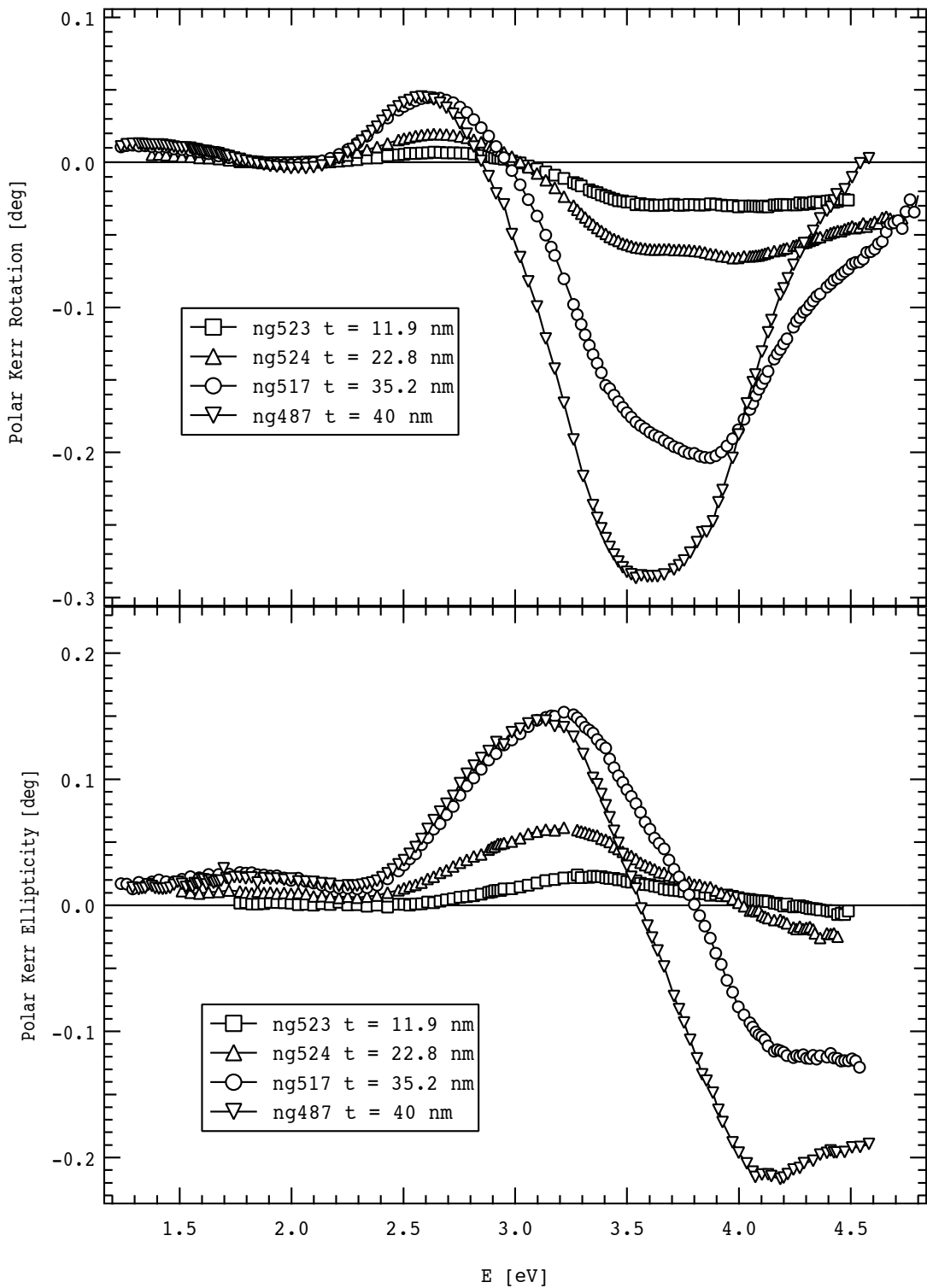


Figure 6.10: Experimental polar Kerr spectra of LSMO thin films deposited on (100) STO substrates measured at nearly normal incidence.

6.4. MAGNETO-OPTICAL SPECTROSCOPY

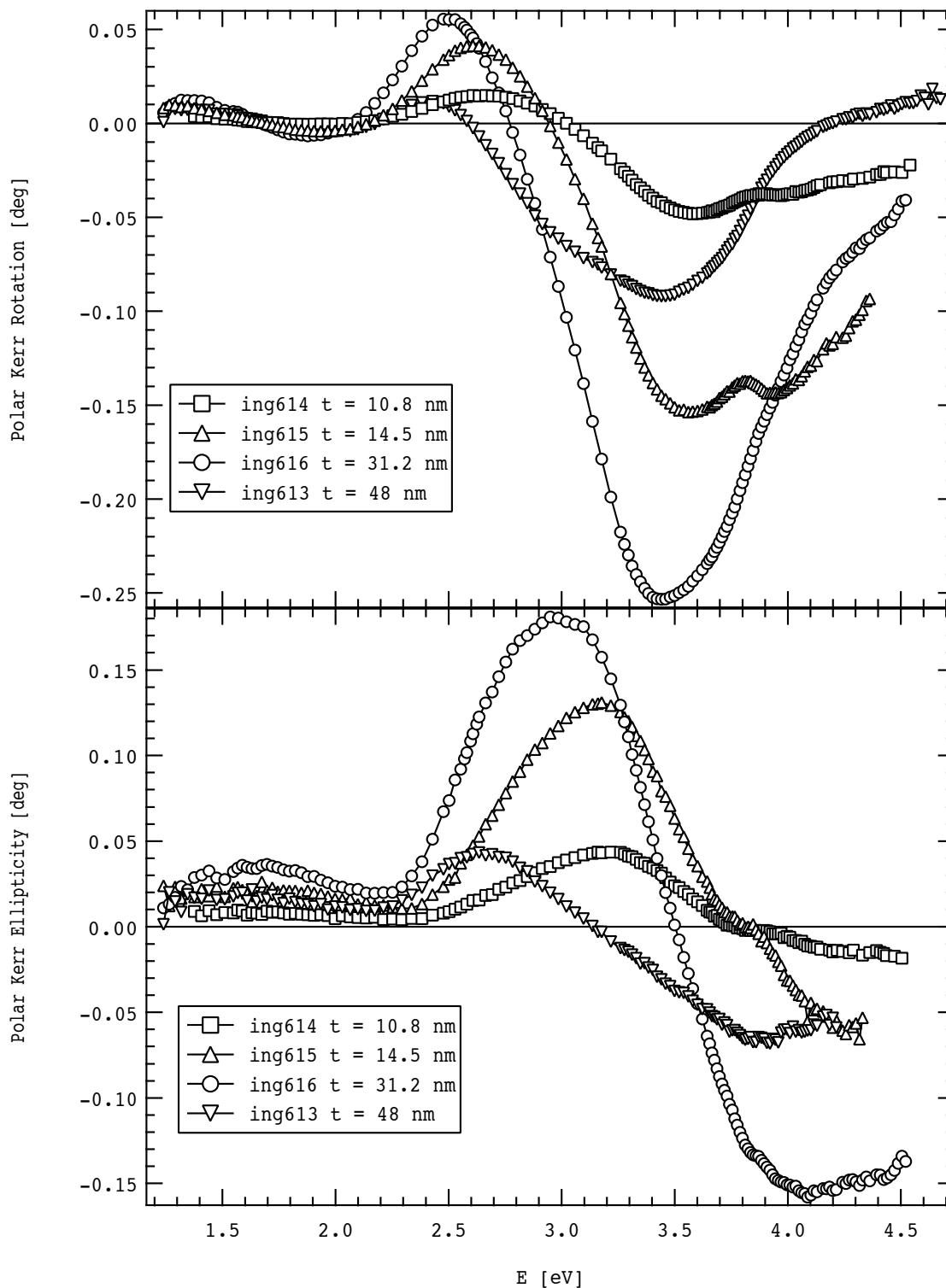


Figure 6.11: Experimental polar Kerr spectra of LSMO thin films deposited on (110) STO substrates measured at nearly normal incidence.

These spectral features of the polar Kerr effect are consistent with Kramers-Kronig relations [88] (Kerr rotation exhibits a positive or negative peak when ellipticity has an inflexion). Comparing the spectra for the samples deposited on (100) and (110) STO substrates, we found two significant differences. Firstly, the amplitude of polar Kerr effect for the sample with thickness 48 nm deposited on (110) STO substrates is notably smaller with respect to the thickness dependence observed for the samples deposited on (100) STO substrates. Secondly, there is a higher energy shift of the spectral peaks toward lower energy side for the films with thicknesses 31.2 nm and 48 nm deposited on (110) STO substrates than for the thicker films deposited on (100) substrates. Moreover, all films deposited on (110) STO substrates exhibit overall higher amplitude of the polar Kerr effect with respect to their thicknesses, except the sample ing613 ($t = 48$ nm) as was mentioned above. We will discuss these features in the next paragraphs. However, despite all these facts, we can observe the same splitting of the polar Kerr rotation peak centered near 3.6 eV for thinner LSMO films deposited on both types of substrates. This effect originates from the STO substrates and is more pronounced at the (110) substrate orientation. To confirm our theory, we calculated the penetration depth of incident light using optical constants shown in Figs. 6.7 and 6.8. Spectral dependence of the penetration depth for LSMO films deposited on both types of substrates is displayed in Fig. 6.12. As follows from this figure, the penetration depth of the incident light with energy 3.8 eV (position of the splitting peak) is less than 30 nm. Therefore, the light is propagating through the film and reflecting on the interface between the substrate and LSMO film. With respect to the dramatic change of the phase of the reflection coefficient of STO (see Fig. 6.13) this reflection makes a contribution to the magneto-optical spectra and is in agreement with our experimental results.

Longitudinal Kerr rotation spectra were measured at an oblique angle of incidence of 54° with the incident linear polarization either perpendicular (s) or parallel (p) to the plane of incidence. Figures 6.14 and 6.15 show the experimental results for both substrate orientations. As follows from the Fig. 6.14, the spectra are similar in shape to those measured at polar configuration. They exhibit positive peak with the maximum near 2.7 eV and negative peak with the minimum near 3.9 eV. The situation becomes more complicated in the case of STO (110) substrate. Although the overall spectral behavior is similar as for the (100) STO substrate, the spectrum of the thickest LSMO film (sample ing613 $t = 48$ nm) notably differs from the rest of the samples. Apart from this feature, we did not observe any additional spectral peak in longitudinal Kerr rotation spectra. Moreover, we did not observe the peak splitting near 3.8 eV for thinner LSMO layers as in the polar configuration. This is the consequence of the oblique incidence and therefore longer optical path of the light in the LSMO layer.

To investigate the microscopic origin of the magneto-optical effect, we computed the off-diagonal elements of the dielectric tensor using the knowledge of the MO spectra and optical

6.4. MAGNETO-OPTICAL SPECTROSCOPY

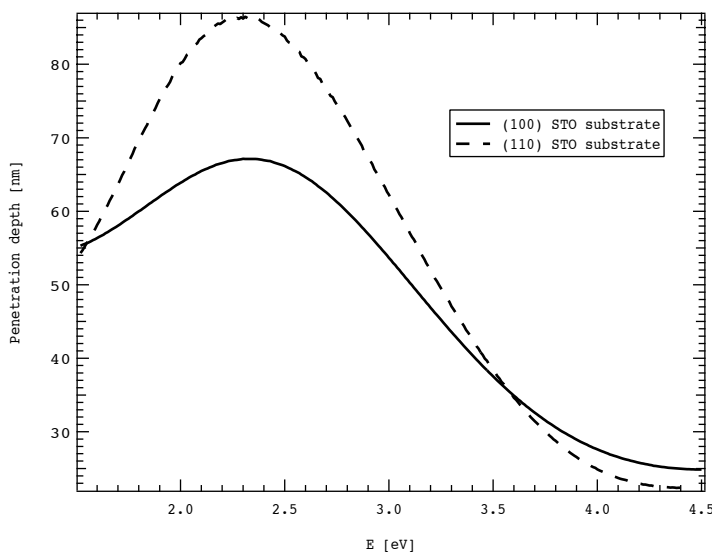


Figure 6.12: Computed penetration depth in LSMO films on (100) and (110) STO substrates as a function of photon energy. The material parameters, ε_{xx} , of LSMO films are those of samples ng517 ($t = 35.2$ nm) on (100) STO substrate and ing616 ($t = 31.2$ nm) on (110) STO substrate.

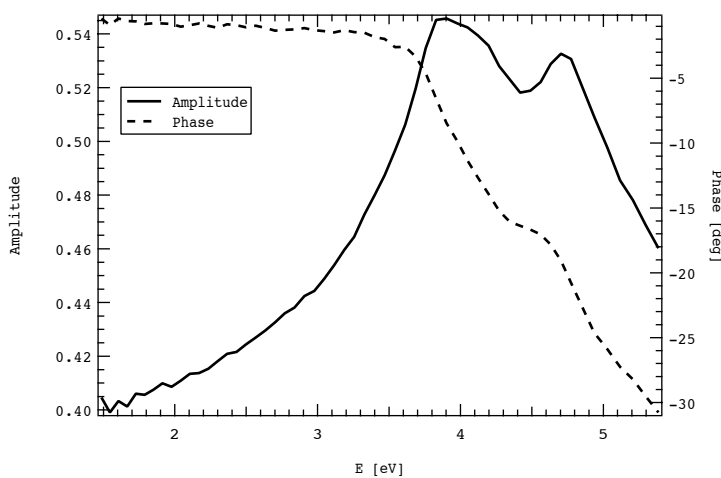


Figure 6.13: Amplitude and phase of the reflection coefficient of bulk STO calculated for the normal incidence.

constants of LSMO layers. Owing to small thicknesses of investigated films and high penetration depth, we considered a model structure consisting of a thin homogenous LSMO layer on a semi-infinite STO substrate (the bottom surface of the substrate was ground and therefore it does not need to be considered in the calculations). The spectra of the off-diagonal elements of the dielectric tensor for LSMO thin films deposited on (100) and (110) STO substrates are

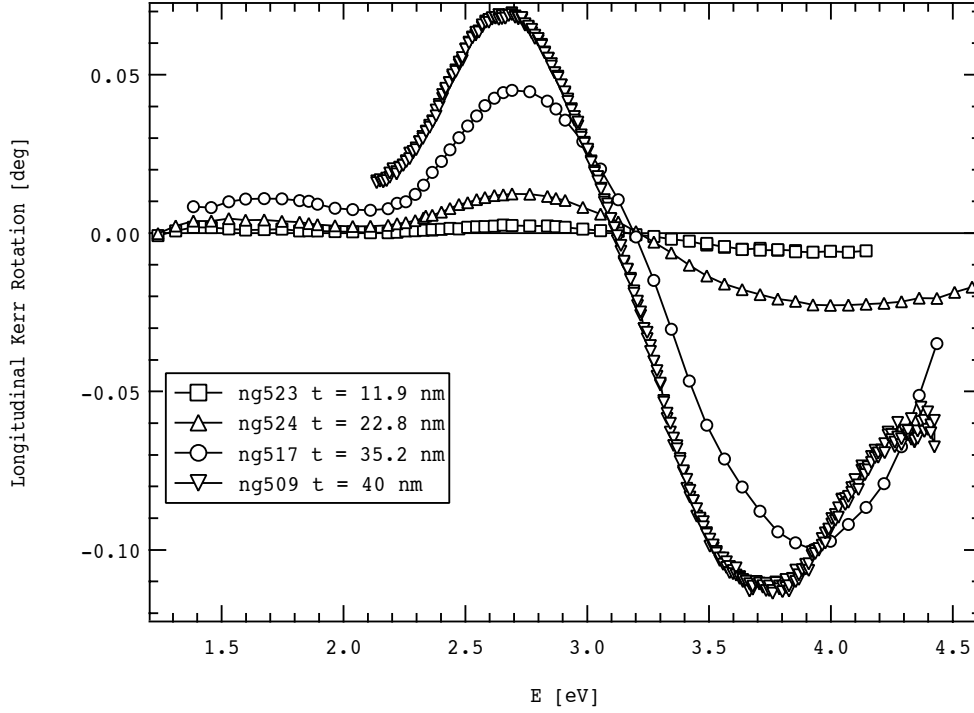


Figure 6.14: Room temperature longitudinal Kerr rotations of LSMO films grown on (100) STO substrates measured as $Re\{r_{ps}/r_{pp}\}$ ratio corresponding to the incident polarization parallel to the plane of incidence. The angle of light incidence was 54° .

displayed in Figs. 6.16 and 6.17.

Two spectroscopic features are clearly visible centered near energies 2.4, and 3.6 eV. With respect to the theoretical classification described in Chapter 3 we can assign the first one to type-II paramagnetic transition and the second one to type-I diamagnetic transition. Both transitions are thickness dependent and we will discuss this dependence in the last paragraph of this chapter.

Let's now compare these findings with previously published results. The presented spectra of the off-diagonal elements have the same spectral behavior with those deduced by Balykina *et al* [75] from transverse magneto-optic Kerr effect on $\text{LaMnO}_{3.11}$ bulk crystals. Moreover, they assigned the same two transitions: one paramagnetic transition at 2.4 eV and one diamagnetic transition at 3.55 eV. Liu *et al.* [69] observed rich spectra, including many spectroscopic features, and described type-I transitions at energies 3.3, 4.1 and 4.7 eV, while type-II transitions at energies 2.5, 3.1 and 3.6 eV. However, the main spectral features of their results remain the same. The results presented by Yamaguchi *et al* [68] are comparable in the energy range from 2 eV to 4.5 eV. We didn't observe strong peak at 1.2 eV, but we observed the same type-I transition peak at energy around 3.5 eV.

6.4. MAGNETO-OPTICAL SPECTROSCOPY

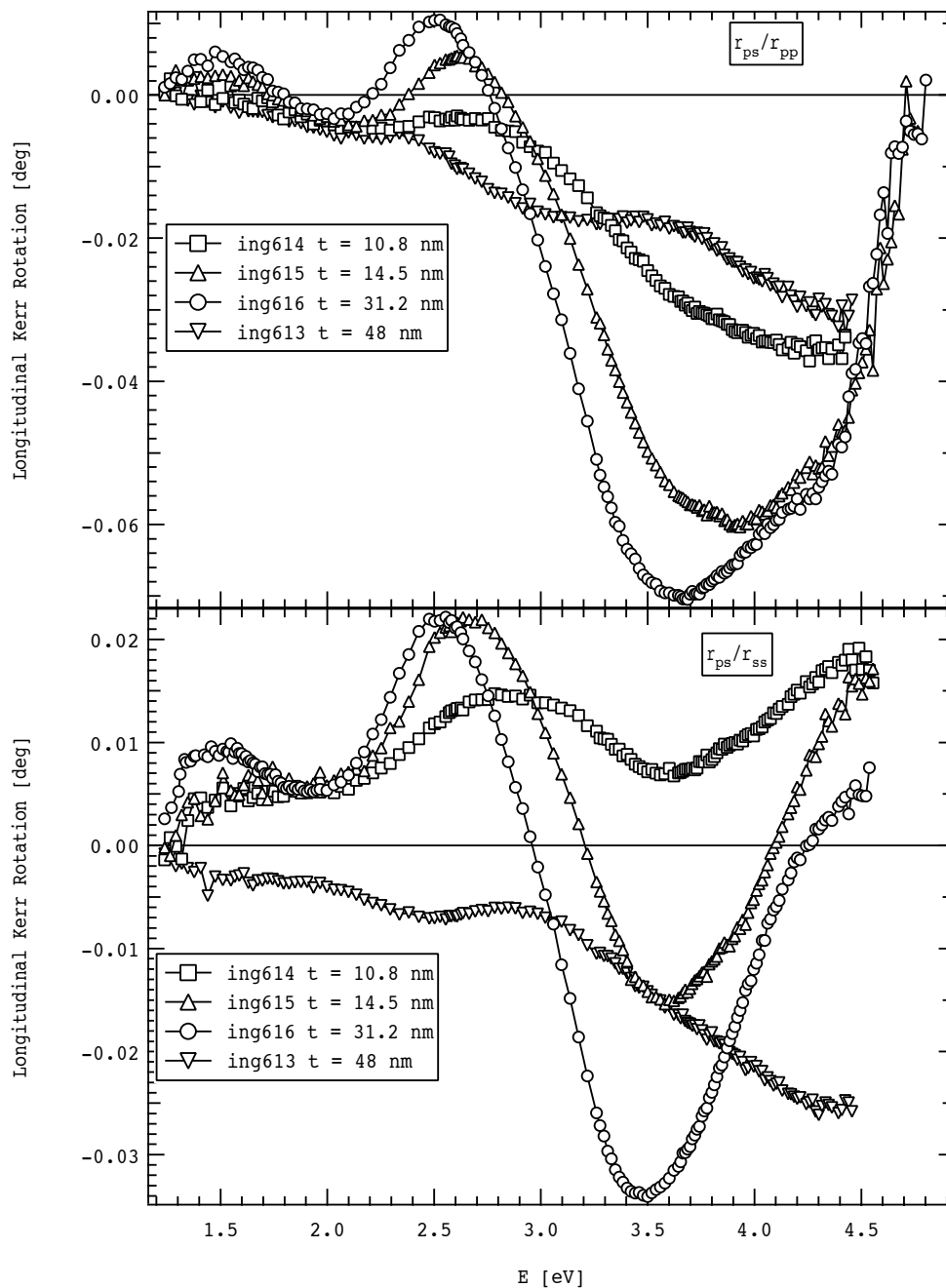


Figure 6.15: Room temperature longitudinal Kerr rotations of LSMO films grown on (100) STO substrates measured as both $Re\{r_{ps}/r_{pp}\}$ and $Re\{r_{ps}/r_{ss}\}$ ratios corresponding to the incident polarizations parallel and perpendicular to the plane of incidence. The angle of light incidence was 54° .

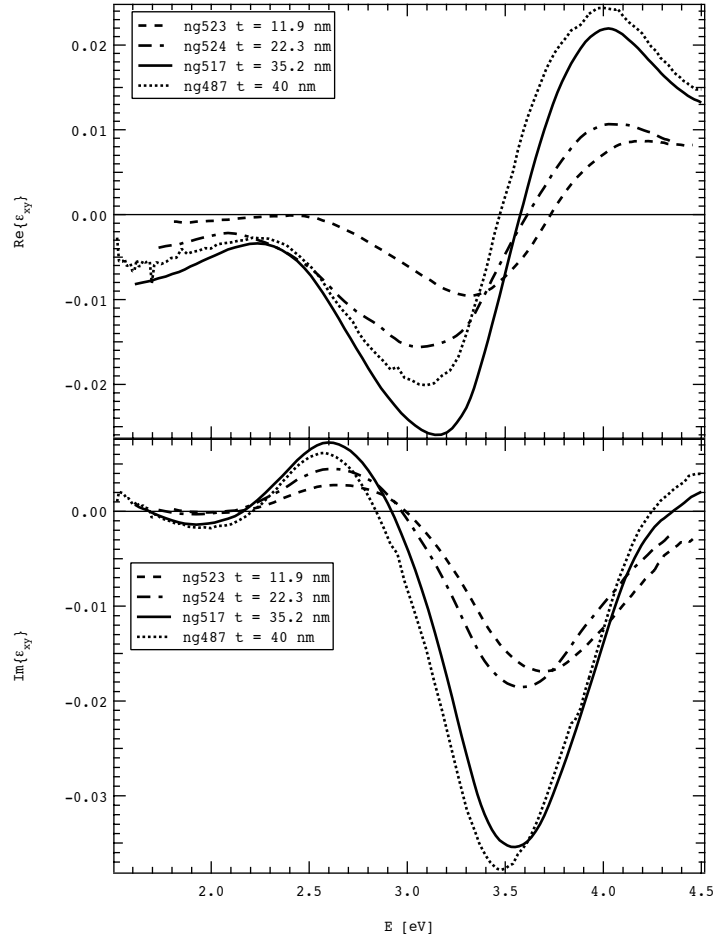


Figure 6.16: Spectra of the off-diagonal permittivity tensor element, ε_{xy} , of LSMO films grown on (100) STO substrates. For the film thicknesses, $t = 11.9, 22.3,$ and 35.2 nm, ε_{xy} was computed from the corresponding polar Kerr rotation and ellipticity. For $t = 40$ nm, ε_{xy} was computed from the corresponding polar Kerr rotation and ellipticity measured for the sample ng517 ($t = 35.2$ nm).

To describe observed transitions in detail and make their assignment, we parametrized the off-diagonal elements spectra obtained from the experiment (Figs. 6.16 and 6.17) by the summation of two shapes (one paramagnetic, one diamagnetic) using Eqs. (3.43) and (3.39). We fit the ε_{xy} spectra with the highest amplitude for both types of STO substrates. The results are shown in Figs. 6.18 and 6.19. A reasonable agreement between the fits and experimental data was achieved. Parameters of all transitions are summarized in Tab 6.2. Comparing the results for both types of substrates we didn't find any significant difference, which reflects the same electronic transitions. However, the transitions in the samples deposited on (110) STO substrates exhibit higher amplitude $(\varepsilon_2)_{max}$. Since the lowest transition energy is higher than

6.4. MAGNETO-OPTICAL SPECTROSCOPY

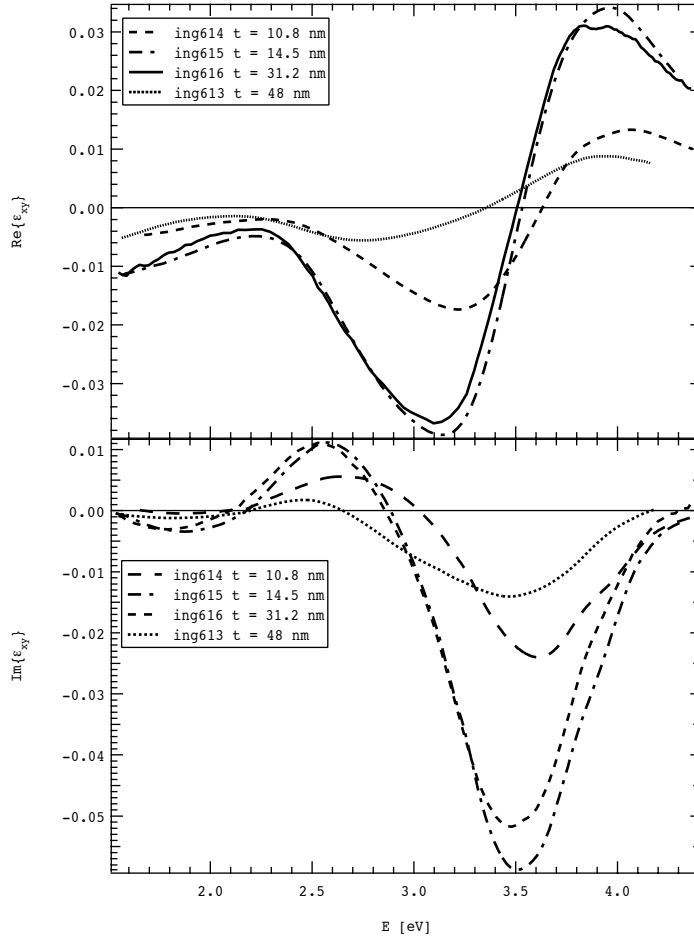


Figure 6.17: Spectra of the off-diagonal permittivity tensor element, ε_{xy} , of LSMO films grown on (110) STO substrates computed from the corresponding polar Kerr rotation and ellipticity.

2 eV, we can not assign any of them to the intraband majority spin hole transition between Mn e_g and O $2p$ states, as Yamaguchi did for the transition near 1.2 eV [68]. The lower energy, broader, paramagnetic transition has smaller oscillator strength compared to the diamagnetic one. Examples of paramagnetic transitions are the crystal field transitions of Fe^{3+} ions [30]. Therefore, we assign this transition to the spin-allowed, electric dipole-forbidden Mn $3d$ crystal field majority spin transition between t_{2g} and $e_{g\uparrow}^1$ energy levels. This is consistent with previous studies [69, 67]. The second, diamagnetic transition centered near energy 3.6 eV has notably higher oscillator strength and smaller broadening. This type of transition has the origin in the spin-orbit splitting in the final state. Since the orbital angular momentum of $3d$ transition-metal ions is zero owing to the crystal field splitting [89], we follow Yamaguchi [68] and consider the splitting of the final state as the combined effect of exchange field and spin-orbit coupling. Thus, we can assign this transition to the dipole-allowed minority spin charge transfer transition

(100) STO substrate			
Type	$(\varepsilon_2)_{max}$	E_0 (eV)	Γ (eV)
paramagnetic	0.022	2.39	0.39
diamagnetic	0.083	3.58	0.78
(110) STO substrate			
Type	$(\varepsilon_2)_{max}$	E_0 (eV)	Γ (eV)
paramagnetic	0.038	2.38	0.48
diamagnetic	0.116	3.54	0.73

Table 6.2: Resulting fitting parameters obtained from the fits of ε_2 spectra of LSMO thin films deposited on both types of STO substrates.

from filled O $2p$ into empty t_{2g} Mn $3d$ levels. Schematic view of the electronic structure of bulk LSMO with all transition revealed by optical and magneto-optical measurements is shown in Fig. 6.20.

Now we will discuss the thickness dependence of the polar and longitudinal Kerr spectra and off-diagonal elements of the dielectric tensor. In the set of samples deposited on (100) STO substrates, the amplitude of Kerr effect is increasing with increasing thickness. The most perceptible is this effect for the peak centered near 3.5 eV. With the knowledge of the diagonal and off-diagonal elements of the dielectric tensor we calculated the thickness dependences of the polar and longitudinal Kerr effects for both types of substrates at selected photon energies corresponding to the peaks in each spectrum. These dependences are displayed in Fig. 6.21. Comparing the calculation with experimental values, one can see a deviation of the experimental data from the linear behavior for low thicknesses. These deviations are higher for (100) STO substrates than for (110) STO substrates, which indicates slower onset of the magnetization for the films deposited on (100) STO substrates. This is consistent with the differences in the growth mechanisms of LSMO on (100) and (110) STO substrates [90].

The amplitude of Kerr effect is related to ferromagnetic order inside the material. A higher degree of magnetic ordering results in higher magneto-optical amplitudes. In manganese oxides is this order dominated by the double-exchange interaction between Mn^{4+} and Mn^{3+} ions [91]. Several mechanisms such as oxygen content [92], annealing procedure [93] external pressure [94] can influence the double exchange mechanism. However, the most important role plays the strain induced by the lattice mismatched substrate [95, 96, 97, 98, 99, 100]. Because the substrate induces a strain symmetry in the growth plane, three dimensional strain states can be decomposed into a bulk strain ε_B and a biaxial strain (Jahn - Teller term) ε_{JT} [95]. Both these terms have opposite influence upon ferromagnetic order and T_C . The extension / contraction of

6.4. MAGNETO-OPTICAL SPECTROSCOPY

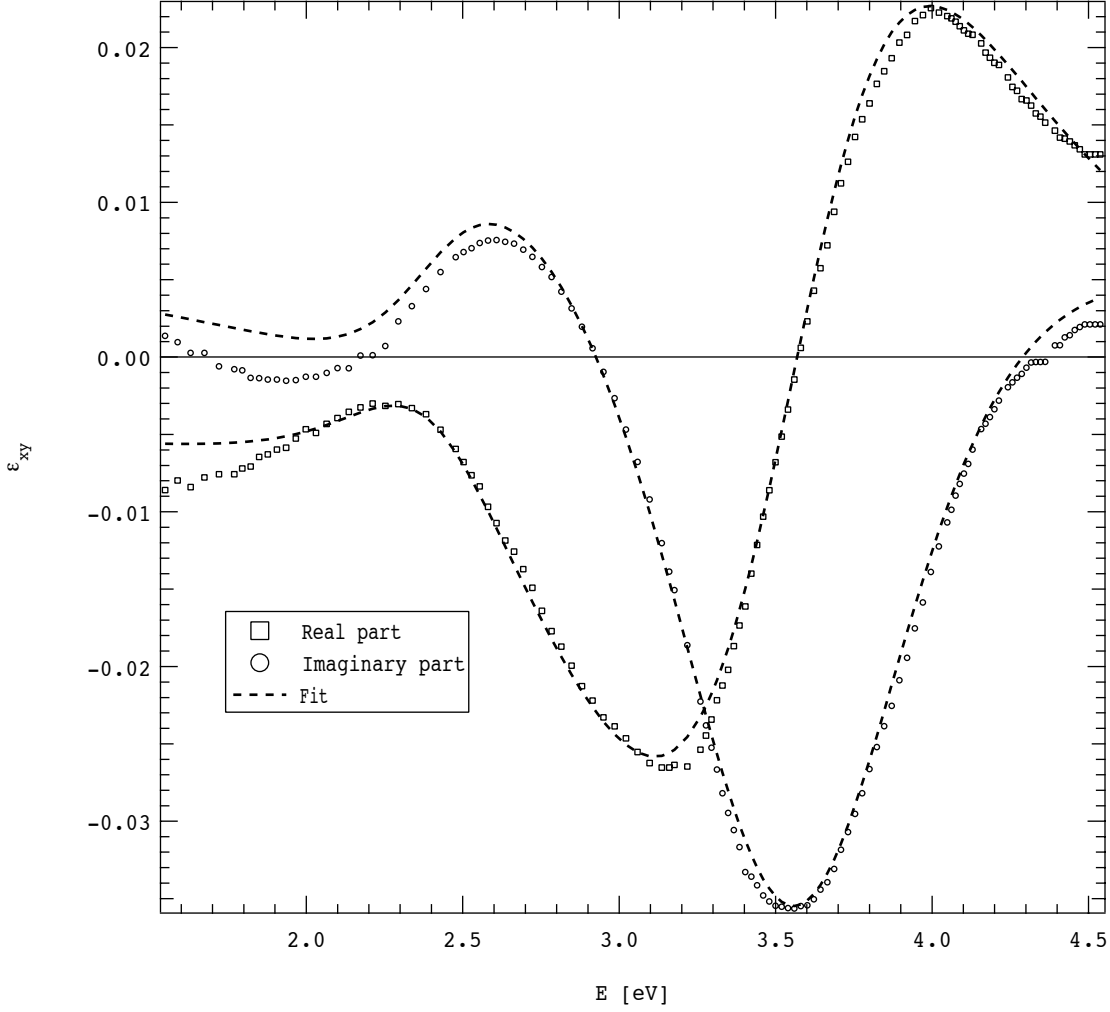


Figure 6.18: Comparison of ε_{xy} spectra derived from experiment (dots) with theoretical fit for the LSMO thin film deposited on (100) STO substrate.

bonds and change of the Mn-O-Mn bond angle due to ϵ_B leads to a reduction / enhancement of the electronic hopping amplitude and ferromagnetic order as was described with respect to the double-exchange model. The increased ϵ_{JT} , on the other hand, renders the effective local potential deeper, trapping electrons. This results in spin-disorder, localization effect of Mn $3d$ majority spin e_g orbitals [101] and suppression T_C . Since we used a lattice mismatched STO substrates and LSMO films are very thin, our samples are fully strained and their T_C is lower than the bulk value [102]. With the thickness increase, the strain can partially relax and the ferromagnetic order can be enhanced, resulting in the increase of T_C . This was confirmed by X-ray diffraction and SQUID magnetometer measurements as well as reported by other authors [103]. Therefore we can explain the thickness dependence of the polar Kerr effect amplitude partly as the effect of the light propagation in the film [73] and partly as the relaxation of the

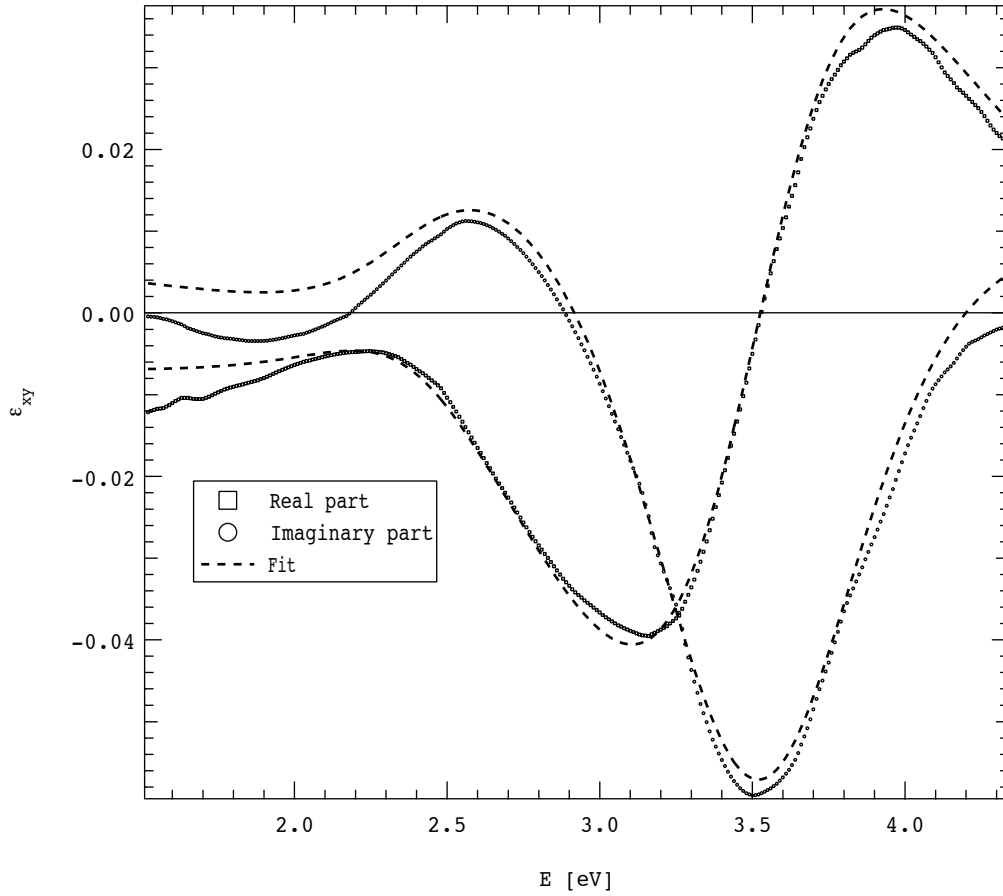


Figure 6.19: Comparison of ε_{xy} spectra derived from experiment (dots) with theoretical fit for the LSMO thin film deposited on (110) STO substrate.

tensile strain induced by substrate.

However, this situation becomes more complicated when we look at the spectra of the films deposited on (110) STO substrates. In this case, the amplitude of both polar and longitudinal Kerr effect for the sample with thickness 48 nm is smaller compared to 31.2 nm thick sample. Even if the thickness is already out of the linear dependence with respect to the Fig. 6.21, the suppression of the amplitude is much higher than expected from the theory. To explain these results (also confirmed by SQUID magnetometer measurements) we can not simply consider only the influence of the strain on ferromagnetic order in LSMO. It was found [93, 104] that also oxygen content and its stoichiometry plays an important role in magnetic and electronic properties of manganese oxides. If the oxygen content is non-stoichiometric, the $\text{Mn}^{3+}/\text{Mn}^{4+}$ ratio is lower, which causes a reduced ferromagnetic order [105]. Moreover, different growth speed and magnetic properties of LSMO films deposited on (100) and (110) STO substrates were reported [62]. Therefore we will explain the decrease of the polar and longitudinal Kerr

6.4. MAGNETO-OPTICAL SPECTROSCOPY

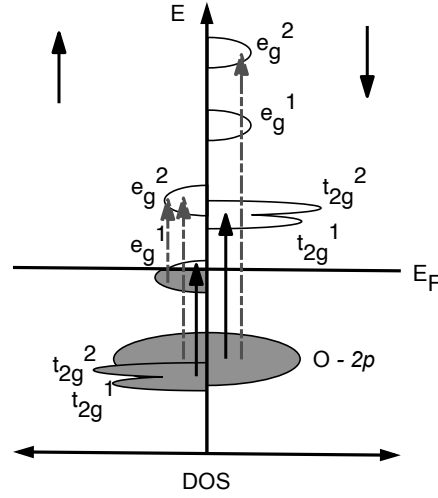


Figure 6.20: Schematically shown electron transitions observed in LSMO thin films deposited on both types of STO substrates. Grey dashed arrows denote the transitions observed in ellipsometric experiments, while black full arrows denote the transitions observed by magneto-optical spectroscopy.

effect amplitude of the 48 nm thick LSMO film as a change of the oxygen stoichiometry due to the structure change inside the film. However, detailed structural and magnetic investigations are necessary to confirm this hypothesis.

Owing to the knowledge of the complete information about the dielectric tensor, which was obtained from the spectroscopical ellipsometry and polar Kerr spectra, we calculated the model longitudinal Kerr rotation. Resulting spectral dependences of theoretical calculations for (100) STO substrates are shown in Fig 6.22. Comparing this figure with Fig. 6.14 one can see that the theoretical calculation describes the spectral behavior of experimental Kerr rotation very well. Small differences in amplitudes are assigned to the tensile strain as was explained above. In the films grown on (110) substrates, the agreement between experimental and theoretical spectra of longitudinal Kerr rotation is less satisfactory. This may be due to a difference between the diagonal in-plane tensor elements (ϵ_{xx} and ϵ_{yy}) and perpendicular ϵ_{zz} caused by optical anisotropy induced by strain.

Finally, we comment the thickness dependence of magneto-optically active diamagnetic transition centered near 3.6 eV. As follows from Figs 6.16 and 6.17, the energy of this transition shifts toward the lower energy side with increasing film thickness for both types of substrates. Since the electronic structure is very sensitive to the LSMO crystallinity, we can explained also this effect by the partial strain relaxation. While the substrate induced tensile stress is relaxing, the Mn-O bond in the a-b plane is contracted. This affects the Mn 3d electrons and shifts the

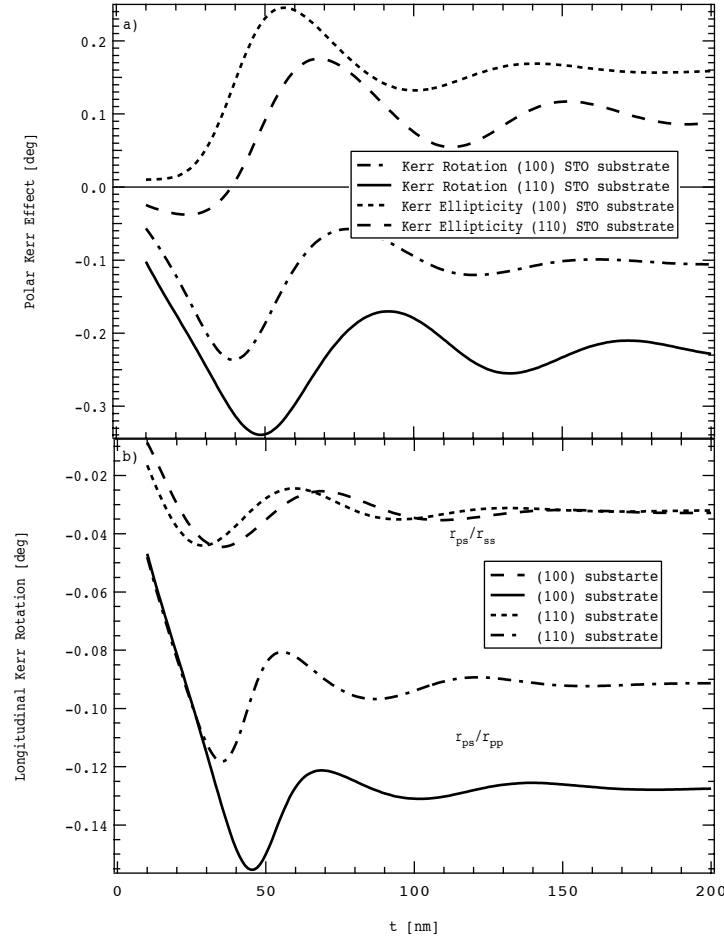


Figure 6.21: (a) Polar Kerr rotation and ellipticity as a function of thickness, t , of the LSMO films on STO substrate at a fixed photon energy. The curves for the (100) oriented STO substrate were computed at the photon energy of 3.87 eV using $\varepsilon_{xx} = 3.80 + j3.00$ and $\varepsilon_{xy} = 0.03 - j0.009$ for LSMO corresponding to sample ng517 ($t = 35.2$ nm) and $\varepsilon = 8.38 + j0.75$ for STO. The curves for the (110) oriented STO substrate were computed at the photon energy of 3.44 eV using $\varepsilon_{xx} = 4.10 + j4.00$ and $\varepsilon_{xy} = 0.03 - j0.02$ for LSMO corresponding to sample ing616 ($t = 31.2$ nm) and $\varepsilon = 10.3 + j4.2$ for STO. (b) Longitudinal Kerr rotation, $Re\{r_{ps}/r_{ss}\}$ and $Re\{r_{ps}/r_{pp}\}$ at an angle of incidence of 54° as a function of thickness, t , of the LSMO films on STO substrate at a fixed photon energy. The curves for the film on a (100) oriented STO substrate were computed at the photon energy of 3.93 eV using $\varepsilon_{xx} = 3.00 + j3.46$ and $\varepsilon_{xy} = 0.01 - j0.02$ for LSMO corresponding to sample ng517 ($t = 35.2$ nm) and $\varepsilon = 10.08 + j5.00$ for SrTiO₃. The curves for the (110) oriented STO substrate were computed at the photon energy of 3.69 eV using $\varepsilon_{xx} = 4.52 + j3.87$ and $\varepsilon_{xy} = 0.02 - j0.04$ for LSMO and $\varepsilon = 9.8 + j1.6$ for SrTiO₃ corresponding to sample ing616 ($t = 31.2$ nm).

6.5. CONCLUSIONS

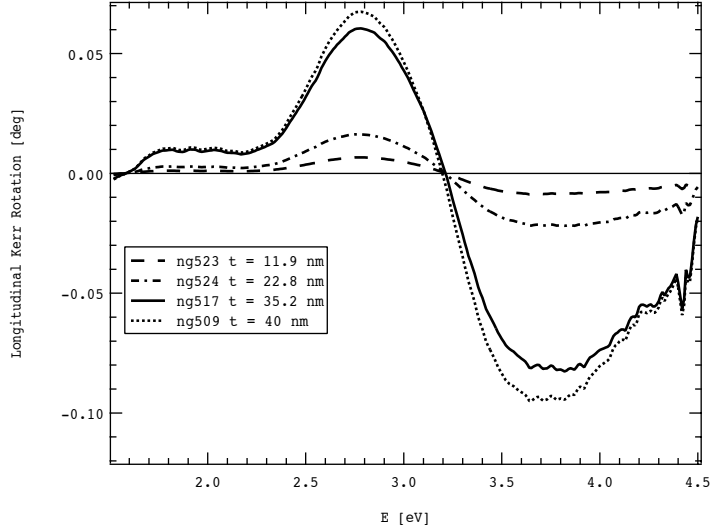


Figure 6.22: Computed longitudinal Kerr rotation, $Re\{r_{ps}/r_{pp}\}$, at an angle of incidence of 54° in LSMO films on (100) STO substrates. Each sample is characterized by its own ε_{xx} and ε_{xy} . The curves of sample ng509 ($t = 40$ nm) were obtained with the ε_{xx} of sample ng517 ($t = 35.2$ nm) as those for sample ng509 were not available.

minority spin t_{2g} levels closer to the Fermi energy [106]. Therefore, the energy of diamagnetic transition is shifting to the lower energy side.

6.5 Conclusions

We investigated optical and magneto-optical spectra of $\text{La}_{2/3}\text{Sr}_{1/3}\text{MnO}_3$ thin films deposited on (100) and (110) STO substrates. We described the electronic structure, optical and magneto-optical properties as well as their mutual dependences among with the crystalline structure. By comparing the results for samples deposited on both type of substrates, we found an insignificant influence of the crystallographic orientation of the substrate on optically and magneto-optically active transitions. However, a change of oxygen stoichiometry or structure change was found in the case of 48 nm thick sample deposited on (110) STO substrate. For thinner samples, the deviation from the linear thickness dependence of polar and longitudinal Kerr effect predicted by theory was observed. Moreover, the thickness dependence of magneto-optical transitions energies was found. This was explained by the partial relaxation of the tensile strain, induced by the lattice mismatched substrate. Altogether five transitions were observed in optical and magneto-optical spectra. They belong to both, charge transfer and crystal field splitting type transitions. Crystal field transitions, d to d are parity forbidden, while charge transfer d to p

CHAPTER 6. EXPERIMENTAL RESULTS ON $\text{La}_{2/3}\text{Sr}_{1/3}\text{MnO}_3$ THIN FILMS

transitions are allowed. Consistently with previously published studies charge transfer type transitions exhibit larger oscillator strength. Finally, the amplitudes of Kerr effect presented in this chapter are comparable with amplitudes of much thicker films and bulk crystals reflecting the high quality of investigated samples and a fully developed LSMO structure (except the sample ing613) even at such low thicknesses. This is an interesting result from the application point of view.

7 Experimental results on CuFe_2O_4 thin films

7.1 Material introduction

Copper ferrite, CuFe_2O_4 , is one of the ferrites formed due to the substitution of Fe^{2+} ions in isostructural Fe_3O_4 by another 3d transition metal ions. Such group of ferrimagnetic oxides, crystallizing usually in spinel structure, has been attracting considerably attention due to their use in magnetic recording and high frequency devices [107].

Spinel structure, named after the mineral spinel (MgAl_2O_4), has the general composition formula AB_2O_4 . An elementary cell is schematically shown in Fig. 7.1. It is essentially cubic with the O^{2-} ions forming a fcc lattice. The cations occupy 1/8 of the tetrahedral sites and 1/2 of the octahedral sites. There are 32 O^{2-} ions in the unit cell. In this work A-atoms denote Cu^{2+} ions while B-atoms denote Fe^{3+} ions.

Recent studies showed that the cation distribution in CuFe_2O_4 can be described by simple formula $(\text{Cu}_\alpha^{2+}\text{Fe}_{1-\alpha}^{3+})[\text{Cu}_{1-\alpha}^{2+}\text{Fe}_{1+\alpha}^{3+}]\text{O}_4^{-2}$, in which parentheses and square brackets denote tetra-

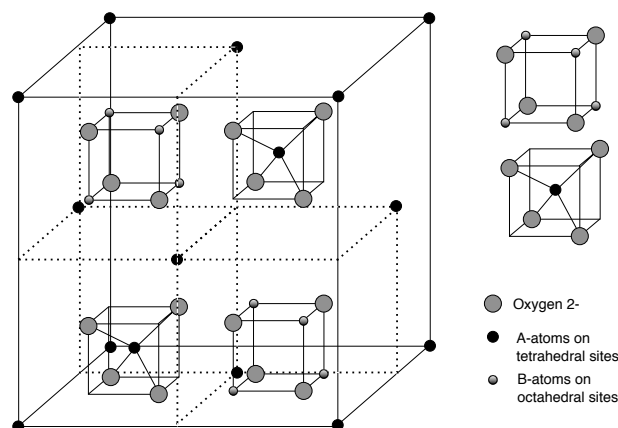


Figure 7.1: The elementary cell of general AB_2O_4 spinel structure after Krupička [108]. The basic small cubes are also contained in the back half of the unit cell.

hedral and octahedral sites, respectively. Tetragonal CuFe_2O_4 is completely inverse ($\alpha = 0$). The ground state of a cubic octahedrally coordinated Cu^{2+} ion is ${}^2E_g(t_{2g})^6(e_g)^3$, while the only excited state is ${}^2T_{2g}(t_{2g})^5(e_g)^4$ [109]. The inversion of the level order leads to the important property of the 2E_g level, which is highly susceptible to a Jahn - Teller configurational instability [110] that removes the degeneracy of the ground state. Therefore octahedral Cu^{2+} ions tend to suffer from a tetragonal distortion and the tetragonal phase copper ferrite is the only one stable at room temperature. The transformation from the tetragonal to cubic phase occurs at the temperature of 350 °C [111]. Thus, by a special post-deposition treatment the cubic phase CuFe_2O_4 thin films can be prepared [112]. The treatment consists of an annealing procedure at high temperatures and subsequent quenching in liquid nitrogen.

There have been several attempts to assign spectroscopic features observed either in magneto - optical Kerr spectra or in the corresponding spectra of the off-diagonal elements of the dielectric tensor, ε_2 , of various ferrite compounds to electron transitions in the material. However, owing to the complex electronic structure of transition metal oxides, a confusing variety of interpretations has been published due to different assignments of observed transitions. Until the report of Fontijn *et al.* on the optical and magneto-optical properties of Fe_3O_4 [34], transitions in infrared and visible region were usually described as crystal field transitions of iron ions on tetrahedral sites [113], $3d^n \rightarrow 3d^{n-1} 4s$ orbital promotion processes [114], or $2p \rightarrow 3d$ charge transfer transitions between O^{2-} and Fe^{3+} [115]. Fontijn pointed out that Fe_3O_4 exhibits a relatively strong Kerr effect in the visible region and absorption peaks with an oscillator strength of about 10^{-3} [116]. Therefore the interpretations written above, which are based on transitions either spin or parity forbidden, can not describe the reality since the oscillator strength of such transitions is expected to be about $10^{-4} - 10^{-5}$ [117]. He suggested the description of optical and magneto-optical properties by intervalence charge transfer (IVCT) and intersublattice charge transfer transitions as had been proposed by Scott [118]. In both, IVCT and ISCT transitions an electron is transferred from one cation to a neighboring cation on the same or different crystallographic site. The key distinction between IVCT transitions and CF transitions is that the former involves two cations while the latter is a single ion transition. As a result, the parity selection rule is relaxed for IVCT transition [118]. Therefore a higher oscillator strength is expected for IVCT transition than for the crystal field and orbital promotion transitions. More information about the phenomenon of IVCT and ISCT transitions can be found in original works of Scott [118] and Fontijn [119].

In this chapter, we present a systematical attempt to investigate the electronic structure of copper ferrites using the experimental techniques of spectroscopic ellipsometry and magneto-optical spectroscopy. Coherently with the results presented on various types of ferrite compounds up to now, we carefully describe all optical transitions revealed by experiment. More-

7.2. SAMPLE DEPOSITION

over, we discuss an influence of the structural change of CuFe_2O_4 on magneto-optical properties.

7.2 Sample deposition

Investigated samples of copper ferrite thin films were prepared in collaboration with Indian Institute of Technology, Bombay, India and Laboratoire de Magnetisme et d'Optique, CNRS, Versailles, France by RF sputtering method using a Leybold Z400 sputtering unit. The 75 mm tetragonal copper ferrite target used in the deposition was prepared by conventional ceramic technique. The films were deposited onto 10×10 mm fused quartz substrates. The base pressure in evacuated deposition chamber was $6 \cdot 10^{-7}$ mbar, while during the deposition a gas mixture of oxygen and argon was kept at the total pressure of $6 \cdot 10^{-3}$ mbar to produce stable plasma. The oxygen to argon ratio was maintained at 15%. The rf power was set to 50 and 200 W at 13.6 MHz. The substrates were neither heated nor cooled during sputtering. After the deposition, samples were usually annealed at 850 °C for two hours and then furnace - cooled (slow cooled (SC) samples) or quenched in liquid nitrogen. A set of samples investigated in our study consists of

- Sample B3: rf power: 50 W; annealed at 600 °C; quenched in liquid nitrogen; cubic structure
- Sample C3: rf power: 50 W; annealed at 850 °C; quenched in liquid nitrogen; cubic structure
- Sample D3: rf power: 50 W; as deposited
- Sample SC50: rf power: 50 W; annealed at 850 °C; slowly cooled; tetragonal structure
- Sample SC200: rf power 200 W; annealed at 850 °C; slowly cooled; tetragonal structure

After the deposition, crystallographic structure and magnetic properties of deposited films were studied by Philips PW 1729 X-ray diffractometer (XRD) and vibrating sample magnetometer [111]. XRD studies revealed peaks typical for cubic structure ($c/a = 1$) in the case of quenched samples, while slowly cooled samples appeared to be tetragonal with ratio $c/a \sim 1.05$. This is consistent with the knowledge that the copper ferrite can transform from the tetragonal to cubic phase only at temperatures higher than 350 °C. Moreover, XRD measurements showed all samples nano-crystalline. Magnetometer measurements showed the highest saturation magnetization M_S for quenched samples and lowest for as deposited films [111]. The increase in M_S for quenched samples is the consequence of their transformation from tetragonal to cubic

Sample	Thickness [nm]	RF power [W]	$4\pi M_S$ [G]	T_G [$^{\circ}\text{C}$]	Structure
B3	-	50	-	600	Cubic
C3	112	50	2300	850	Cubic
D3	90	50	750	-	As deposited
SC50	280	50	1500	850	Tetragonal
SC200	230	200	1600	850	Tetragonal

Table 7.1: Basic parameters of the set of CuFe_2O_4 samples. T_G denotes annealing temperature.

structure. In cubic copper ferrite, migration of cupric ions to tetrahedral site causes an increase in the magnetization. Reduced magnetic moment of the as deposited sample is caused by low grain size and large grain boundary volume [112]. The parameters of investigated samples are summarized in Tab. 7.1.

7.3 Spectroscopic ellipsometry

Similarly to the previous chapter, the four-zone null ellipsometer was employed to obtain the spectral dependences of ellipsometric parameters Ψ and Δ of the quenched sample C3 in the spectral range from 1.5 to 5.4 eV. To increase the accuracy of measured data processing, the spectra were recorded for three angles of incident light at 65° , 70° and 75° . Because the fused quartz substrate was both side polished, incoherent backreflections from the backside of the substrate contributed to the measured signal and complicated the optical characterization. Therefore a liquid solution procedure (LSP) [120] was applied to avoid the backreflections. We put a small amount of wadding paper infused by a mixture of glycerin and water, optically matched to the quartz, at the bottom of the substrate. The diagonal permittivity spectra were parametrized by the sum of four damped Lorentz oscillators similarly as for LSMO samples (Eq. (5.16)) and the least square method was employed to adjust the transition energy E_n , strength A_n and broadening Γ_n for each oscillator along with the film thickness t .

The experimental values of Ψ and Δ are shown in Fig. 7.2. The computed spectral dependence of the diagonal part of the dielectric tensor ε_{xx} is displayed in Fig. 7.3. The spectral dependence of ε_{xx} presented in this work is similar in shape to dependences reported on Fe_3O_4 [34], CoFe_2O_4 [121] and MgFe_2O_4 [114]. This indicates similar electron transitions contributing to optical properties of CuFe_2O_4 material.

The theoretical fit of experimental data revealed four optically active transitions in this material centered near energies 2.4, 3.1, 4.8 and 13.2 eV. The film thickness was evaluated to 112 nm.

7.3. SPECTROSCOPIC ELLIPSOMETRY

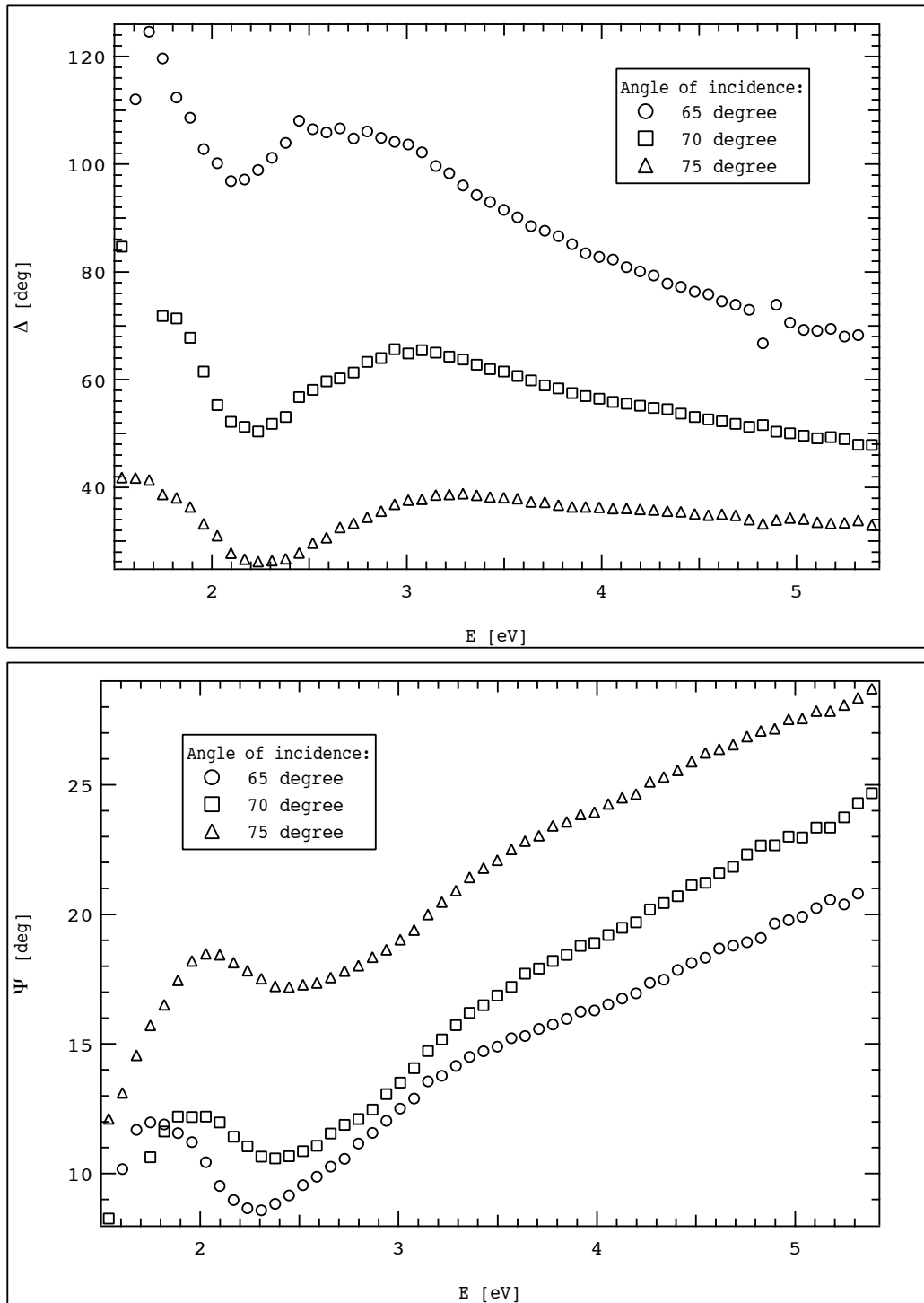


Figure 7.2: Experimental values of Ψ and Δ for quenched CuFe_2O_4 thin film (sample C3, $t=112$ nm) obtained by ellipsometric measurements at three different angles of incident light.

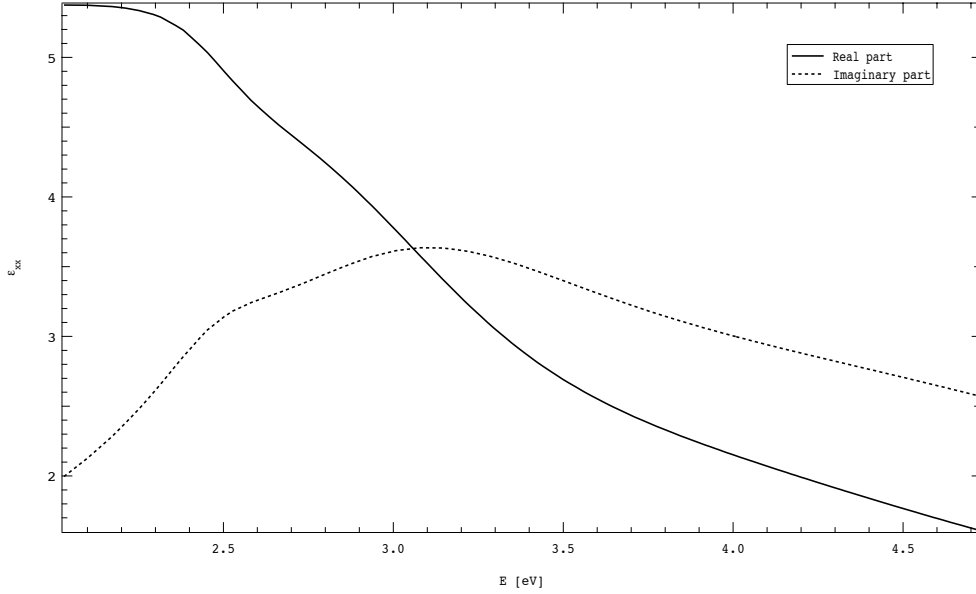


Figure 7.3: The real and imaginary part of the diagonal element ε_{xx} of the dielectric tensor for quenched CuFe_2O_4 thin film (sample C3, $t=112$ nm).

The first three transitions were also observed at similar energies in experimental spectra of the off-diagonal element of the dielectric tensor. The differences in energies are very small and are within the errors of both data. We postpone the discussion of these transitions to the next section and focus here only on the transition centered near 13.2 eV.

The separation energy of about 5-10 eV between the valence band of oxygen $2p$ orbitals and $4s$ orbital of transition metal ions has been reported in various transition metal oxides [122, 6]. Strong absorption above 8 eV has been reported by Zhang *et al.* [114] in optical reflection measurements on Mg and Li ferrites. Alvarado *et al.* [123] reported the same spectral behavior in photoelectron-spin-polarization measurements with photon energies up to 11 eV on Fe_3O_4 . Therefore the oscillator near 13.2 eV obtained from the fit of experimental Ψ and Δ data is surely related to the electric-dipole-allowed transition between O^{2-} $2p$ valence band and Fe^{3+} $4s$ conduction band.

Because it is necessary to know the film thickness to analyze magneto-optical data and derive the spectra of off-diagonal elements of the dielectric tensor, we used the thickness of the sample C3 obtained from ellipsometric measurements in further calculations. Thicknesses of remaining samples were taken from [124].

7.4 Magneto-optical spectroscopy

7.4.1 Polar geometry

Experimental polar Kerr spectra were measured in the photon energy range from 1.3 to 4.7 eV at nearly normal light incidence. Samples were mounted on the water cooled pole piece of electromagnet similarly to the case of LSMO thin films. Because the fused quartz substrates were both side polished, a small piece of black paper was inserted between the sample and pole piece of electromagnet to minimize the back reflections from the backside of the substrate. The magnetic field applied during the measurement was as high as 470 mT, which was satisfying for the film saturation.

Fig. 7.4 shows the experimental results for all investigated samples. A low noise level with respect to relatively small amplitude of measured effect reflects very high sensitivity of measurement system. Measured polar Kerr spectra of all samples exhibit similar spectral behavior with only minor differences. A contribution of the propagation across the film resulting in the interference is clearly visible in photon energy range below 2.4 eV. Besides, the polar Kerr rotation spectrum is dominated by two visible peaks with opposite signs near 3.1 and 4.2 eV. On the other hand, polar Kerr ellipticity spectra show a positive peaks near 3.5 and 3.8 eV. The amplitudes of polar Kerr effect differ with the sample. This is due to the different internal magnetization of each film (see Tab. 7.1). Measured spectra are similar in shape with those published by Kim *et al.* [125] on samples prepared by sol-gel method. However in that paper a different convention was used. Therefore to compare the results, one has to compare our rotation to their ellipticity and our ellipticity to their rotation multiplied by the factor -1. There are some discrepancies in their results above 4.5 eV. They observed a spectroscopic structure in the polar Kerr rotation spectrum near 4.3 and 4.7 eV. However the Kerr ellipticity spectrum should exhibit also some spectroscopic structure since it is related to the polar Kerr rotation spectrum through Kramers - Kronig relations.

Comparing our polar Kerr rotation spectra of slowly cooled and quenched samples, the positive peak near 3.1 eV is more visible for slow cooled samples than for quenched samples. In the case of the as deposited sample, the peak vanishes completely.

To provide more detailed analysis of measured polar Kerr effect, we computed the spectra of the off-diagonal element of the dielectric tensor, ε_2 , for all samples except the sample B3. In the calculation, we considered a model of thin layer on semi-infinite substrate. As optical constants for all samples we used the spectrum of ε_{xx} obtained by ellipsometric measurements on the sample C3 (shown in Fig. 7.3). Calculated results in the photon energy region from 2.2 to 4.8 eV are displayed in Fig. 7.5.

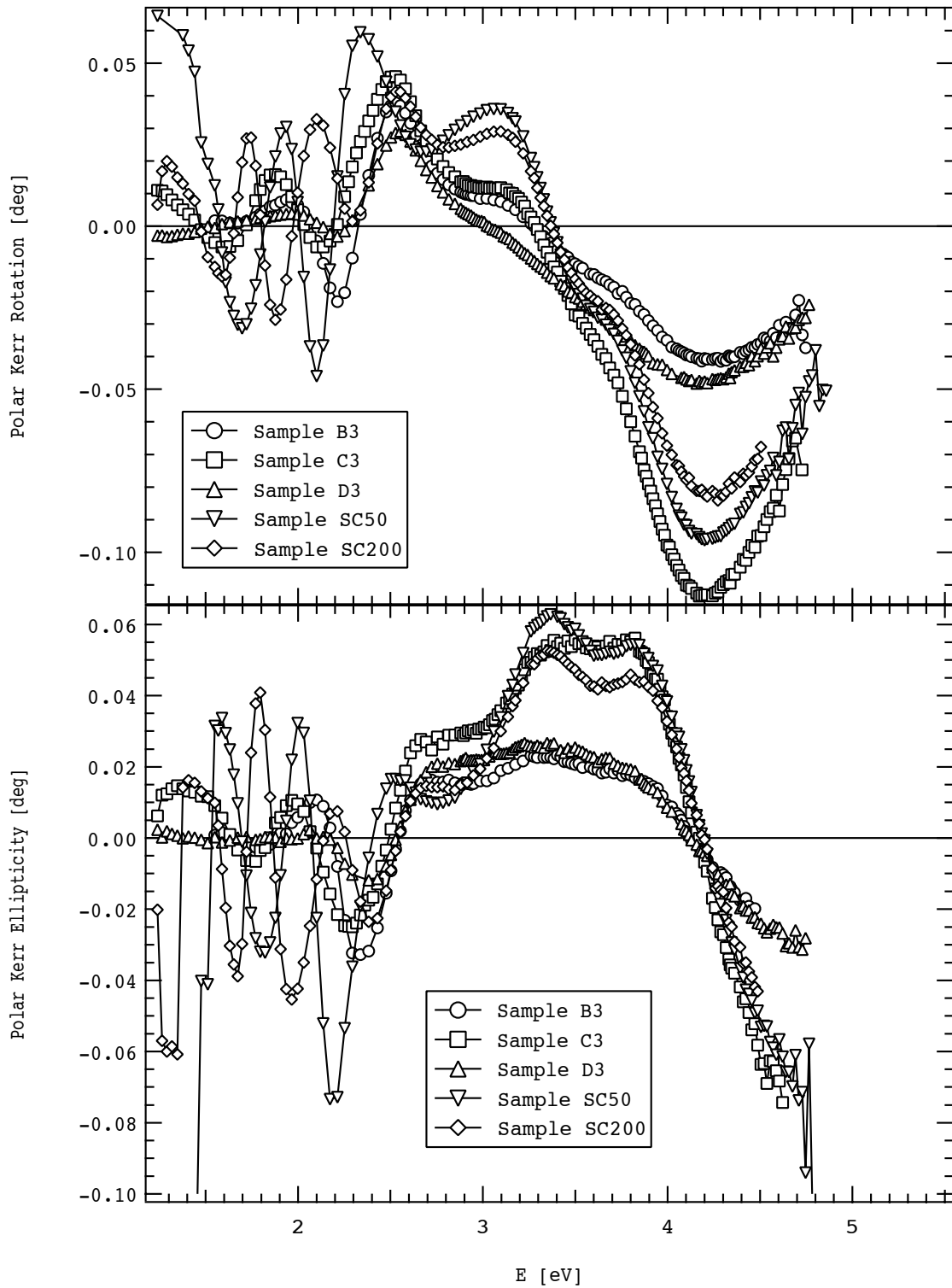


Figure 7.4: Experimental polar Kerr spectra of CuFe_2O_4 thin films measured at nearly normal incidence.

7.4. MAGNETO-OPTICAL SPECTROSCOPY

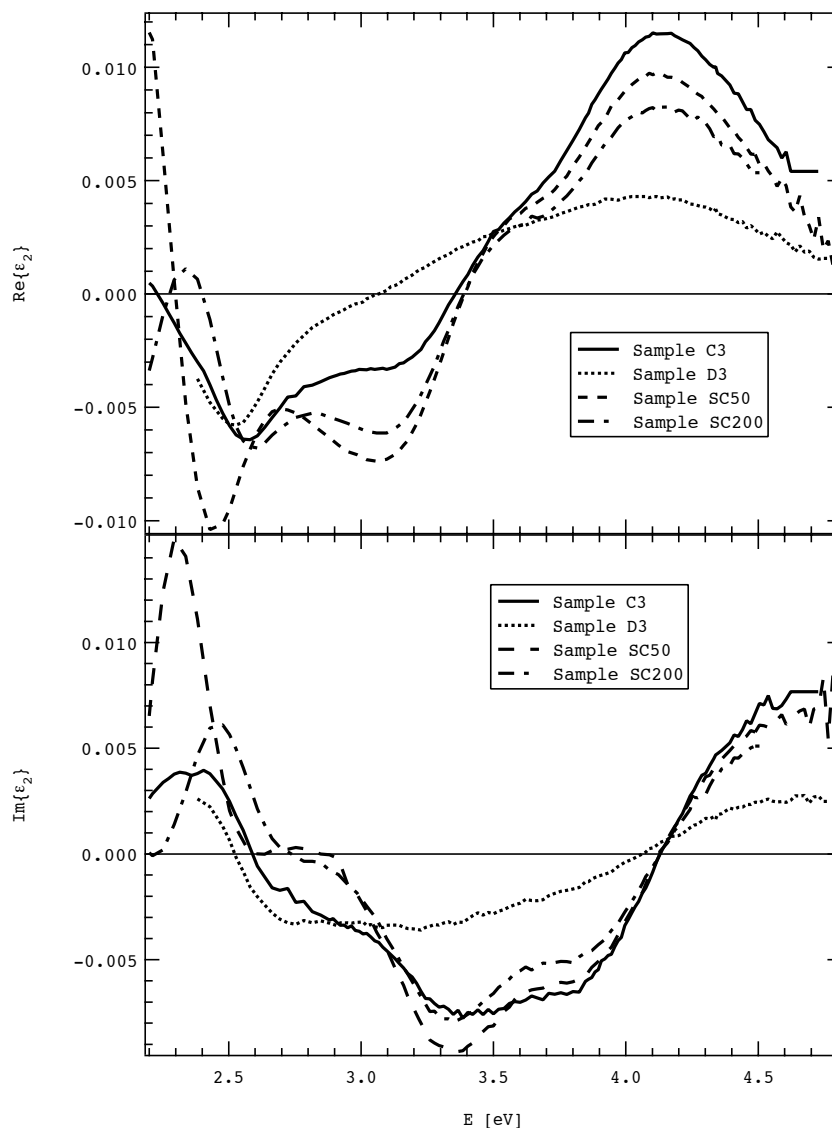


Figure 7.5: Experimental off-diagonal elements of the dielectric tensor of CuFe_2O_4 thin films.

All samples exhibit similar spectral behavior of ε_2 with only minor differences. The most departing spectrum appears to be that of the sample D3. This is, however, comprehensible owing to the similar differences in XRD and magnetic measurements. Nevertheless, all spectra of the real part of ε_2 exhibit negative peaks near 2.6 and 3.1 eV, and broad positive peak near 4.2 eV. On the other hand, spectra of the imaginary part of ε_2 are dominated by two positive peaks near 2.5 and 4.7 eV, and negative spectroscopic structure consisted of two peaks near 3.3 and 3.9 eV. Such spectral shapes are similar to those published in [115] on MgFe_2O_4 bulk samples as well as with those published on $\text{Li}_{0.5}\text{Fe}_{2.5}\text{O}_4$ single crystals [114, 126, 127]. Nevertheless, in both cases they observed a sharp peak near the energy of 3.5 eV in the real part

spectra of ε_2 which is not so clearly visible in the results presented here. Martens *et al.* [121] published experimental results on Co ferrite, but their results differ from the results presented here. It should be also noted, that they used the sign convention in which the imaginary part is multiplied by the factor -1.

Deeper analysis of the off-diagonal elements derived from the experiment showed five transitions near 2.4, 2.6, 3.3, 3.9 and 4.6 eV. All these transitions are of paramagnetic shape. This is contrary to work of Fontijn *et al.* [128, 119] who reported almost all transitions in various ferrite compounds as diamagnetic types. However we don't agree with their conclusions, since they ignored a spectral dependence of the imaginary part of ε_2 . Following Kahn *et al.* [28], the imaginary part of ε_2 in diamagnetic transition exhibits a maximum on the left side from the resonant frequency ω_0 and the minimum on the right side (see Fig. 3.1). This is in contrary with the results presented by Fontijn *et al.*. We suspect that they also exchanged the real and imaginary parts of ε_2 for Co ferrite.

Four transitions can be easily seen in the imaginary part of ε_2 in Fig. 7.5. The fifth transition, situated near 2.6 eV, is not clearly visible. The spectral dependence of ε_2 derived from the experimental Kerr effect was fitted by a summation of five paramagnetic shapes using Eq. (3.43). The results of these fits are shown in Figs. 7.6 and 7.7, while the fitting parameters are summarized in Tab. 7.2. From Figs. 7.6 and 7.7 excellent agreement between the theoretical fit and experimental data is clearly visible. Comparing the resulting spectra of ε_2 with results on MgFe_2O_4 [115], NiFe_2O_4 [128] or $\text{Li}_{0.5}\text{Fe}_{2.4}\text{O}_4$ [114, 126, 127], one can estimate which transitions are coming from iron ions and which are coming from copper ions.

Now, we focus on the first transition near 2.4 eV. The spectroscopic structure corresponding to this transition can be also observed at similar energies in other ferrite compounds [115, 114] even in the parent compound Fe_3O_4 [129]. This indicates that the transition involves Fe^{3+} electrons only. Thus, according to electron energy levels in CuFe_2O_4 , we can assign this transition to an ISCT transition $(\text{Fe}^{3+})t_2 \rightarrow [\text{Fe}^{3+}]t_{2g}$ between tetrahedral and octahedral Fe^{3+} ions [34]. This is consistent with Kim *et al.* [125] who observed the same transition near energy 2.5 eV in the spectrum of polar Kerr rotation of CuFe_2O_4 . The second transition near 2.6 ~ 2.7 eV is not clearly visible in the spectra of ε_2 due to smaller oscillator strength and width, compared to neighboring transitions. Most visible is this transition in the sample D3. Similarly to the previous case, MgFe_2O_4 and $\text{Li}_{0.5}\text{Fe}_{2.4}\text{O}_4$ also exhibit spectroscopic structure around these energies. Clearly visible is the peak in ε_2 spectrum of $\text{Li}_{0.5}\text{Fe}_{2.4}\text{O}_4$ reported by Zhang [114]. Since there is no change with different substitution, only Fe^{3+} ion should be involved. Therefore we assign this transition to an ISCT transition, $[Fe^{3+}]e_g \rightarrow (Fe^{3+})e$, between octahedral and tetrahedral Fe^{3+} ions.

Let's now discuss two peaks centered near 3.3 and 3.9 eV. Such pair of spectroscopic struc-

7.4. MAGNETO-OPTICAL SPECTROSCOPY

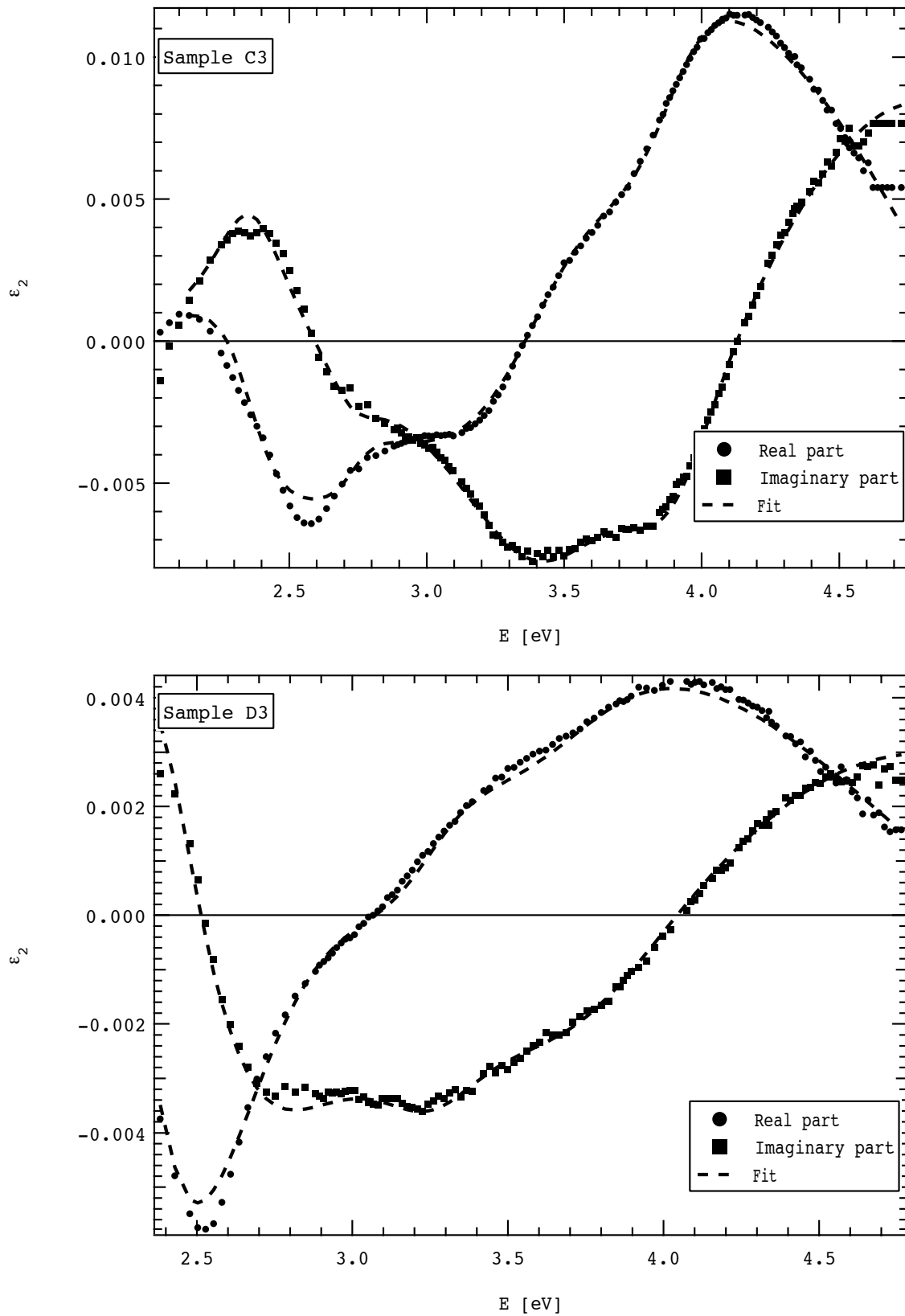


Figure 7.6: Comparison of ϵ_2 spectra derived from experiment (dots) with theoretical fit for quenched samples C and D.

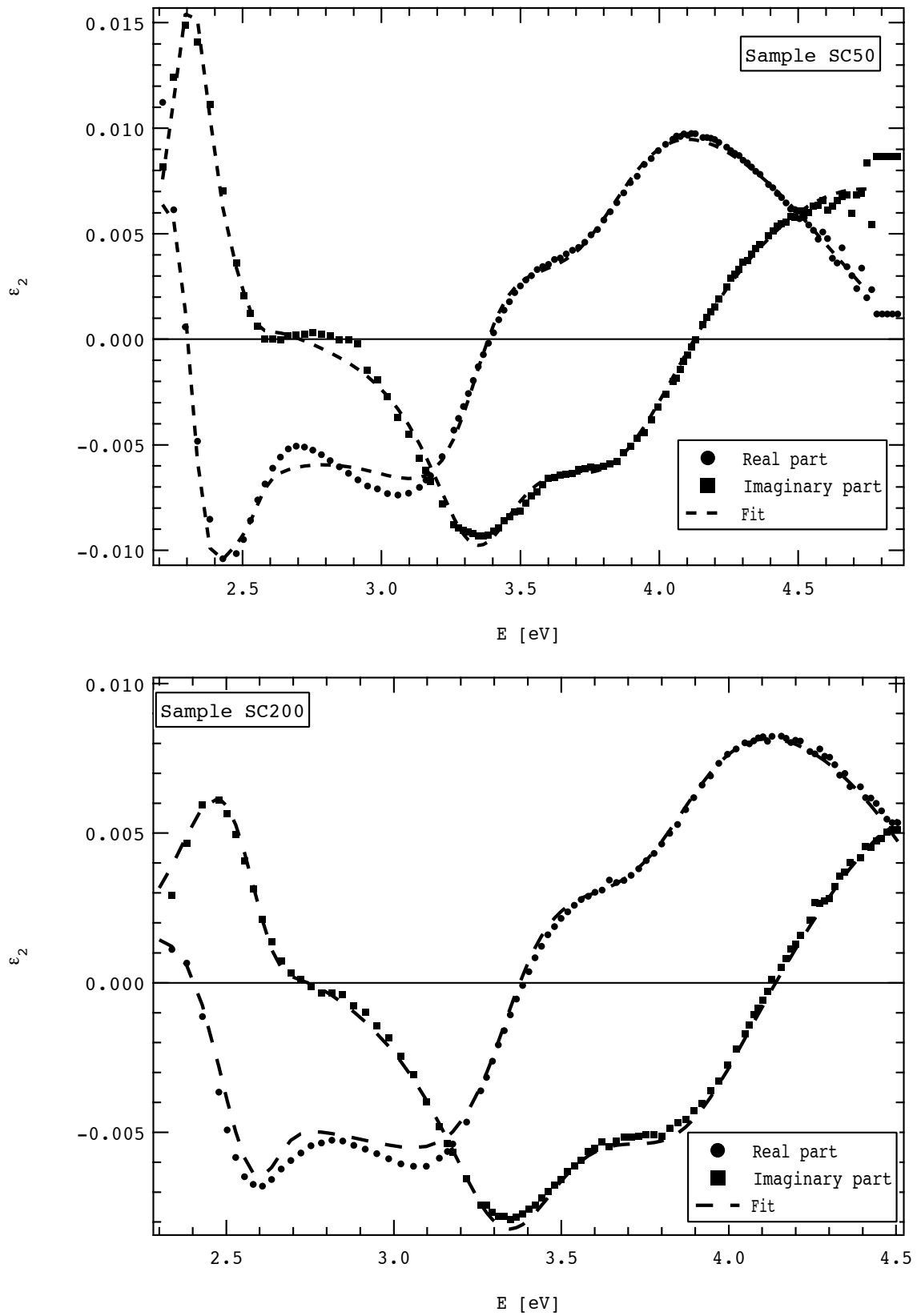


Figure 7.7: Comparison of ϵ_2 spectra derived from experiment (dots) with theoretical fit for slowly cooled samples SC50 and SC200.

7.4. MAGNETO-OPTICAL SPECTROSCOPY

Sample	C3	D3	SC50	SC200
$(\varepsilon_2'')_{max}$	0.0053	0.0072	0.0163	0.0075
ω_0 [eV]	2.3573	2.3528	2.3143	2.4434
Γ [eV]	0.1858	0.2097	0.0961	0.1840
Transition I	ISCT $(Fe^{3+})t_2 \rightarrow [Fe^{3+}]t_{2g}$			
$(\varepsilon_2'')_{max}$	-0.0017	-0.0052	-0.0012	-0.0026
ω_0 [eV]	2.7320	2.6571	2.5541	2.6412
Γ [eV]	0.1381	0.4359	0.0719	0.1086
Transition II	ISCT $[Fe^{3+}]e_g \rightarrow (Fe^{3+})e$			
$(\varepsilon_2'')_{max}$	-0.0087	-0.0019	-0.0092	-0.0079
ω_0 [eV]	3.3426	3.2492	3.3357	3.3308
Γ [eV]	0.4320	0.2562	0.2245	0.2536
Transition III	ISCT $[Fe^{3+}]e_g \rightarrow (Fe^{3+})t_2 \uparrow$			
$(\varepsilon_2'')_{max}$	-0.0063	-0.0029	-0.0081	-0.0061
ω_0 [eV]	3.8870	3.7223	3.8389	3.8624
Γ [eV]	0.2705	0.4891	0.3515	0.3308
Transition IV	ISCT $(Fe^{3+})t_2 \rightarrow [Fe^{3+}]e_g \downarrow$			
$(\varepsilon_2'')_{max}$	0.0099	0.0038	0.0087	0.0073
ω_0 [eV]	4.7396	4.7142	4.6622	4.4976
Γ [eV]	0.7249	0.9827	0.7255	0.5301
Transition V	IVCT $[Cu^{2+}]e_g \rightarrow [Fe^{3+}]t_{2g}$			

Table 7.2: The magneto-optically active transitions in $CuFe_2O_4$ thin films between 2.0 and 5.0 eV. Listed are transition energy, ω_0 , linewidth, Γ_0 , intensity, $(\varepsilon_2'')_{max}$, and transition assignment. (Note that the parenthesis denote tetrahedral coordination and square brackets octahedral coordination.)

tures in ε_2 spectra was observed across all ferrite compounds [114, 129, 34] including $CuFe_2O_4$ [125]. In Kim's report [125] on $CuFe_2O_4$, the former transition is shifted to higher energy side of about 0.2 eV. However, it is appropriate to note that their conclusions are coming from the approximative analysis of the Kerr rotation spectra, while the analysis based on the permittivity tensor presented in this work is more rigorous. Consistently with previous findings we assigned discussed peaks to ISCT transitions between octahedral and tetrahedral sites, $[Fe^{3+}]e_g \rightarrow (Fe^{3+})t_2 \uparrow$ and $(Fe^{3+})t_2 \rightarrow [Fe^{3+}]e_g \downarrow$, respectively. The 3.3 eV structure is attributed to an ISCT transition in the majority spin bands while the 3.9 eV one to an ISCT

transition in the minority spin bands.

The last structure to discuss is situated near 4.4 ~ 4.7 eV. Compared to all previous cases, this band energy varies with the sample. This is a consequence of the inaccurate determination of the peak position due to its relatively large line-width and the end of the measured region. Moreover, in the UV region the Kerr measurement suffers from higher noise level due to the increased role of light scattering. This noise is also reflected in the experimental ε_2 spectra and negatively influence the accuracy of the fit in this energy region. There is no comparable transition visible in ε_2 spectra of $\text{Li}_{0.5}\text{Fe}_{2.4}\text{O}_4$ [114], NiFe_2O_4 [128] and CoFe_2O_4 [121]. This raise the possibility of the contribution of Cu^{2+} ions to this transition. IVCT transitions between divalent substituted ion and trivalent iron ion, both situated at octahedral sites, were observed in Co and Ni ferrites: $[\text{Co}^{2+}]t_{2g} \rightarrow [\text{Fe}^{3+}]t_{2g}$ at about 2.2 eV and $[\text{Ni}^{2+}]t_{2g} \rightarrow [\text{Fe}^{3+}]t_{2g}$ at about 3.1 eV. Owing to the larger binding energies of more localized 3d electrons of Cu^{2+} compared to Co^{2+} and Ni^{2+} , a similar transition is expected at higher energies. Considering the inversion of the electron level order for Cu^{2+} ions, we finally assign the last observed spectroscopic structure to an IVCT $[\text{Cu}^{2+}]e_g \rightarrow [\text{Fe}^{3+}]t_{2g}$ transition. This is consistent with Kim *et al.* [125], who observed spectroscopic structures near 4.3 and 4.7 eV in the Kerr rotation spectrum of CuFe_2O_4 . However, their explanation of the splitting seems to be less realistic due to the reasons mentioned above.

Assignments of all transitions revealed by fitting the ε_2 spectra are summarized in Tab. 7.2. The spectra of imaginary part of ε_2 for each fitted transition are shown in Fig. 7.8. From both, one can see a slight variation of the transition energy with the sample. This is due to the fit error, which is ~ 1%, and also due to the fact that we used optical constants of the sample C3 in all fits. The optical properties of other samples can slightly differ from those of the sample C3. Comparing the results on slowly cooled samples, one can find considerably higher amplitude $(\varepsilon_2'')_{max}$ of transitions (except Transition II) in the sample SC50 than in the sample SC200. This indicates a decomposition of the target material at higher sputtering power, which results in the decrease of exchange interactions and lower number of active absorbing centers per unit volume. This may cause the decrease of the transition amplitude. From Fig. 7.8 follows that the transitions in the quenched sample are broader compared to those in slowly cooled samples. This might have connection with the migration of cupric ions to tetrahedral site. Because the center of the symmetry is missing at tetrahedral sites, electron orbitals are more opened and a covalent bonding is increased. This may broaden the transition line shapes. However, more detailed structural and optical studies are necessary to confirm this hypothesis.

Finally, we make a comment on the crystal field (CF) splitting energy Δ_{CF} of tetrahedral and octahedral Fe^{3+} ions in CuFe_2O_4 thin films. As follows from Tab. 7.2, the crystal field energy splitting for the octahedral Fe^{3+} iron Δ_{CF}^O is about 1.5 eV, while in the case of tetrahedral

7.4. MAGNETO-OPTICAL SPECTROSCOPY

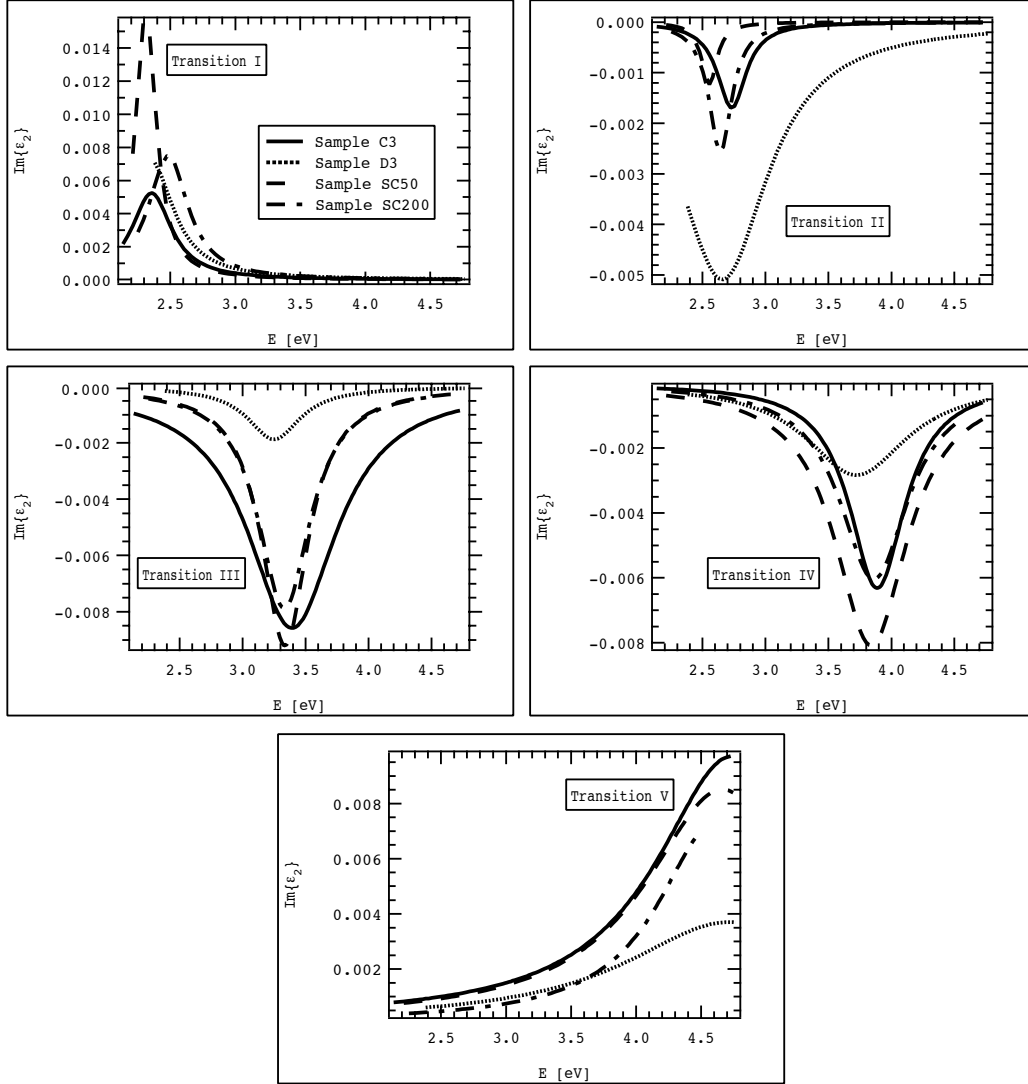


Figure 7.8: The imaginary parts of all fitted paramagnetic transitions in CuFe_2O_4 thin films.

Fe^{3+} iron Δ_{CF}^T is about 0.7 eV. Camphausen *et al.* [122] reported that octahedrally coordinated Fe^{3+} ions give $\Delta_{CF}^O = 1.7 - 2.0$ eV, while the tetrahedrally coordinated Fe^{3+} ions give $\Delta_{CF}^T = 0.86 - 1.17$ eV. Kim *et al.* reported the value of $\Delta_{CF}^O = 1.4$ eV. Comparing our results with published studies we found a very good agreement. This also confirmed the correctness of the assignment of the spectroscopic structures observed in ϵ_2 spectra to particular transitions.

7.4.2 Longitudinal geometry

Longitudinal Kerr rotation spectra of quenched and as-deposited samples were measured at the angle of incidence 72° . The optical sequence was the same as in the polar geometry. The sample was kept at ambient temperature approximately 295 K and applied magnetic field was as high

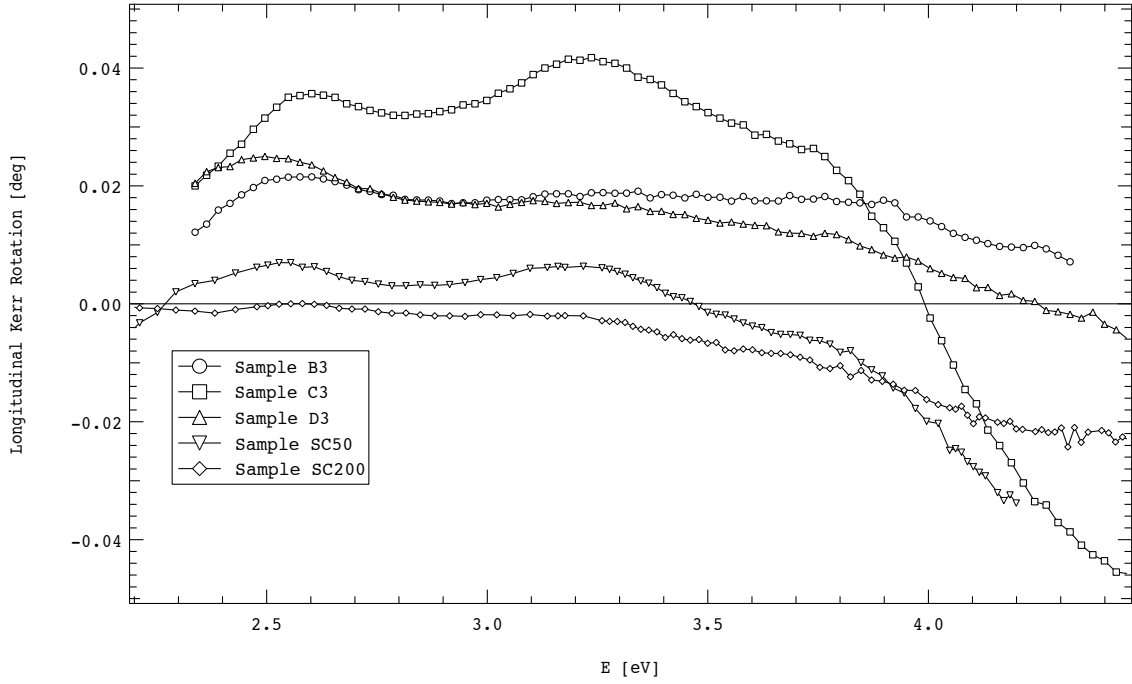


Figure 7.9: Room temperature longitudinal Kerr rotations of CuFe_2O_4 measured as both $Re\{r_{ps}/r_{pp}\}$ ratio for quenched samples and $Re\{r_{ps}/r_{ss}\}$ ratio measured for slowly cooled samples. The angle of light incidence was 72° .

as 0.1 T which ensured the sample saturation. Similarly to the case of LSMO samples, the effect of the stray magnetic field on the optical elements was considered in the data processing. The incident light polarizations were s -polarization for quenched and as-deposited samples (measuring $\frac{r_{ps}}{r_{pp}}$ ratio), and p -polarization (measuring $\frac{r_{ps}}{r_{ss}}$ ratio) for slowly cooled samples. Experimental data are shown in Fig. 7.9. All presented spectra are similar in shape apart from the sample and incident light polarization. The difference seems to be only in amplitudes. All spectra exhibit two positive peaks near energies of 2.6 and 3.2 eV and are monotonically decreasing with increasing photon energy.

Theoretical calculation of longitudinal Kerr rotation was performed utilizing the complete knowledge of the dielectric tensor of CuFe_2O_4 layers. Resulting spectra are shown in Fig. 7.10. Comparing these results with experimental data, one can see a very good agreement in the case of the sample C3. However, slowly cooled and as-deposited samples give less satisfactory agreement. The model spectra of these samples have similar spectral shape with two main positive peaks, but their amplitudes are higher compared to the experimental results. This is understandable if we will consider the fact that these samples are nano-crystalline with high inhomogeneity. Owing to the high angle of incidence, the area of the optical spot on the sample

7.5. CONCLUSION

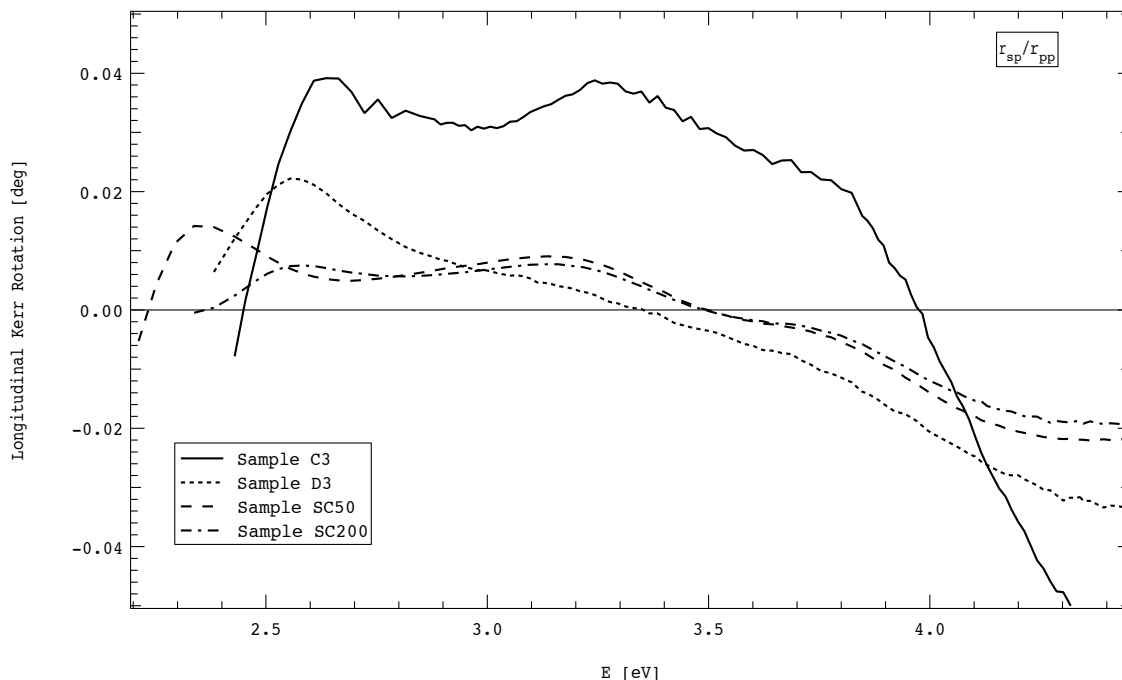


Figure 7.10: Theoretically calculated longitudinal Kerr rotation for quenched samples $Re\{r_{ps}/r_{pp}\}$ and slowly cooled samples $Re\{r_{ps}/r_{ss}\}$. The angle of light incidence was considered 72° .

increased. Therefore a parasitic effects as the light scattering on the surface of the film as well as the multiple internal light scattering (well known in semiconductor powders [130]) play an important role and lead to decrease of the measured signal which results in the decrease of the measured Kerr effect.

7.5 Conclusion

In this section, the results of ellipsometric and magneto-optical measurements on CuFe_2O_4 thin films with cubic and tetragonal crystalline structures were presented. The combination of spectroscopic ellipsometry and magneto-optical spectroscopy showed itself as an effective method to investigate the electronic structure of these inverse spinels. Utilization of both methods detected six electron transitions in a broad spectral region near energies 2.4, 2.7, 3.3, 3.9, 4.7, and 13.2 eV. First four transitions were, consistently with literature, assigned to ISCT transitions between Fe^{3+} ions placed at octahedral and tetrahedral sites. The fifth transition was assigned to an IVCT transition between Cu^{2+} and Fe^{3+} ions. Finally the last transition was discussed as an electron transfer between O 2p valence band and Fe 4s conduction band. This assignment was

CHAPTER 7. EXPERIMENTAL RESULTS ON CuFe_2O_4 THIN FILMS

confirmed by the derivation of the crystal field splitting energy for both octahedral and tetrahedral iron ions respectively. Obtained energies are in reasonable agreement with theoretically predicted values as well as with experimental results obtained on similar compounds.

8 Experimental results on Bi:YIG thin films

8.1 Material introduction

Yttrium iron garnets (YIG) were historically one of the first magnetic oxides intensively studied for their potential applications in sensors, displays, magnetic storage media (bubble memories), modulators and switches, etc. [117, 131]. This interest has arisen by the report of anomalous Faraday rotation induced by Bi^{3+} ions in Bi,Ca:YIG compounds published by Buhrer [132]. Later, a similar magneto-optical response was observed also in Bi substituted YIG [30, 133]. By the time, these compounds became also attractive due to their potential application in devices for magneto-optical sensing of the magnetic field distribution on the surface of magnetic nanostructures. Such device requires a small probe that will not modify the magnetic field distribution generated in magnetic nanostructures. Recently, the magneto-optical response of garnet compounds was enhanced by their incorporation in magneto-phonic crystals [134, 135]. These are promising for various device applications as spatial light modulators, optical isolators, etc. Processing of Bi:YIG magneto-phonic crystals, however, requires small thicknesses of Bi:YIG layers to obtain the highest magneto-optical efficiency at given wavelength. This brings a new effort in deposition techniques to grow thin, stoichiometric layers with good magnetic properties.

Yttrium iron garnet is a ionic crystal, which composition is characterized by a prototype formula $\{\text{Y}_3^{3+}\}[\text{Fe}(\text{oct})_2^{3+}][\text{Fe}(\text{tet})_3^{3+}]\text{O}_{12}^{2-}$. The space group is body centered cubic O_h^{10} -Ia3d. There are eight formula units in a unit cell (shown in Fig. 8.1) of the lattice constant $a = 12.376 \text{ \AA}$ [136]. With regard to the formula unit, five iron atoms are situated in two sites. Three iron atoms are in 24(d) sites tetrahedrally surrounded by four neighbor oxygen atoms, while two iron atoms are in 16(a) sites octahedrally surrounded by six neighbor oxygen atoms. Both the octahedra and tetrahedra are slightly distorted. The strongest exchange interaction is antiferromagnetic between two neighbor iron atoms in different sites through the intervening oxygen, so there is a net magnetization parallel to the $\text{Fe}(\text{tet})$ magnetization.

The substitution of bismuth Bi^{3+} into YIG leads to the increase of magneto-optical response.

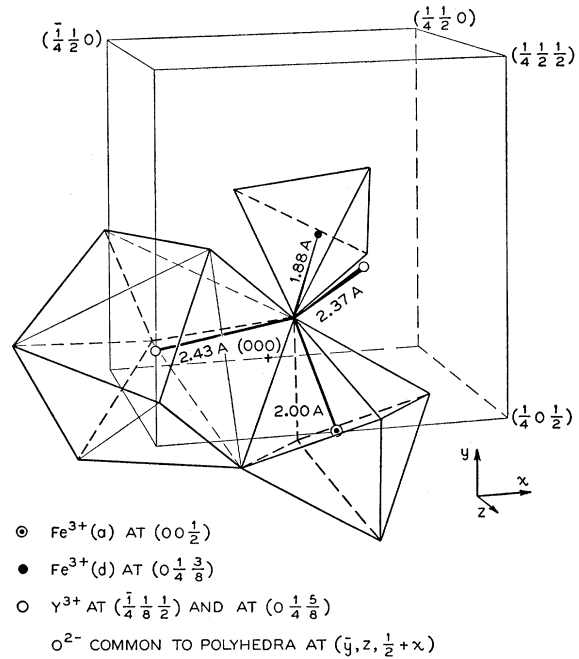


Figure 8.1: Elementary cell of the garnet structure [139].

This substitution also results in a stretch of the lattice parameter. Because the exchange interactions strongly depend on the geometry of [Fe] - O - (Fe) bonding, the increase of the lattice parameter seems to be linked to a small increase of the [Fe] - O - (Fe) angle without significant variation of the Fe-O distances [137].

More information about the crystalline structure of Bi:YIG as well its influence on magnetic properties can be found in Ref. [138]

8.2 Sample deposition

There are several methods used for the garnet film growth. First successfully applied was the liquid phase epitaxy (LPE) method [140, 141, 142]. Since this method was applied for the first time at the end of 1960's [143], it became the most widely used method to prepare garnet films. This method produces films with the least microstructure, allows good control over the film composition, and shows a high reproducibility. On the other hand, the disadvantages is a difficulty to produce films far away from the thermodynamical equilibrium. Other disadvantage is the incorporation of ions coming from materials used in deposition equipment.

Another technique, mainly used for the Bi:YIG deposition, is PLD [144, 145, 146, 147]. One of the main advantages of this technique is the stoichiometric transfer of matter from the

8.3. MAGNETO-OPTICAL SPECTROSCOPY

target to the substrate. This feature allows to grow layers with complex stoichiometries. The disadvantage of this method is the growth of low quality films with thicknesses exceeding $1\ \mu\text{m}$.

Besides these two main growth techniques, reactive ion beam sputtering [146, 148], *rf* sputtering [149], metal organic chemical vapor deposition [150], spin or dip coating gels [151] and electron cyclotron resonance sputtering [152] methods have been also employed to grow Bi:YIG films.

In this work, investigated samples were prepared in collaboration with Indian Institute of Technology, Bombay, India and Laboratoire de Magnetisme et d'Optique, CNRS, Versailles, France. Pulsed laser deposition was used as a deposition technique, while Gallium Gadolinium Garnet (GGG) (111) was used as a substrate. Details of the PLD technique are shown in the Chapter 6, thus we will mention here only the deposition conditions. To enhance the growth speed and increase the crystalline quality of deposited films, the substrates were heated to the temperature of 700°C and 800°C during the deposition. A third harmonic of Nd:YAG laser with repetition rate 10 Hz and energy density of $2.5\ \text{J}/\text{cm}^2$ was used to ablate the target. A set of three samples with different Bi content and deposition temperature was prepared as follows

- Sample B1YIGa: $\text{Bi}_1\text{Y}_2\text{Fe}_5\text{O}_{12}$ deposited at 700°C
- Sample B1YIGb: $\text{Bi}_1\text{Y}_2\text{Fe}_5\text{O}_{12}$ deposited at 800°C
- Sample B2YIG: $\text{Bi}_2\text{Y}_1\text{Fe}_5\text{O}_{12}$ deposited at 800°C

All samples were characterized by X-ray diffraction. Thicknesses of Bi:YIG films have not been determined.

8.3 Magneto-optical spectroscopy

8.3.1 Polar geometry

Polar Kerr effect was measured in the energy range between 1.8 and 5.1 eV at nearly normal light incidence. Applied magnetic field was 470 mT, which provided the saturation of the samples. Because all samples were mounted on the water cooled pole piece of electromagnet, their temperature was stabilized at 285 K. The experimental complex polar Kerr effect spectra of the samples B1YIGa and B1YIGb along with the polar Kerr rotation spectrum of the sample B2YIG are shown in Fig 8.2. A low level of noise was observed in the spectra up to 5 eV which indicates a good surface quality of investigated samples. An important contribution of the propagation across the film resulting in the interference is clearly visible below 3 eV for all samples. Except this region, polar Kerr rotation spectra are characterized by positive peak

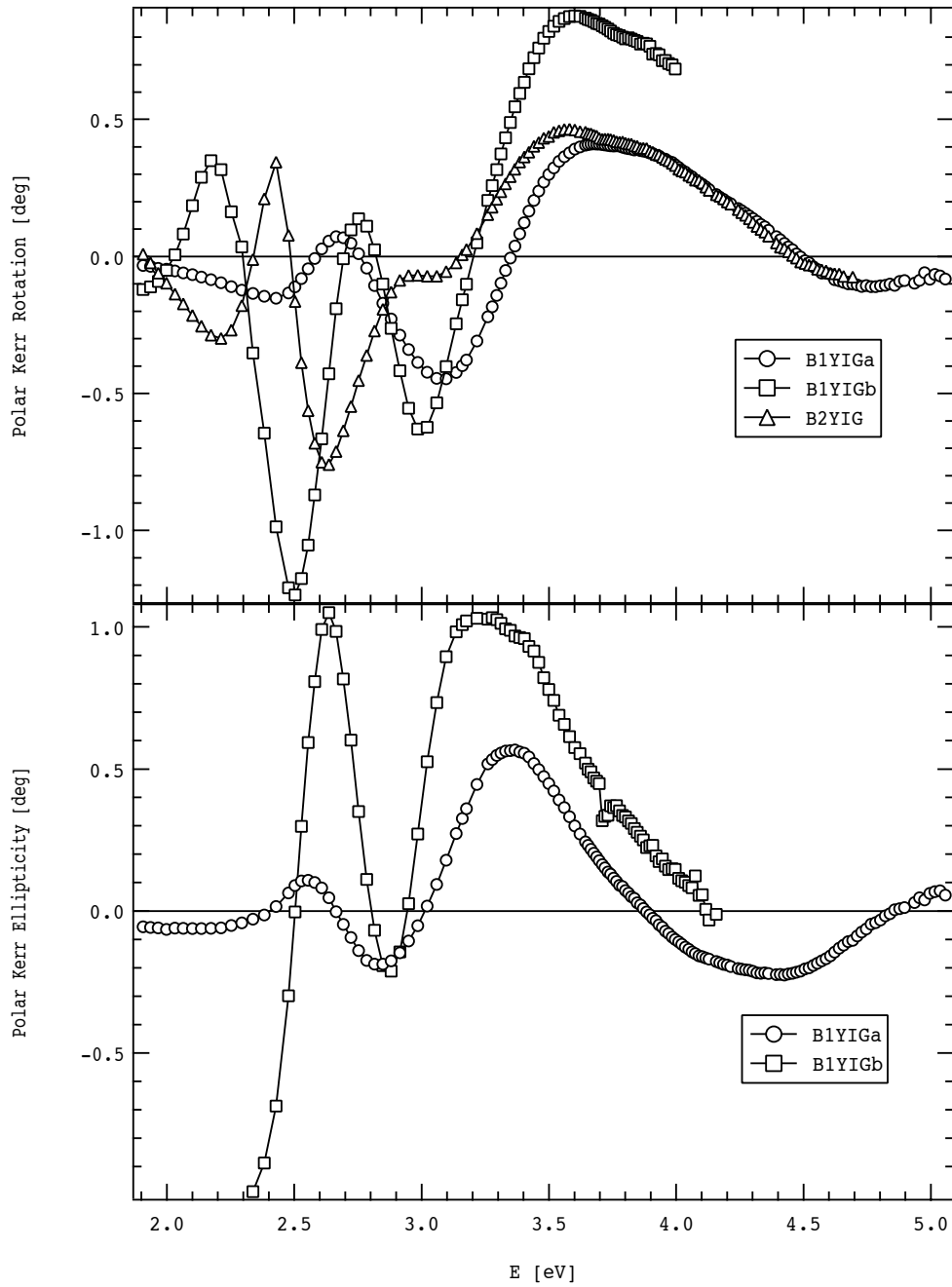


Figure 8.2: Experimental polar Kerr spectra of Bi:YIG films deposited on (111) GGG substrates measured at nearly normal incidence.

8.3. MAGNETO-OPTICAL SPECTROSCOPY

with the maximum near 3.6 eV coupled with the negative peak with the minimum near 4.7 eV. On the other hand, polar Kerr ellipticity spectra exhibits two main peaks of opposite signs near 3.4 and 4.5 eV, respectively. For all samples, the overall spectral behavior is similar and in agreement with complex polar Kerr effect spectra reported by Wittekoek [30] on polycrystalline samples. The polar Kerr spectra are also consistent with results published by Papakonstantinou on 300 nm thick polycrystalline sample of BiGa:DyIG film [153].

For deeper analysis of experimental data, theoretical spectra of polar Kerr effect have been calculated to determine the thicknesses of investigated films. Owing to the strong interference in the spectral region below 3 eV and the high penetration depth in the Bi:YIG layer, the model of a thin layer of Bi:YIG on a semi-infinite GGG substrate had to be considered instead of the simple bulk Bi:YIG model. In the calculation we used the optical and magneto-optical constants obtained by Wittekoek *et al.* on polycrystalline samples [30] along with the optical constants of GGG coming from experiments of Wood *et al.* [154]. Spectral dependences of these constants are shown in Figs. 8.3 and 8.4. To derive the thicknesses of Bi:YIG layers, theoretical spectra of polar Kerr effect were calculated with respect to positions of the interference maxima and minima in the infrared region. Calculated spectra of polar Kerr effect and corresponding experimental values for the sample B1YIGa are shown in Fig. 8.5. In this figure a satisfactory agreement between the theory and experiment is evident. The thickness of Bi:YIG layer was determined as high as $t = 73$ nm, which is notably lower than usual thickness of bismuth substituted iron garnets grown by PLD technique [137, 144, 145, 146, 147, 155]. Although the model describes the spectral behavior of experimental spectra very well, the theory predicts higher amplitudes of main spectral peaks. This is a consequence of a small layer thickness with respect to the size of one elementary cell of Bi:YIG, which is approximately 1.2 nm. A rela-

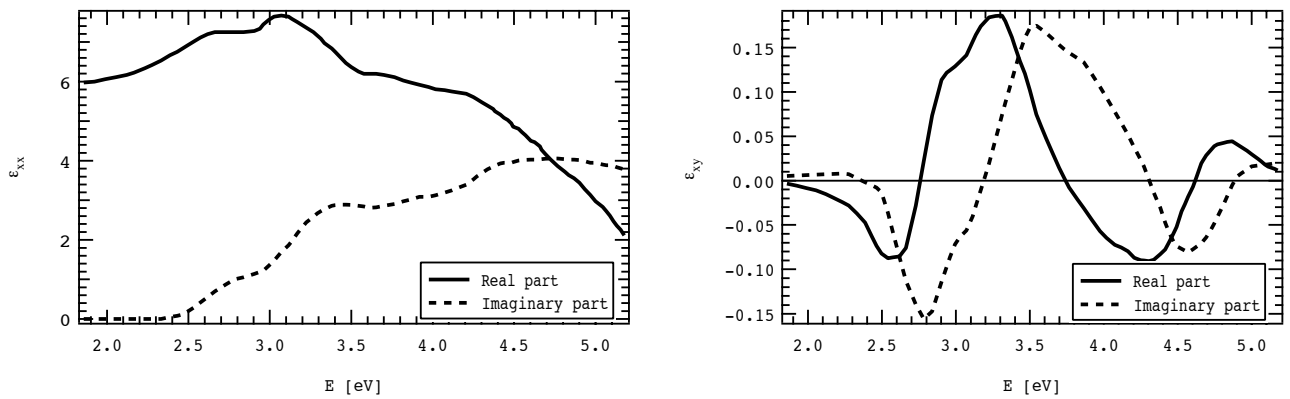


Figure 8.3: Real and imaginary part of the diagonal element ϵ_{xx} of the dielectric tensor of $Y_2Bi_1Fe_5O_{12}$ [30].

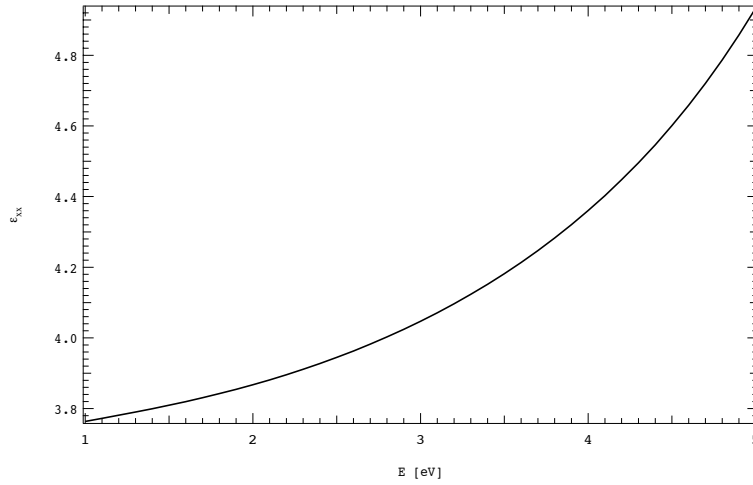


Figure 8.4: Real part of the diagonal element ε_{xx} of the dielectric tensor of GGG [154].

tively small number of elementary cell layers is therefore contained in the film. Thus the effect of the non-ideal interface between the substrate and Bi:YIG layer as well as the roughness of the film surface, when not all elementary cells contribute to the general ferrimagnetic ordering of the film due to their deformations, has an important influence on the magnetic properties and polar Kerr effect. Because a simple model of a single layer with ideal interfaces on semi-infinite substrate without any consideration of these effects was used, theoretical spectra exhibit higher amplitudes compared to the experimental data.

Polar Kerr effect spectra of the sample B1YIGb along with the theoretical simulation are displayed in Fig. 8.6. In this case, the film thickness was determined to be $t = 235$ nm. Again, the spectral behavior of the experiment is in a good agreement with the calculation, especially for lower energies. However, contrary to the sample B1YIGa, experimental amplitudes are higher compared to the theoretical calculation.

A great interest was dedicated to the quantitative analysis of the influence of bismuth doping on the magnetic and magneto-optical properties [30, 133, 156, 157, 158, 159]. These results were mainly presented on stoichiometric films prepared by LPE and describe the increase of the internal magnetization in Bi:YIG as a consequence of the enlargement of lattice parameter by Bismuth doping. Very recently an important role of non-stoichiometry of Bi:YIG and Bi:IG films prepared by PLD technique was reported [137, 160].

We believe that non-stoichiometry of investigated films would decrease the oxygen content in the layer, which leads to the rise of the charge transfer between Fe atoms due to their covalent bonding caused by the absence of oxygen atoms. This would cause a spread of the main spectral shapes along with the increase of the absorption. We did not observe such effects in

8.3. MAGNETO-OPTICAL SPECTROSCOPY

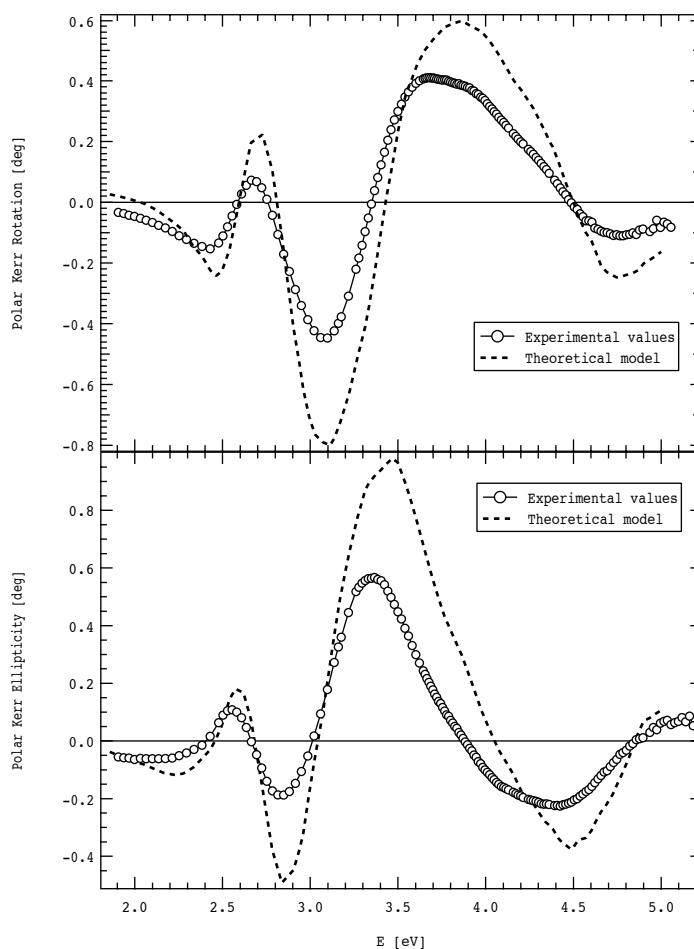


Figure 8.5: Experimental polar Kerr spectra for the sample B1YIGa (dots) compared with the theoretical model (dashed line). In the calculation, the thickness of the Bi:YIG film was considered $t = 73$ nm.

polar Kerr spectra of the sample B1YIGb. Especially the absorption can not be high, because of the interference observed in the low energy region. Thus the difference between theoretical and experimental values shown in Fig 8.6 seems to be due to a higher bismuth content in the film than it was expected from the deposition. This can be a consequence of higher substrate temperature during the deposition compared to the sample B1YIGa. To present a deeper analysis of this problem would require a consideration of a large number of parameters (such as iron oxidation state, distances between oxygen and iron atoms, angles of the bonding, spin-orbit coupling, etc.).

Owing to the absence of reported magneto-optical constants for bismuth concentration $x = 2$, we were not able to calculate the theoretical spectra of the Kerr effect for the sample B2YIG and derive its thickness. However, from Fig. 8.2 one can see a slightly higher amplitude of

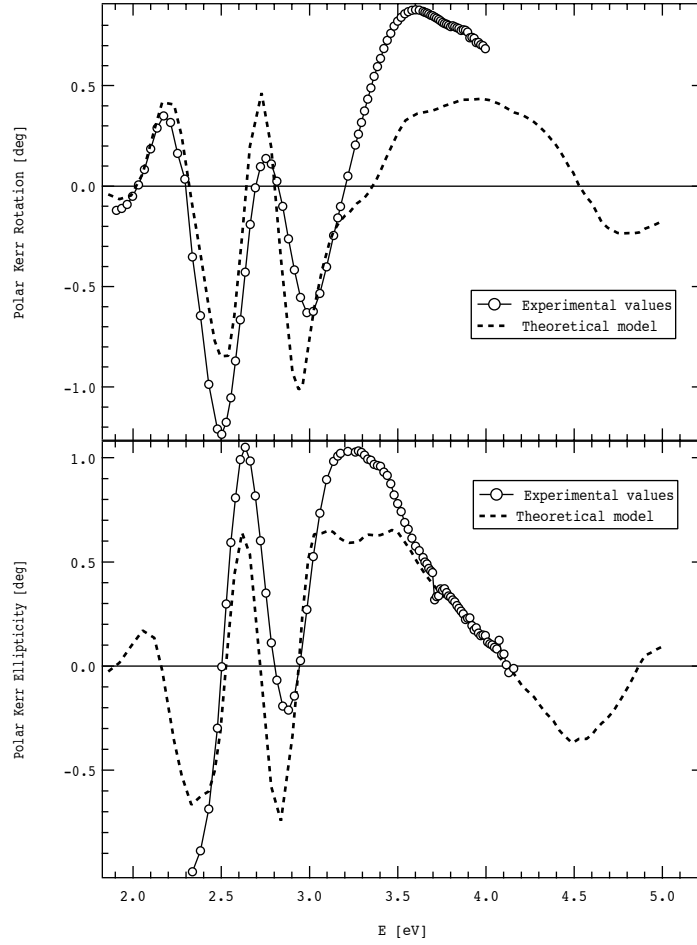


Figure 8.6: Experimental polar Kerr spectra for the sample B1YIGb (dots) compared with the theoretical model (dashed line). In the calculation, the thickness of the Bi:YIG film was considered $t = 235$ nm.

polar Kerr rotation as well as the red shift of the main spectral peak near 3.6 eV compared to the sample B1YIGa. These findings are consistent with results reported by Wittekoek [30].

8.3.2 Longitudinal geometry

The longitudinal rotation was obtained at incident light polarization perpendicular (s) and parallel (p) to the plane of incidence as a complex ratio of reflection coefficients with regard to the definitions derived in Chapter 2. The optical sequence was the same as in the polar geometry with the angle of incidence, φ , adjusted to 56 degree. The sample was kept at ambient temperature of approximately 295 K. The magnetic field of 0.1 T was high enough to ensure the magnetic saturation of the sample. Because the amplitude of the longitudinal Kerr rotation is usually very small, the effect of the stray magnetic field on the optical elements was considered

8.3. MAGNETO-OPTICAL SPECTROSCOPY

in the data processing.

The spectra of longitudinal Kerr rotation for both incident polarizations are shown in Fig. 8.7. Magneto-optical interference at lower energy side is clearly visible for s incident polarization similarly to the polar Kerr spectra. Samples B1YIGb and B2YIG are similar in shape with sharp positive spectral peak at 3.4 eV and negative peak at 4.2 eV. The longitudinal Kerr rotation of the sample B1YIGa has a different spectral behavior with a broad maximum at 4 eV. The highest amplitude of the longitudinal Kerr rotation measured at s incident polarization exhibits the sample B1YIGb, while the smallest rotation is measured for the sample B1YIGa. This is consistent with the results obtained in polar geometry. As was expected, longitudinal Kerr effect amplitudes are almost one order smaller compared to the polar geometry.

Longitudinal Kerr rotation spectra measured at p incident polarization for B1YIGa and B1YIGb samples do not show any significant difference in their spectral shape. Both samples exhibit two spectral peaks of opposite signs. First, positive one, centered near 2.6 eV and second, negative, centered near 4.2 eV. Sample B1YIGb exhibits, as was expected, higher amplitudes of longitudinal Kerr rotation.

Similarly to the polar geometry, theoretical spectra of longitudinal Kerr rotation of the sample B1YIGa were calculated taking into account the same model of the single layer on a semi-infinite substrate. The results of this calculation compared to the experimental data are shown in Fig. 8.8. From this figure, one can see a satisfactory agreement between theoretical and experimental spectral behavior of longitudinal Kerr rotation. The difference in the case of the s polarized incident light can be explained similarly as in the polar geometry. Owing to the small thickness of the sample, effects of the non-ideal interface between the film and the substrate as well as the non-ideal surface have an important influence on the magnetic properties of the sample. These effects result in a decrease of the internal magnetization and consequently suppression of the longitudinal Kerr effect. Therefore the theoretical model, which is not considering this fact, gives a higher amplitudes than the experiment. Contrary, the experimental data of longitudinal Kerr rotation measured for p polarized incident light exhibit higher amplitudes beyond 3 eV compared to the theoretical prediction. This situation reflects the fact that the magneto-optical constants were obtained on polycrystalline samples with higher light scattering in the UV range. The scattering of the incident light leads to its depolarization and consequently to the lowering of detected intensity. Last but not least, we have to consider the optical anisotropy induced by the large lattice mismatch between GGG substrate and the Bi:YIG film. Such anisotropy may influence the magneto-optical spectra as well. The overall shape of the spectra remains well reproduced.

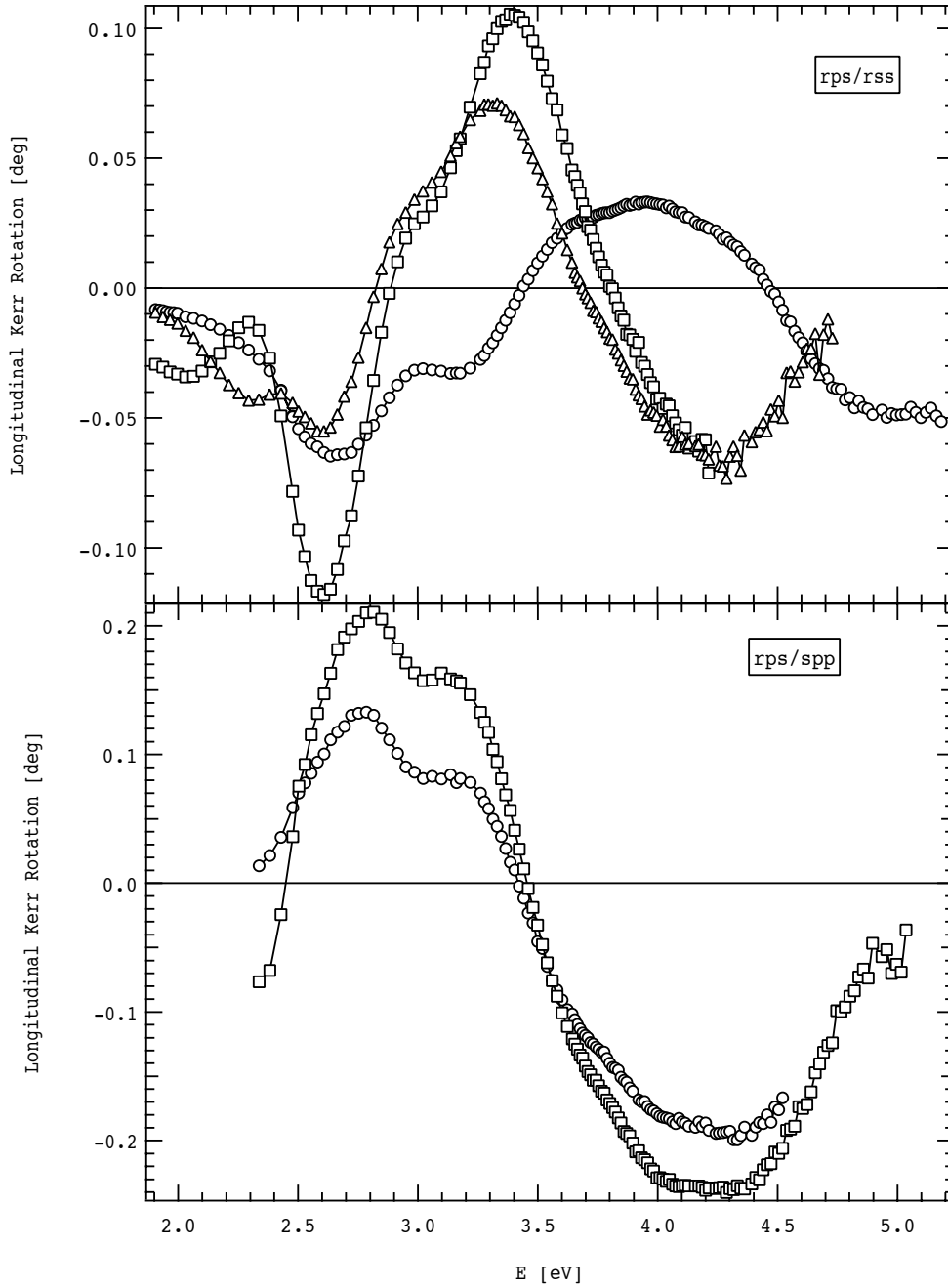


Figure 8.7: Room temperature longitudinal Kerr rotations of Bi:YIG films grown on (111) GGG substrates measured as both $Re\{r_{ps}/r_{pp}\}$ and $Re\{r_{ps}/r_{ss}\}$ ratios corresponding to the incident polarizations parallel and perpendicular to the plane of incidence. The angle of light incidence was 56° .

8.4. CONCLUSION

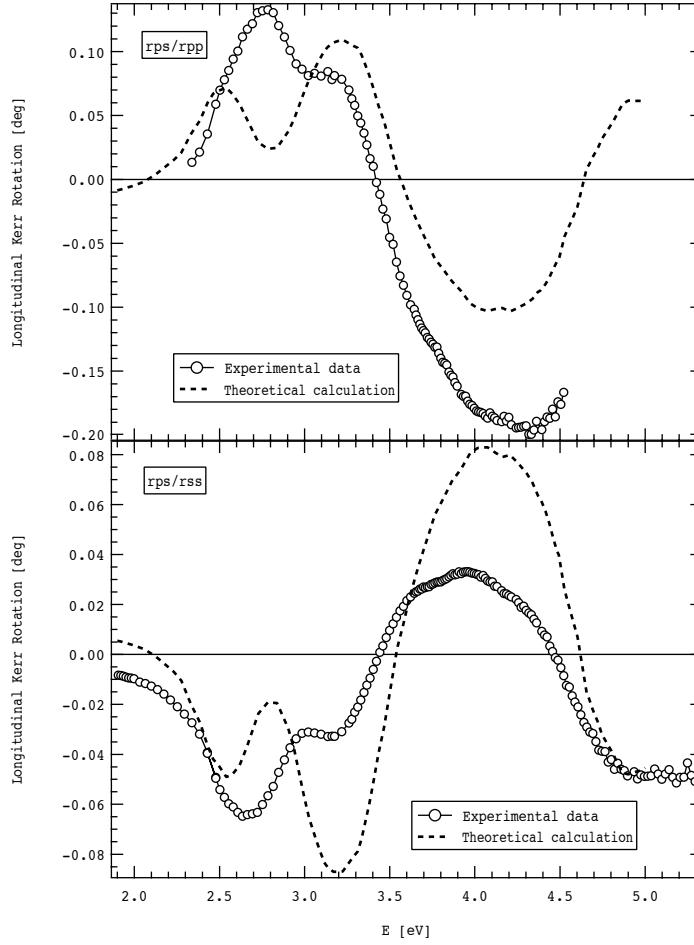


Figure 8.8: Experimental and computed longitudinal Kerr rotation, $Re\{r_{ps}/r_{pp}\}$ and $Re\{r_{ps}/r_{ss}\}$, at an angle of incidence of 56° for the sample BiYIGa. The sample is characterized by its ε_{xx} and ε_{xy} .

8.4 Conclusion

To conclude this section, Kerr effect spectra of Bi:YIG films with different Bi substitution prepared by PLD technique have been measured in polar and longitudinal geometries. Low noise in the magneto-optical signal indicated a good surface quality of investigated samples. The interference was observed for all samples in both, polar and longitudinal geometries for energies below 3 eV. Because the film thicknesses have not been derived from structural characterizations, a theoretical model of a single layer on a semi-infinite substrate was used to fit the experimental data and determine the layer thickness. The theoretical calculation revealed one of the thicknesses below 100 nm, while both theoretical and experimental data confirmed the garnet structure of the sample even for such thin layer. Small difference in amplitudes was

CHAPTER 8. EXPERIMENTAL RESULTS ON Bi:YIG THIN FILMS

explained as a consequence of interface effect with regard to the small thickness. Therefore the magneto-optical spectroscopy act well as a useful and sensitive technique to investigate thin layers of Bi:YIG suitable for the magneto-phonic crystal application.

9 Summary

The aim of this work was to investigate and understand the optical properties of thin films of selected magnetic oxides. For this purpose, methods of spectroscopical ellipsometry along with magneto-optical spectroscopy were used. The original principal results are:

- Optical and magneto-optical spectra of $\text{La}_{2/3}\text{Sr}_{1/3}\text{MnO}_3$ thin films deposited on (100) and (110) SrTiO_3 substrates were investigated by means of spectroscopic ellipsometry and magneto-optical spectroscopy. Electronic transitions inside the material, optical and magneto-optical properties as well as their mutual dependences among with the crystalline structure were described by analysis of the experimental data. Comparing the results for samples deposited on both types of substrates, no significant influence of the crystallographic orientation of the substrate on optically and magneto-optically active transitions was found. For thinner samples, the deviation from the linear thickness dependence of polar and longitudinal Kerr effect predicted by theory was observed. Moreover, the thickness dependence of magneto-optical transitions energies was found and explained by the partial relaxation of the tensile strain induced by the lattice mismatched substrate. Altogether five transitions were revealed in optical and magneto-optical spectra. They belong to both charge transfer and crystal field splitting type transitions. The experiments showed high quality of investigated samples and a fully developed material structure even at very low thicknesses below 50 nm. This is an interesting result from the application point of view.
- Results of ellipsometric and magneto-optical measurements on CuFe_2O_4 thin films with cubic and tetragonal crystalline structures were presented. The combination of spectroscopic ellipsometry and magneto-optical spectroscopy showed itself as an effective method to investigate the electronic structure of these inverse spinels. Utilization of both methods detected six electron transitions in a broad spectral region near energies 2.4, 2.7, 3.3, 3.9, 4.7, and 13.2 eV. First four transitions were, consistently with literature, assigned to ISCT transitions between Fe^{3+} ions placed at octahedral and tetrahedral sites. The fifth transition was assigned to an IVCT transition between Cu^{2+} and Fe^{3+} ions. Finally the last transition was discussed as an electron transfer between O $2p$ valence band and Fe $4s$ conduction band. This assignment was confirmed by the derivation of the crystal

field splitting energy for both octahedral and tetrahedral iron ions respectively. Obtained energies were in a good agreement with theoretically predicted values as well as with experimental results obtained on similar compounds.

- Kerr effect spectra of Bi:YIG films with different Bi substitution prepared by PLD technique have been measured in polar and longitudinal geometries. Low noise in the magneto-optical signal indicated a high quality surface of investigated samples. Magneto-optical interference was observed for all samples in both, polar and longitudinal geometries for energies below 3 eV. Because the film thicknesses had not been derived from structural characterizations, a theoretical model of a single layer on a semi-infinite substrate was used to fit the experimental data and determine the layer thickness. The theoretical calculations revealed one of the thicknesses below 100 nm, while both theoretical and experimental data confirmed the garnet structure of the sample even for such thin layer. Small differences in amplitudes were explained as a consequence of interface effect with regard to the small thickness.

Bibliography

- [1] B. Koopmans, M. van Kampen, J. T. Kohlhepp, and W. J. M. de Jonge, *Phys. Rev. Lett.* **85**, 844 (2000).
- [2] T. Aign et al., *Phys. Rev. Lett.* **81**, 5656 (1998).
- [3] J. J. F. Dillon, *Journal of Applied Physics* **39**, 922 (1968).
- [4] J. Dillon, *Journal of Magnetism and Magnetic Materials* **31-34** (1983).
- [5] J. Suits, *IEEE Trans. Magn.* **8**, 95 (72).
- [6] W. Wetling, *Journal of Magnetism and Magnetic Materials* **3**, 147 (1976).
- [7] J. G. Bednorz and K. A. Muller, *Z. Physik B* **64**, 189 (1986).
- [8] K. ichi Chahara, T. Ohno, M. Kasai, and Y. Kozono, *Applied Physics Letters* **63**, 1990 (1993).
- [9] R. von Helmolt, J. Wecker, B. Holzapfel, L. Schultz, and K. Samwer, *Phys. Rev. Lett.* **71**, 2331 (1993).
- [10] S. Jin et al., *Science* **264**, 413 (1994).
- [11] M. Hase, I. Terasaki, and K. Uchinokura, *Phys. Rev. Lett.* **70**, 3651 (1993).
- [12] S. Taniguchi et al., *J. Phys. Soc. Jpn.* **64**, 2758 (1995).
- [13] R. A. M. Azzam and N. M. Bashara, *Ellipsometry and polarized light*, Nort-Holland, 1977.
- [14] A. Yariv and P. Yeh, *Optical waves in crystals*, John Wiley and Sons, New York, 1984.
- [15] S. Visnovsky, *Optics in Magnetic Multilayers and Nanostructures*, Taylor and Francis, 2006.

- [16] H. S. Bennett and E. A. Stern, Phys. Rev. **137**, A448 (1965).
- [17] J. F. Dillon, J. P. Remeika, and C. R. Staton, Journal of Applied Physics **41**, 4613 (1970).
- [18] A. Yariv, *Quantum electronics*, Wiley, New York, 1975.
- [19] R. M. White, *Quantum Theory of Magnetism*, Springer Verlag, Berlin, 1983.
- [20] F. Bassani and G. P. Parravicini, *Electronic States and Optical Transitions in Solids*, Pergamon Press, Oxford, 1975.
- [21] R. Kubo, J. Phys. Soc. Jpn. **12**, 570 (1957).
- [22] B. D. Bartolo, *Optical Interactions in Solids*, John Wiley, New York, 1968.
- [23] S. Visnovsky, Czech. J. Phys. B **36**, 625 (1986).
- [24] M. Nyvlt, *Optical interactions in ultrathin magnetic film structures*, PhD thesis, Charles University in Prague, Czech Republic, 1996.
- [25] F. Wooten, *Optical Properties of Solids*, Academic Press, New York - London, 1972.
- [26] C. Cohen-Tannoudji, B. Diu, and F. Laloe, *Quantum Mechanics*, Wiley-Interscience, 2006.
- [27] Y. R. Shen, Phys. Rev. **133**, A511 (1964).
- [28] F. J. Kahn, P. S. Pershan, and J. P. Remeika, Phys. Rev. **186**, 891 (1969).
- [29] W. A. Crossley, R. W. Cooper, J. L. Page, and R. P. van Staple, Phys. Rev. **181**, 896 (1969).
- [30] S. Wittekoek, T. J. A. Popma, J. M. Robertson, and P. F. Bongers, Phys. Rev. B **12**, 2777 (1975).
- [31] H. le Gall and J. P. Jamet, physica status solidi (b) **46**, 467 (1971).
- [32] A. M. Clogston, Journal of Applied Physics **31**, S198 (1960).
- [33] N. Bloembergen, *Nonlinear Optics*, W. A. Benjamin, Inc., 1965.
- [34] W. F. J. Fontijn, P. J. van der Zaag, M. A. C. Devillers, V. A. M. Brabers, and R. Metselaar, Phys. Rev. B **56**, 5432 (1997).
- [35] P. S. Pershan, Journal of Applied Physics **38**, 1482 (1967).

BIBLIOGRAPHY

- [36] M. Mansuripur, *Journal of Applied Physics* **67**, 6466 (1990).
- [37] R. K. Wangsness, *Electromagnetic fields*, John Wiley and Sons, Inc., New York, 1979.
- [38] R. P. Hunt, *Journal of Applied Physics* **38**, 1652 (1967).
- [39] A. Hubert and G. Traeger, *Journal of Magnetism and Magnetic Materials* **124**, 185 (1993).
- [40] J. Zak, E. R. Moog, C. Liu, and S. D. Bader, *Journal of Magnetism and Magnetic Materials* **89**, 107 (1990).
- [41] J. Zak, E. R. Moog, C. Liu, and S. D. Bader, *Phys. Rev. B* **43**, 6423 (1991).
- [42] W. A. McGahan and J. A. Woolam, *Appl. Phys. Commun.* **9**, 1 (1989).
- [43] L. Wenzel, V. Kambersky, and A. Hubert, *physica status solidi (a)* **151**, 449 (1995).
- [44] P. Yeh, *Surface Science* **96**, 41 (1980).
- [45] S. Visnovsky, *Czech. J. Phys. B* **41**, 663 (1991).
- [46] K. Postava et al., *Journal of Magnetism and Magnetic Materials* **272-276**, 2319 (2004).
- [47] R. Lopusnik et al., *Journal of Applied Physics* **101**, 09C516 (2007).
- [48] R. Antos, *Diffraction on laterally structured anisotropic periodic systems*, PhD thesis, Charles University in Prague, 2006.
- [49] J. Pommier et al., *Phys. Rev. Lett.* **65**, 2054 (1990).
- [50] J. McCord, H. Brendel, A. Hubert, and S. S. P. Parkin, *Journal of Magnetism and Magnetic Materials* **148**, 244 (1995).
- [51] K. Postava, *Light propagation in magneto-optical multilayers. Magnetization behavior*, PhD thesis, Palacky University Olomouc, Czech Republic, 1997.
- [52] R. Kusters, J. Singleton, D. Keen, R. McGreevy, and W. Hayes, *Physica B* **155**, 362 (1989).
- [53] R. von Helmolt, J. Wecker, B. Holzapfel, L. Schultz, and K. Samwer, *Phys. Rev. Lett.* **71**, 2331 (1993).
- [54] C. Zener, *Phys. Rev.* **82**, 403 (1951).

- [55] J. B. Goodenough, *Phys. Rev.* **100**, 564 (1955).
- [56] P. G. de Gennes, *Phys. Rev.* **118**, 141 (1960).
- [57] S. Y. Yang et al., *Japanese Journal of Applied Physics* **45**, 5754 (2006).
- [58] P. Dey, T. K. Nath, and A. Taraphder, *Applied Physics Letters* **91**, 012511 (2007).
- [59] U. Staub et al., *Europhysics Letters* **76**, 926 (2006).
- [60] K. Steenbeck and R. Hiergeist, *Applied Physics Letters* **75**, 1778 (1999).
- [61] T. K. Nath et al., *Applied Physics Letters* **74**, 1615 (1999).
- [62] L. M. Berndt, V. Balbarin, and Y. Suzuki, *Applied Physics Letters* **77**, 2903 (2000).
- [63] S. G. Kaplan et al., *Phys. Rev. Lett.* **77**, 2081 (1996).
- [64] M. Quijada et al., *Phys. Rev. B* **58**, 16093 (1998).
- [65] J. H. Jung et al., *Phys. Rev. B* **55**, 15489 (1997).
- [66] H. L. Liu et al., *Journal of Applied Physics* **97**, 113528 (2005).
- [67] T. Popma and M. Kamminga, *Solid State Communications* **17**, 1073 (1975).
- [68] S. Yamaguchi, Y. Okimoto, K. Ishibashi, and Y. Tokura, *Phys. Rev. B* **58**, 6862 (1998).
- [69] H. L. Liu et al., *Journal of Applied Physics* **99**, 043908 (2006).
- [70] H. Liu et al., *Journal of Magnetism and Magnetic Materials* **304**, e303 (2006).
- [71] P. Fumagalli, C. Spaeth, and G. Guntherodt, *IEEE Trans. Magn.* **31**, 3277 (1995).
- [72] M. Koubaa et al., *Journal of Magnetism and Magnetic Materials* **272-276**, 1812 (2004).
- [73] J. Mistrik et al., *Journal of Applied Physics* **99**, 08Q317 (2006).
- [74] J. Cho, M. Gomi, and M. Abe, *Japanese Journal of Applied Physics* **29**, 1686 (1990).
- [75] E. Balykina, E. Ganshina, G. Krinchik, A. Trifonov, and I. Troyanchuk, *Journal of Magnetism and Magnetic Materials* **92**, 259 (117).
- [76] E. A. Gan'shina et al., *Journal of Physics: Condensed Matter* **12**, 2857 (2000).
- [77] M. S. Laad, L. Craco, and E. Muller-Hartmann, *New Journal of Physics* **6**, 157 (2004).

BIBLIOGRAPHY

- [78] I. Bergenti et al., *Journal of Magnetism and Magnetic Materials* **310**, e780 (2007).
- [79] A.-M. Haghiri-Gosnet and J.-P. Renard, *Journal of Physics D: Applied Physics* **36**, R127 (2003).
- [80] T. Kimura and Y. Tokura, *Annu. Rev. Mater. Sci.* **30**, 445 (2000).
- [81] A. M. Haghiri-Gosnet, M. Hervieu, C. Simon, B. Mercey, and B. Raveau, *Journal of Applied Physics* **88**, 3545 (2000).
- [82] H. S. Kim and H. S. Kwok, *Applied Physics Letters* **61**, 2234 (1992).
- [83] C. J. Lu, Z. L. Wang, C. Kwon, and Q. X. Jia, *Journal of Applied Physics* **88**, 4032 (2000).
- [84] T. Kanki, H. Tanaka, and T. Kawai, *Solid State Communications* **114**, 267 (2000).
- [85] K. Takenaka, Y. Sawaki, R. Shiozaki, and S. Sugai, *Phys. Rev. B* **62**, 13864 (2000).
- [86] T. Arima, Y. Tokura, and J. B. Torrance, *Phys. Rev. B* **48**, 17006 (1993).
- [87] J. H. Jung, K. H. Kim, T. W. Noh, E. J. Choi, and J. Yu, *Phys. Rev. B* **57**, R11043 (1998).
- [88] P. Kielar, *J. Opt. Soc. Am. B* **11**, 854 (1994).
- [89] J. V. Vleck, *The Theory of Electric and Magnetic Susceptibilities*, Oxford University Press, New York, 1975.
- [90] I. C. Infante et al., *Physical Review B* **76**, 224415 (2007).
- [91] Y. Tokura and N. Nagaosa, *Science* **288**, 462 (2000).
- [92] J. Sakai, N. Ito, and S. Imai, *Journal of Applied Physics* **99**, 08Q318 (2006).
- [93] Y. Du, B. Wang, T. Li, D. Yu, and H. Yan, *Journal of Magnetism and Magnetic Materials* **297**, 88 (2006).
- [94] S. Jacob, T. Roch, F. S. Razavi, G. M. Gross, and H.-U. Habermeier, *Journal of Applied Physics* **91**, 2232 (2002).
- [95] A. J. Millis, T. Darling, and A. Migliori, *Journal of Applied Physics* **83**, 1588 (1998).
- [96] J. Dho, Y. N. Kim, Y. S. Hwang, J. C. Kim, and N. H. Hur, *Applied Physics Letters* **82**, 1434 (2003).

- [97] H. Chou et al., *Applied Physics Letters* **89**, 082511 (2006).
- [98] T. Kanki, H. Tanaka, and T. Kawai, *Phys. Rev. B* **64**, 224418 (2001).
- [99] C. Kwon et al., *Journal of Magnetism and Magnetic Materials* **172**, 229 (1997).
- [100] Y. Du, X. Zhang, D. Yu, and H. Yan, *Journal of Rare Earths* **24**, 560 (2006).
- [101] T. Becker et al., *Phys. Rev. Lett.* **89**, 237203 (2002).
- [102] A. Urushibara et al., *Phys. Rev. B* **51**, 14103 (1995).
- [103] R. B. Praus, G. M. Gross, F. S. Razavi, and H. U. Habermeier, *Journal of Magnetism and Magnetic Materials* **211**, 41 (2000).
- [104] J. Dho, Y. N. Kim, Y. S. Hwang, J. C. Kim, and N. H. Hur, *Applied Physics Letters* **82**, 1434 (2003).
- [105] A. M. De León-Guevara et al., *Phys. Rev. B* **56**, 6031 (1997).
- [106] T. Geng and N. Zhang, *Physics Letters A* **351**, 314 (2006).
- [107] V. A. M. Brabers, *Handbook of Magnetic Materials*, volume 8, North-Holland, Amsterdam, 1995.
- [108] S. Krupicka, *Fyzika feritů a příbuzných magnetických kysličníků*, Academia, 1969.
- [109] C. J. Ballhausen, *Introduction to Ligand Field Theory*, McGraw-Hill, 1962.
- [110] H. A. Jahn and E. Teller, *Proc. Rec. Soc. London* **161**, 220 (1037).
- [111] M. Desai et al., *Journal of Magnetism and Magnetic Materials* **246**, 266 (2002).
- [112] M. Desai et al., *Journal of Applied Physics* **91**, 2220 (2002).
- [113] Z. Sima, H. Legall, and P. Siroky, *physica status solidi (b)* **100**, 665 (1980).
- [114] X.-X. Zhang, J. Schoenes, W. Reim, and P. Wachter, *Journal of Physics C: Solid State Physics* **16**, 6055 (1983).
- [115] S. Visnovsky et al., *Magnetics*, *IEEE Transactions on* **17**, 3205 (1981).
- [116] H. Feil, *Solid State Communications* **69**, 245 (1989).
- [117] A. Paoletti, *Physics of magnetic garnets*, in *Proceedings of the international school physics Enrico Fermi*, 1978.

BIBLIOGRAPHY

- [118] G. B. Scott, D. E. Lacklison, H. I. Ralph, and J. L. Page, *Phys. Rev. B* **12**, 2562 (1975).
- [119] W. F. J. Fontijn, P. J. van der Zaag, L. F. Feiner, R. Metselaar, and M. A. C. Devillers, **85**, 5100 (1999).
- [120] R. Antos et al., *Journal of Applied Physics* **97**, 053107 (2005).
- [121] J. W. D. Martens, W. L. Peeters, H. M. van Noort, and M. Erman, *Journal of Physics and Chemistry of Solids* **46**, 411 (1985).
- [122] D. L. Camphausen, J. M. D. Coey, and B. K. Chakraverty, *Phys. Rev. Lett.* **29**, 657 (1972).
- [123] S. F. Alvarado, M. Erbudak, and P. Munz, *Phys. Rev. B* **14**, 2740 (1976).
- [124] M. Kucera et al., *Journal of Magnetism and Magnetic Materials* **316**, e688 (2007).
- [125] K. J. Kim, J. H. Lee, and S. H. Lee, *Journal of Magnetism and Magnetic Materials* **279**, 173 (2004).
- [126] S. Visnovsky, N. P. Thuy, J. Stepanek, V. Prosser, and R. Krishnan, *Journal of Applied Physics* **50**, 7466 (1979).
- [127] S. Visnovsky et al., *Journal of Magnetism and Magnetic Materials* **15-18**, 831 (1980).
- [128] W. F. J. Fontijn, P. J. van der Zaag, and R. Metselaar, *The 7th joint MMM-intermag conference on magnetism and magnetic materials* **83**, 6765 (1998).
- [129] K. J. Kim, H. S. Lee, M. H. Lee, and S. H. Lee, *Journal of Applied Physics* **91**, 9974 (2002).
- [130] D. S. Wiersma, P. Bartolini, A. Lagendijk, and R. Righini, *Nature* **390**, 671 (1997).
- [131] G. Winkler, *Magnetic garnets*, Freidr. Vieweg and Sohn, 1981.
- [132] C. F. Buhner, *Journal of Applied Physics* **40**, 4500 (1969).
- [133] F. Hansteen et al., *Thin Solid Films* **455-456**, 429 (2004), *The 3rd International Conference on Spectroscopic Ellipsometry*.
- [134] M. Inoue, K. Arai, T. Fujii, and M. Abe, *Journal of Applied Physics* **85**, 5768 (1999).
- [135] H. Kato et al., *Journal of Applied Physics* **93**, 3906 (2003).
- [136] S. Geller and M. A. Gilleo, *Journal of Physics and Chemistry of Solids* **3** (1957).

- [137] B. Vertruyen et al., *Physical Review B* **78**, 094429 (2008).
- [138] K. von Enke, *Magnetic and other properties of oxides and related compounds, Part a: Garnets and perovskites.*, Landolt-Bornstein, Condensed matter, Springer-Verlag, 1978.
- [139] M. A. Gilleo and S. Geller, *Phys. Rev.* **110**, 73 (1958).
- [140] P. Hansen, K. Witter, and W. Tolksdorf, *Phys. Rev. B* **27**, 6608 (1983).
- [141] L. E. Helseth, R. W. Hansen, E. I. Il'yashenko, M. Baziljevich, and T. H. Johansen, *Phys. Rev. B* **64**, 174406 (2001).
- [142] L. E. Helseth et al., *Phys. Rev. B* **66**, 064405 (2002).
- [143] R. C. Linares, *Journal of Crystal Growth* **3-4**, 443 (1968).
- [144] R. Lux et al., *Journal of Applied Physics* **100**, 113511 (2006).
- [145] S. Kahl et al., *Journal of Applied Physics* **91**, 9556 (2002).
- [146] N. Adachi, V. P. Denysenkov, S. I. Khartsev, A. M. Grishin, and T. Okuda, *Journal of Applied Physics* **88**, 2734 (2000).
- [147] M. Laulajainen et al., *Journal of Magnetism and Magnetic Materials* **279**, 218 (2004).
- [148] T. Okuda et al., *Journal of Applied Physics* **67**, 4944 (1990).
- [149] M. Gomi, T. Tanida, and M. Abe, *Journal of Applied Physics* **57**, 3888 (1985).
- [150] M. Okada, S. Katayama, and K. Tominaga, *Journal of Applied Physics* **69**, 3566 (1991).
- [151] K. Matsumoto, S. Sasaki, Y. Asahara, K. Yamaguchi, and T. Fujii, *Journal of Magnetism and Magnetic Materials* **104-107**, 451 (1992).
- [152] S. Mino, M. Matsuoka, A. Shibukawa, and K. Ono, *Japanese Journal of Applied Physics* **29**, L1823 (1990).
- [153] P. Papakonstantinou, B. Teggart, and R. Atkinson, *Journal of Magnetism and Magnetic Materials* **163**, 378 (1996).
- [154] D. L. Wood and K. Nassau, *Applied Optics* **29**, 3704 (1990).
- [155] S. Kahl and A. M. Grishin, *Journal of Applied Physics* **93**, 6945 (2003).
- [156] G. F. Dionne and G. A. Allen, *Journal of Applied Physics* **73**, 6127 (1993).

- [157] G. F. Dionne and G. A. Allen, *Journal of Applied Physics* **75**, 6372 (1994).
- [158] S. Kahl, V. Popov, and A. M. Grishin, *Journal of Applied Physics* **94**, 5688 (2003).
- [159] V. Doormann, J.-P. Krumme, and H. Lenz, *Journal of Applied Physics* **68**, 3544 (1990).
- [160] Y. Dumont et al., *Physical Review B* **76**, 104413 (2007).

List of the Author's Publications

Original refereed journal papers

1. Moke spectroscopy of Sputter Deposited Cu-ferrite films
Journal of Magnetism and Magnetic Materials, Vol. 272-276, p. E885 (2004)
M. Veis, V. Kolinský, Š. Višňovský, P.D.Prasanna D. Kulkarni, Mrugesh Desai, N. Venkataramani, Shiva Prasad, R. Krishnan
2. Magneto-optical spectroscopy of strained $\text{La}_{2/3}\text{Sr}_{1/3}\text{MnO}_3$ thin films grown by "laser MBE"
Journal of Magnetism and Magnetic Materials, Vol. 272-276, p. 272 (2004)
M. Koubaa, A. M. Haghiri-Gosnet, J. P. Renard, **M. Veis**, V. Kolinský, Š. Višňovský, Ph. Lecoeur, W. Prellier, B. Mercey
3. Interface Effects on Magneto-Optic Kerr and Reflectivity Spectra in Ultrathin Fe/Au and Fe/Ag Systems
Trans. Magn. Soc. Japan, Vol 4, p. 293 (2004)
J. Ğrondilová, M. Rickart, **M. Veis**, E. Lišková, K. Postava, Š. Višňovský, S. O. Demokritov, B. Hillebrands, J. Mistrík, T. Yamaguchi
4. Moke Spectroscopy of Sputter Deposited Cu-Ferrite films
Journal of Magnetism and Magnetic Materials, Vol. 290-291, p. 195 (2005)
Š. Višňovský, **M. Veis**, E. Lišková, V. Kolinský, Prasanna D. Kulkarni, N. Venkataramani, S. Prasad, R. Krishnan
5. Magneto-optical and optical spectroscopic ellipsometries of $\text{La}_{2/3}\text{Sr}_{1/3}\text{MnO}_3$ thin films
Journal of Applied Physics, Vol. 99, p. 08Q317 (2006)
J. Mistrík, T. Yamaguchi, **M. Veis**, E. Lišková, Š. Višňovský, M. Koubaa, A. M. Haghiri-Gosnet, Ph. Lecoeur, J. P. Renard, W. Prellier, B. Mercey
6. Optimization of magneto-optical response of FeF₂/Fe/FeF₂ sandwiches for microwave field detection
Journal Applied Physics, Vol 101, p. 09C516 (2007)
R. Lopušník, J. Correu, I. Harward, S. Widuch, P. Maslankiewicz, S. Demirtas, Z. Celinski, E. Lišková, **M. Veis**, Š. Višňovský

Conference presentations

1. Interface Effects on Magneto-Optic Kerr and Reflectivity Spectra in Ultrathin Fe/Au and Fe/Ag Systems
Magneto-Optical Recording International Symposium, MORIS 2004, Yokohama, Japan
J. Ğrondilová, M. Rickart, **M. Veis**, E. Lišková, K. Postava, Š. Višňovský, S. O. Demokritov, B. Hillebrands, J. Mistrík, T. Yamaguchi
2. Moke Spectroscopy of Sputter Deposited Cu-Ferrite films
Joint European Magnetic Symposia, JEMS 2004, Dresden, Germany
Š. Višňovský, **M. Veis**, E. Lišková, V. Kolinský, Prasanna D. Kulkarni, N. Venkataramani, S. Prasad, R. Krishnan
3. Polar and Longitudinal Magneto-Optic Spectra of Thin Strained $\text{La}_{2/3}\text{Sr}_{1/3}\text{MnO}_3$ Films
Joint European Magnetic Symposia, JEMS 2004, Dresden, Germany
M. Veis, E. Lišková, Š. Višňovský, M. Koubaa, A.M. Haghiri-Gosnet, J.P. Renard, Ph. Lecoeur, W. Prellier, B. Mercey
4. Magneto-optic spectroscopy of PLD Bi substituted yttrium iron garnet films
International workshop on exchange bias 2004, Anglet, France
E. Lišková, **M. Veis**, Š. Višňovský, N. Kumar, D. S. Mishra, N. Venkataramani, S. Prasad, R. Krishnan
5. Temperature dependence of the conductivity in strained $\text{La}_{2/3}\text{Sr}_{1/3}\text{MnO}_3$ thin film
Magnetism and Magnetic Materials conference 2005, Jacksonville, USA
A. Haghiri-Gosnet, M. Koubaa, A. Santander, **M. Veis**, B. Mercey, P. Lecoeur, J. Renard, N. Bontemps, Š. Višňovský
6. Magneto-optical and Optical Spectroscopic Ellipsometry of $\text{La}_{2/3}\text{Sr}_{1/3}\text{MnO}_3$ Thin Films
50th Magnetism and Magnetic Materials conference 2005, San Jose, California USA
J. Mistrík, T. Yamaguchi, **M. Veis**, E. Lišková, Š. Višňovský, M. Koubaa, A. M. Haghiri-Gosnet, Ph. Lecoeur, J. P. Renard, W. Prellier, B. Mercey
7. Magneto-optical spectroscopy of $\text{La}_{2/3}\text{Sr}_{1/3}\text{MnO}_3$ films grown by pulsed laser deposition onto (100) and (110) SrTiO_3 substrates
MRS spring meeting 2007, San Francisco, USA
M. Veis, J. Mistrík, T. Yamaguchi, E. Liškova, Š. Višňovský, A.M. Haghiri-Goset, Ph. Lecoeur, J.P. Renard, W. Prellier, B. Mercey

Citations

- Magneto-optical and optical spectroscopic ellipsometries of $\text{La}_{2/3}\text{Sr}_{1/3}\text{MnO}_3$ thin films
Journal of Applied Physics, Vol. 99, p. 08Q317 (2006)
J. Mistrík, T. Yamaguchi, **M. Veis**, E. Lišková, Š. Višňovský, M. Koubaa, A. M. Haghiri-Gosnet, Ph. Lecoeur, J. P. Renard, W. Prellier, B. Mercey
 1. Nonlinear optical detection of a ferromagnetic state at the single interface of an antiferromagnetic $\text{LaMnO}_3/\text{SrMnO}_3$ double layer
Physical Review B, Vol 78, p 212409 (2008)
N. Ogawa, T. Satoh, Y. Ogimoto, K. Miyano
 2. dc leakage mechanism in artificial biferroic superlattices
Journal of Applied Physics, Vol. 104, p. 104102 (2008)
A. R. Chaudhuri, S. B. Krupanidhi
- Magneto-optical spectroscopy of strained $\text{La}_{2/3}\text{Sr}_{1/3}\text{MnO}_3$ thin films grown by "laser MBE"
Journal of Magnetism and Magnetic Materials, Vol. 272-276, p. 272 (2004)
M. Koubaa, A. M. Haghiri-Gosnet, J. P. Renard, **M. Veis**, V. Kolinský, Š. Višňovský, Ph. Lecoeur, W. Prellier, B. Mercey
 1. Magnetization reversal in patterned $\text{La}_{0.67}\text{Sr}_{0.33}\text{MnO}_3$ thin films by magneto-optical Kerr imaging
Journal of Applied Physics, Vol. 103, p. 113905 (2008)
M. Saib, M. Belmeguenai, L. Mechin, D. Bloyet, S. Flament
 2. Magneto-optical properties of $\text{La}_{0.7}\text{Sr}_{0.3}\text{MnO}_3$ thin films with perpendicular magnetic anisotropy
Journal of Applied Physics, Vol. 99, p. 043908 (2006)
H. L. Liu, K. S. Lu, M. X. Kuo, L. Uba, S. Uba, L. M. Wang, H. T. Jeng